UNIVERSITY OF OKLAHOMA

GRADUATE COLLEGE

TRANSPORT PHENOMENA IN MICRO SCALE CHANNELS AND PORES BY

NUMERICAL SIMULATIONS

A DISSERTATION

SUBMITTED TO THE GRADUATE FACULTY

in partial fulfillment of the requirements for the

Degree of

DOCTOR OF PHILOSOPHY

By

NGOC HONG PHAM
Norman, Oklahoma
2014

TRANSPORT PHENOMENA IN MICRO SCALE CHANNELS AND PORES BY
NUMERICAL SIMULATIONS

A DISSERTATION APPROVED FOR THE
SCHOOL OF CHEMICAL, BIOLOGICAL AND MATERIALS ENGINEERING

BY

_____
Dr. Dimitrios V. Papavassiliou, Chair

_____
Dr. Vassilios I. Sikavitsas

_____
Dr. Robert L. Shambaugh

_____
Dr. Takumi Hawa

_____
Dr. Ramkumar N. Parthasarathy

This work is dedicated to my parents, my wife, and my little daughter, who are always by my side in every moment of joy and pain.

Acknowledgements

Table of Contents

List of Tables

List of Figures

Abstract

In this thesis, the lattice Boltzmann method (LBM) in conjunction with the Lagrangian particle tracking (LPT) algorithm are employed to numerically investigate: (i) *the hydraulic responses to a linear array of finite-length nanoposts attached at the bottom wall of square microchannels under viscous flow conditions*. Different configurations of the array are considered as these changes can directly contribute to flow pattern deformation. Simulation results indicate that the flow structure strongly depends on nanopost height and space between two adjacent nanoposts in the nanopost line, but not on the Reynolds number in the range examined. If nanoposts, however, are grown far apart from each other, a fully developed velocity profile can be recovered at sufficiently long distance downstream and an empirical correlation for calculating the recovery length is proposed; (ii) *the applicability of a three-point gamma probability density function (PDF) found by Voronov et al. (Voronov R.S., VanGordon S.B., Sikavitsas, V.I., Papavassiliou, D.V., Appl. Phys. Let. 2010, 97:024101) for flow-induced stress distributions inside high porosity and randomly structured scaffolds to that in structured porous scaffolds*. To do that, PDF of flow-induced stresses in different scaffold geometries are calculated via flow dynamics simulations. It is found that the direction of flow relative to the internal architecture of the scaffolds is important for stress distributions. The stress distributions follow a common distribution within statistically acceptable accuracy, when the flow direction does not coincide with the direction of internal structural elements of the scaffold; (iii) *the bulk stress distributions in the pore space of columns packed with spheres*. Three different ideally-packed and one randomly-packed configuration of the columns are considered under

Darcy flow conditions. The stress distributions change when the packing type changes. In the Darcy regime, the normalized stress distribution for a particular packing type is independent of the pressure difference that drives the flow and presents a common pattern. The three parameter (3P) log-normal distribution is found to describe the stress distributions in the randomly packed beds within statistical accuracy. In addition, the 3P log-normal distribution is still valid when highly porous scaffold geometries rather than sphere beds are examined. It is also shown that the 3P log-normal distribution can describe the bulk stress distribution in consolidated reservoir rocks like Berea sandstone; (iv) *the fate and transport of nanoparticles (NPs) as they propagate in porous columns that are packed with spherical particles*. In this approach, physical phenomena that result in particle retention and remobilization are represented by a probability for attachment and detachment, respectively. The method is validated with experiments where polymer-stabilized purified multi-walled carbon nanotubes (PMWCNTs) propagate in a column packed with inert glass beads. Comparison of simulation results to the conventional filtration equation leads to the correlation of the simulation input parameters to macroscopically observed parameters, such as attachment and detachment rate constants. Together with the particle kinetics explored by the LBM/LPT simulations with simplicities, transport and kinetics of PMWCNTs in crushed Berea sandstone packed columns are experimentally investigated. The columns were saturated with brine solution, in which the salt concentration was varied from 0 to 10wt%. Experimental results show that the presence of polymer coating effectively eliminates the effects of salt on particle deposition when the salt concentration is less than or equal to 5wt%. At 10wt% salt, when the intensity of Van der Waals attraction

strengthens, a drop in particle recovery compared to that of 5wt% is observed. A new filtration equation that accounts for the dynamic change of single collector efficiency as the deposition process advances is proposed.

CHAPTER I.   INTRODUCTION

Fluid transport in channels at microscale sizes has attracted considerable attention due to its encounter in microfluidics devices for use in a number of engineering disciplines such as chemical, biological, and biomedical engineering. As the field of miniaturization rapidly expands, this type of flow is easily found in micro heat sinks, micro mixers, micro reactors, micro pumps, etc. On the other hand, fluid flow in micro pores of porous media is also common. Typical examples include flow in filtration columns, membranes, soils, and settling rocks. In this thesis, we direct attention to several cases. Specifically, flow in microchannels with heat sinks and flow in micro pores of porous scaffolds and packed bed columns are examined using computational techniques.

I.1   Flow in microchannels and heat sinks

As is well known, a microchip, while operating, generates a lot of heat, which might lead to chip malfunction if not be effectively dissipated. The breakdown of chips due to thermal heat originates from the breakdown of semiconductor junction at high temperature. It is suggested that the operating temperature of a chip should not exceed 80^0C, as most of the chips remain functional below this temperature. However, the traditionally adopted air-cooling techniques show limited heat transfer ability, raising demand for more efficient alternative cooling solutions. In the early 1980s, ideas of a mountable microchannel heat sink using liquid coolant were introduced by Tuckermann and Pease[1]. By driving water through 100μm microchannels, they demonstrated that the device was able to dissipate a heat flux of 780W/cm^2 with a temperature increase of

1

71K. The reported encouraging results are in line with predictions from conventional heat transfer theory, stating that the heat transfer coefficient for fully developed laminar flow in a channel is inversely proportional to the cross section of the channel, highlighting the advantages of adopting microchannels for heat transfer purposes.

Inspiring by the pioneering work of Tuckermann and Pease, a number of investigators have attempted to study such devices in a further extent such as changing channel size, shape, and liquid coolant. Mudawar and Bowers[2] used circular microchannels of 902μm in diameter and 5.8mm in length, and reached an ability of removing heat fluxes as high as 3000W/cm^2. The employed coolant was single-phase water. Celata et al.[3] assessed heat transfer performance of flowing water in microtubes of different diameters, ranging from 50 to 528μm. An increase of Nusselt numbers with tube diameter was observed due to longer thermal entrance lengths in tubes of bigger diameters. Lee and Garimella[4] investigated the effect of channel aspect ratio on Nusselt numbers in rectangular microchannels and found that a high aspect ratio favors local Nusselt numbers. At a certain aspect ratio, both local and average Nusselt numbers rapidly decay in entrance regions, and attain a plateau when flow is fully developed. Correlations for local and average Nusselt numbers as a function of channel aspect ratio were given that showed reasonable agreement with published data. Interestingly, the hyper-exponential decay tendency of local and average Nusselt numbers along the flow direction found in rectangular microchannels also holds for the cases of non-rectangular channels such as channels of trapezoidal and triangular shape[5, 6]. In association with that, the channel geometry effect was confirmed, as heat transfer intensity in triangular microchannels was found to be worse than that in trapezoidal microchannels[5].

Microchannels of trapezoidal shape show promise for on-chip integration, and thereby, have received closer scrutiny, i.e., how heat dissipation performance of the channels would change if the aspect ratio changed[6]. Beside geometric factors affecting heat dissipation efficiency of the micro heat sink, effects of heating position also need to be addressed. Noticing the fact that heat fluxes on the channel walls are never uniform, Lelea[7] conducted a numerical study on a partially heated microchannel. Her results showed a strong dependence of both hydrodynamic behavior and thermal performance on heating positions.

Along with attention given to microchannel shape and size, considerable work has been done on changing liquid coolant or using nanofluids, i.e., with a nanoparticle suspension added, as an alternative species of coolant. Badran et al.[8] used methanol as liquid coolant and reported an improvement of 6% in heat transfer performance in micro heat pipes. Water was also tested, and shown the improvement of 11%. Lee and Mudawar[9] adopted a pre-cooled procedure of HEF 7100 prior to injection into microchannel heat sinks and reported a great enhancement of cooling performance when the working coolant was pre-cooled to 0^0C or below. At such temperature of the liquid coolant, dissipation of a heat flux of up to $700W/cm^2$ can be handled. Uddin and Feroz[10] filled their miniature heat pipe system with acetone and ethanol to cool a desktop processor. Compared to conventional finned aluminum heat sink with cooling fan, the micro heat sink system with such fluids dissipated heat from the heat source more efficiently. Between the two studied cooling fluids, acetone shows better heat removal performance.

As mentioned, nanofluids were also subject to intensive consideration for use in microchannel heat sinks due to their anomalous thermal behaviors, i.e. abnormal enhancement of thermal conductivity with small concentration. Investigations into thermal characteristics of nanofluids have brought a wide species of NPs to lab tests, such as Cu, CuO, Al, TiO_2, carbon nanotubes (CNTs), grapheme, etc. Prior publications have confirmed the enhancement in thermal conductivity of fluids with suspended NPs compared to that of base fluids[11-14]. There are a number of reasons for the reported enhancement after adding NPs, among which are the following[12]: (i) increased surface area and heat capacity of the fluid, (ii) increased apparent thermal conductivity of the fluid, (iii) intensified the mixing fluctuations and turbulence of the fluid. Details about works done and accomplishments on nanofluids can be found in a number of review works, available elsewhere[15-17].

At the same time, tremendous consideration has been given to explore the hydrodynamic behavior of flows in miniature spaces. As being employed to operate under unusual conditions, flow is expected to depart substantially from traditional fluid mechanics correlations, developed for macro scale. The Darcy friction factor, for example, is not able to be predicted by its well-known relation with Reynolds number, since that examined in microchannels appears to be either higher or lower than theoretical predictions[18]. Discrepancies in flow transition regime and hydrodynamic entrance length are also noticed[19, 20]. However, recent innovative ideas of grafting nanopost arrays, i.e., arrays of CNTs, from microchannel walls to further enhance heat dissipation for liquid cooling lead to the need for understanding hydrodynamic behaviors in such systems.

I.2 Fluid transport in scaffolds

In tissue engineering, scaffolds are widely used as supporting 3D geometries on which stem cells attach and differentiate into tissue appropriate for organ transplantation. The process for tissue growth from stem cells involves seeding stem cells onto the scaffolds, culturing *in vitro* the cell-seeded scaffolds in suitable culture medium, where the cells will proliferate and differentiate into desirous tissue, and transplanting the tissue to patient bodies. Therefore, it is of importance to manufacture the scaffolds, which meet specific requirements of mechanical characteristics and external shape. As noticed in the relevant literature, there are diverse materials being used for scaffold manufacturing, including metals, ceramics, and polymers. Due to their disadvantages in biodegradation and processability, scaffolds made by metals and ceramics have received limited consideration[21]. On the other hand, attention on polymeric scaffolds has been continuously growing. Regardless of the construction material, typically employed scaffolds should have high ratio of surface area to volume, so that uniform loading of stem cells with high cell density on the scaffold structure is possible. For this purpose, manufacturing methods aim at creating highly porous scaffolds with either structured or unstructured pore networks (see Figure I.1). Depending on fabricating methods, the porosity of the scaffolds can be up to 97% with the pore size between a few microns to hundreds of microns[22, 23].
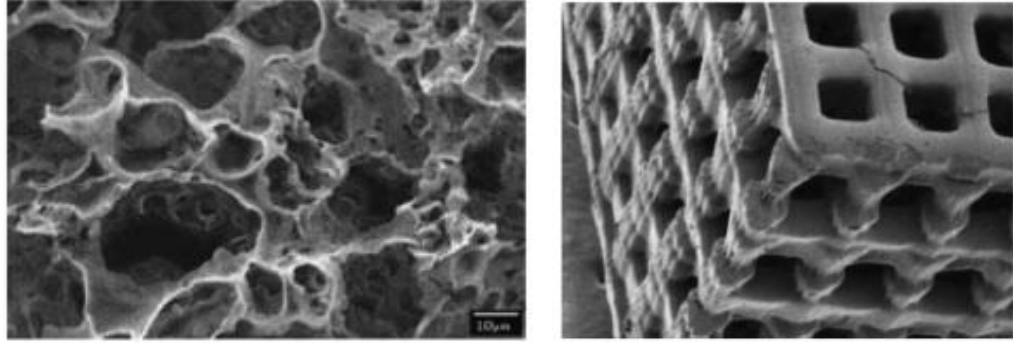
Figure I.1. Left: unstructured pore network of a polylactic acid/polyglycolide (PLGA) scaffold; Right: structured pore network of a poly(propylene fumarate) (PPF) scaffold. Images from Hollister[23].

As already described, after successfully seeding the scaffolds with stem cells, such scaffolds need to be taken to culturing. Culture has been recognized as one of the critical steps for obtaining the desired tissue at the end of the process. Typically, *in vitro* scaffold culture can be performed either statically or dynamically. Static culture includes soaking the cell-seeded scaffolds into an optimized culture medium, keeping the whole system statically for a certain period of time. The term "static" is referred to neither disturbance of the culture medium nor contraction or expansion of the surface on which the cells attach. Due to the static state, this strategy of culture has been reported to result in inhomogeneous cell distribution, in which a majority of cells is found at exterior surface of the scaffold[24, 25]. The inhomogeneity is attributed to the lack of nutrient supply for cells in internal surfaces, and the accumulation of cellular waste products within the scaffold structure without being removed[26]. The dynamic culture approach, on the other hand, is found to be able to overcome such mass transfer limitations associated with the static culture by circulating the culture medium through the scaffold. This dynamic approach involves placing the scaffold into rotatable bioreactors, such as the *spinner flask* and the *rotating wall vessel*. In addition, the

scaffold can also be directly perfused using a *perfusion bioreactor*, in which the flow of the culture medium is circulated by a pump. The main advantages of such devices occur because the flow enhances the nutrient and oxygen transport toward the scaffold via convection, and reduces waste products accumulating during the cell growth. Also, conducting the culture step dynamically is found to stimulate cell growth by exerting shear stress on the cells. It has been reported that an increase of average stresses from 0.2mPa to 1mPa leads to increasing the cell volume fraction from 0.4 to 0.7[27]. However, the applied stresses should not be over critical values, otherwise cell detachment and necrosis would be induced. It is, therefore, important to be able to predict the stress field associated with the chosen operating conditions of flow.

I.3 Nanoparticle transport in micro pores of packed bed columns

In recent years, transport of NPs (particles with at least one critical dimension smaller than 100nm[28]) into the groundwater system has drawn concentrated consideration of investigators. It is motivated by the widespread use of engineered NPs in many sectors of engineering, while controlled disposal of such particles has not been well regulated. When leaked into the environment, the NPs are able to migrate into the subsurface, reach aquifers, and contaminate the ground water. This fact has motivated a lot of research on the toxicity of the NPs and their potential risks to the human health as well as to other living creatures. For example, silver NPs have been claimed to be responsible for severe toxicological effects on the male reproductive system, adverse effects on sperm cells, effects on the central nervous system, respiratory effects, and argyrosis[29]. In the same vein, CeO_2 NPs have been reported to have negative impacts on human lung cells causing membrane damage[30]. Together with silver and CeO_2 NPs, the

ecotoxicological effects of other metal-based NPs such as gold, copper, and aluminum NPs have been described in a review of Schrand et al.[31]. Gold NPs at the size of 14nm are toxic to dermal fibroblasts by causing abnormal proteins, which decrease significantly cell proliferation, adhesion, and motility. However, their toxicity is highly sensitive to their size and shape. In the case of copper NPs, severe toxicological effects on the kidney, liver, and spleen of mice have been noticed, while they have promising applications in diverse sectors of engineering. Similar to the gold NPs, the toxicity of copper NPs is size-dependent, which is nontoxic if the particles are of micron size. In contrast, toxicological induction of aluminum NPs varies, depending on which type of aluminum-based NPs between aluminum and aluminum oxide NPs one is exposed to. Aluminum oxide NPs induce limited toxicity, whereas aluminum NPs significantly reduce cell viability, hinder cell phagocytotic ability, and cause toxicological effects on mammalian germline stem cells.

Along with the metal-based NPs, toxicological assessments of carbon-based NPs have been conducted. Magrez et al.[32] studied cytotoxic damage of cultured cells as exposed to CNTs, carbon fibers, and carbon NPs. Generally, they all cause proliferation inhibition and cell death in the order of carbon NPs > carbon fibers > CNTs. The CNTs with functional groups such as carbonyl, carboxyl, and hydroxyl added on their surfaces exhibit higher cytotoxicity than non-functionalized ones. Smith et al.[33] further considered the toxicity of singlewalled carbon nanotubes (SWCNTs) to rainbow trout, and concluded that the SWCNTs are a respiratory toxicant in trout. Changing of the fish behavior, which might be because of gill irritation caused by the SWCNTs was also noticed. Furthermore, their findings have highlighted some new modes of SWCNT

toxicity in fish, and raised concerns about possible SWCNT-induced neurotoxicity and cell cycle defects. Other works done on toxicity assessment of carbon-based NPs and accomplishments can be found in a recent review by Morimoto et al.[34].

Beside the investigation into deep penetration of the engineered NPs in porous media like soil from an environmental standpoint, their transport and kinetics at pore scales also attract interest due to their novel applications in enhanced oil recovery strategies. These strategies encompass a number of chemical treatments using NPs , including reducing mobility ratio between oil and displacing fluids, changing the wettability of rock surfaces at the oil-rock interface, and stabilizing foam for foam flooding[35-37]. If injected into wellbores, due to their nano-size, NPs are believed to be able to travel hundreds of meters away from the wellbores into reservoirs, reaching pockets of trapped oils and carrying out interfacial reactions without impeding the flow or clogging at small pore throats. In association with the chemical methods, innovative thermal recovery using self-heating magnetic NPs is considered as an alternative for traditional steam injection. The magnetic NPs, i.e., ferrite NPs, can absorb external electromagnetic waves with either high or low frequency, and generate heat by changing dipole alignment[38-40]. The alterations in physical properties of NPs open up opportunities to make the reservoirs and fractures visible by imaging contrast agents[41, 42]. Innovative ideas of using NPs as downhole nanosensors are also promising in probing temperature, pressure, and stress of the reservoirs, which will lead to better understandings of the physical properties of reservoirs[41]. However, as mentioned above, if one were to employ NPs, the solution would have to be fabricated in such a way that it is stable under harsh salinity and temperature conditions. Furthermore, it should

exhibit insignificant deposition onto reservoir rock surfaces and should not exhibit size exclusion due to small pore throats.

It is apparent from both standpoints that complete understanding of the mobility of NPs in pore spaces under various physical chemical conditions is important, no matter whether deep penetration of the NPs is desired or undesired. At the lab scale, studies of packed columns are common forms of investigation into the mobility of NPs in porous media. Packing materials in the columns can vary, including granular materials, i.e., quartz sand, or consolidated rock samples, depending on research scope. The columns can be either fully saturated or partially saturated with working fluids, or completely unsaturated. Under such conditions of flow, the mobility of NPs will be explored, coupling with other affecting factors, such as the grain size of packing materials, the NP size, the pH and ionic strength of the working fluid, the surface charge, etc. At the same time with the experimental assessments, predictive models describing the transport and kinetics of NPs have also been developed. These models are useful in obtaining macroscopic kinetic parameters of the nanoparticle-pore suface interaction, leading to upscaling from the lab scale to real reservoir scale.

I.4 Goal of this work

The basic goals of this work are summarized in three bullet points as follows:

- To explore the hydrodynamic responses of an incompressible Newtonian fluid creeping over nanopost arrays, grown from micro channel walls. The hydrodynamic responses include how the velocity profile is deformed by the nanoposts, how long is the recovery length after the deformation (i.e., the distance needed downstream from the nanoposts for the flow to recover to

its fully developed pattern), and how the recovery length would vary with the nanopost array structure. The works done on this topic are in Chapter III.

- To explore the flow-induced stress distributions in structured and highly porous scaffolds, and investigate how geometric factors affect the distributions. The applicability of a predictive PDF for stress distributions in scaffolds with random pore structures, i.e., the three-point gamma distribution proposed by Voronov et al.[43], is considered for use in the examined structured scaffolds. The validity of such PDF at various porosities of the scaffolds is also addressed. The works done are presented in Chapter IV.

- To explore the flow-induced stress distributions in pore spaces, denoted as bulk stresses, of packed-sphere beds, as the bulk stresses provoke aggregate formation of suspended particles, leading to decreasing mobility of the suspended particles by size exclusion and gravitational settling. To a further extent, we want to know if a predictive PDF, which is able to reproduce the bulk stress distributions in the packed-sphere beds, the highly structured scaffolds in Chapter IV, and consolidated sandstones like Berea sandstone exists. This is the content of Chapter V. In Chapter VI, we present a numerical approach using LBM/LPT simulations to model transport and kinetics of suspended NPs in the packed-sphere beds. Results from the modeling approach were validated with column experiments, taking inert glass beads and PMWCNTs as the granular packing material and dispersant, respectively. However, if the PMWCNTs were employed in natural sand-

packed columns, i.e., crushed Berea sandstone, saturated by highly saline solutions, experimental data showed that available filtration models fail to reproduce the breakthrough behavior of the PMWCNTs. Investigation into a new filtration model to address this shortcoming is given in Chapter VII.

CHAPTER II.   NUMERICAL METHODOLOGY

II.1   Lattice Boltzmann method

The LBM is a numerical method to simulate incompressible or compressible fluid flow. Instead of solving the classical Navier-Stokes equation, the discrete Boltzmann equation is solved iteratively. In LBM, the choice of the number of dimensions in space, m, and number of velocity lattice vectors, n, is commonly denoted as $(DmQn)$[44, 45]. The simulations employed herein are D3Q15, and the lattice configuration is shown in Figure II.1.
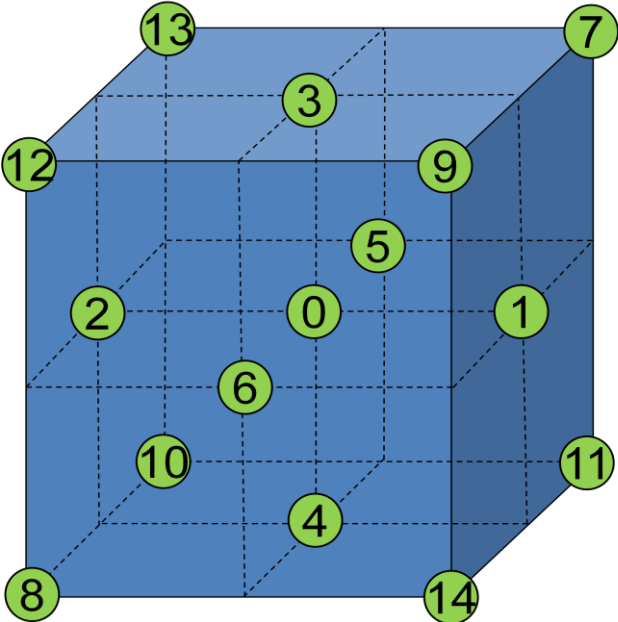
Figure II.1. The cubic lattice of the D3Q15. The associated nodes are classified as following: rest node: 0; class I nodes: 1-6; class II nodes: 7-14.

Because of the inherently parallelizable character of the method in a parallel computer and rather easy implementation, LBM has been used to simulate a wide spectrum of flows (laminar, turbulent, non-Newtonian flows, and multiphase flows)[46]. In addition,

13

according to Chen and Doolen[44], LBM has three main features that make it to be more effective compared to other approaches: (i) the nonlinear convection terms in other approaches can be recovered by the combination of a linear streaming and a relaxation process; (ii) LBM utilizes an equation of state to calculate the pressure whereas a Navier-Stokes solver solves the Poisson equation that often requires special treatment; (iii) calculation of macroscopic properties from the microscopic particle density functions is simple, because a minimal set of velocity vectors is used in LBM. Its numerical accuracy has also been proven to be of second order compared to other numerical methods. Another advantage of LBM is that structured meshes can be used to mesh complex geometries rather than unstructured meshes that are usually used in conventional numerical approaches, like finite volume or finite element methods. No remeshing is needed for each new flow configuration with LBM, and the number of mesh points is not prohibitive (consider for example that over 800,000 computational cells were used to resolve the flow around only a single nanotube in [67] using finite volume techniques).

In the LBM simulation used herein, the geometry is discretized into lattice points (solid walls are described by logical 'TRUE' value and mesh nodes within the void pores are described as logical 'FALSE'). While in the void spaces, fluid particles undergo three steps: propagation, collision, and forcing, in which the particle probability distribution function possesses a different value at every time step, as follows:

$$\underbrace{f_i(\vec{x} + \vec{e}_i \Delta t, t + \Delta t) = f_i(\vec{x}, t)}_{STREAMING} + \underbrace{\Omega_i(\vec{x}, t)}_{COLLISION} \pm \underbrace{f\!f_i}_{FORCING} \qquad \text{(II.1)}$$

14

where f is the particle distribution function, $\vec{x}$ is position, t is time, Δt is the time step, $\vec{e}$ is the microscopic lattice velocity, Ω is the collision operator, ff is the forcing factor, and i is a lattice direction index. The collision process must be characterized by another mathematical model and the single relaxation time approximation model of Bhatnagar-Gross-Krook (BGK) is the simplest and the most commonly used[44]

$$\Omega_i(\vec{x},t) = -\frac{1}{\kappa}(f_i - f_i^{eq}) \tag{II.2}$$

where f^{eq} is the particle equilibrium distribution function and is defined as

$$f_i^{eq}(\vec{x}) = w_i \rho \left[1 + 3\frac{\vec{e}_i \cdot \vec{U}}{c^2} + 9\frac{(\vec{e}_i \cdot \vec{U})^2}{c^4} - \frac{3}{2}\frac{\vec{U}^2}{c^2} \right] \tag{II.3}$$

where $c = \dfrac{\Delta x}{\Delta t}$ is the lattice speed, Δx is the lattice constant, w is a lattice specific weighing factor, and U is the macroscopic velocity. In the BGK collision operator, the relaxation time, κ, is the time scale for the particle distribution function to return to equilibrium, and it is related to the kinematic viscosity of the fluid, ν, as follows:

$$\nu = \frac{1}{3}\left(\kappa - \frac{1}{2}\right) \tag{II.4}$$

The final step in LBM simulation is to back-calculate the macroscopic properties (density ρ and velocity U), from the entire spectrum of discrete microscopic properties (local particle distribution function f_i and microscopic lattice velocity e_i) by applying the conservation equations of mass and momentum

$$\rho = \sum_{i=0}^{n} f_i \tag{II.5}$$

$$\rho\vec{U} = \sum_{i=0}^{n} f_i \vec{e}_i \tag{II.6}$$

where *n* is the number of velocity lattice vectors including the zero position (the rest node) that a fluid particle can stay when it does not move. The simulation mesh consists of *nx*, *ny* and *nz* nodes in the *x*, *y* and *z* directions, respectively. Among these, *fluid* nodes are those within the flow field (i.e., within the empty pore space, given the logical value "FALSE") and *wall* nodes are those that make up the rigid wall (those given the logical value "TRUE"). The velocity field generated by solving the above equations (Equations II.5 and II.6) is equivalent to solving the Navier-Stokes equations for single-phase or multi-phase flows through the pore spaces with 2nd order accuracy[44]. Periodic boundary conditions were applied in all three directions (*x, y, z*). The no-slip boundary condition was applied at the wall faces using the bounce-back technique. In order to take advantage of the LBM parallelizability, the domain was decomposed using message passing interface[26].

The LBM algorithm has been validated for single phase flows in microflows and porous media, and shown excellent agreement[47, 48]. In addition, the precision of the LBM algorithm was further validated by simulating the velocity field of a 5x5μm square channel with no obstacles placed inside. The simulation resolution was chosen to be 0.05μm. The simulation results were compared to exact solutions for flow in ducts that were found in the work of Marco and Han[49]. A very good agreement between LBM results and analytical results was obtained – the maximum velocity and the average velocity obtained from simulations deviated 0.18% and 0.2%, respectively, from the exact solutions (see Figure II.2).
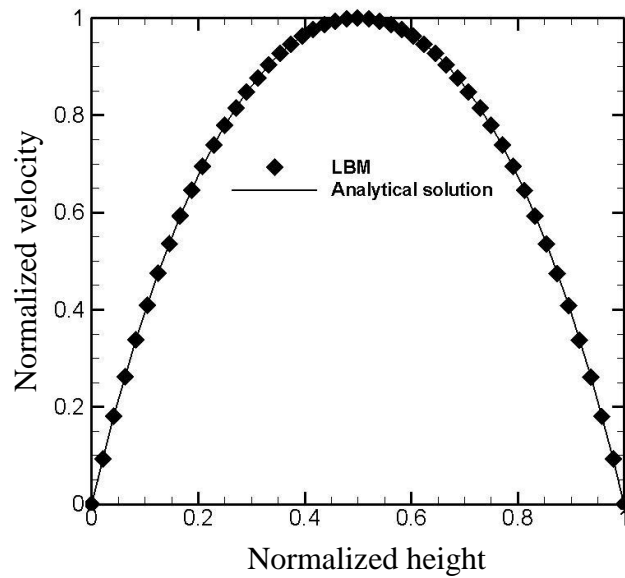
Figure II.2. Agreement of LBM simulation with analytical solution by Marco and Han in generating the velocity profile of water in a 5x5µm square conduit. Velocity data were taken along one of the two shorter axes of the plane, which is perpendicular with flow direction. Velocity was normalized with the maximum velocity, and position was normalized with the channel side.

II.2   Lagrangian particle tracking

This method involves following the trajectory of point particles, released at the inlet of a geometry (see Figure II.3 for illustration), in the Lagrangian framework, as they travel in a certain flow field.
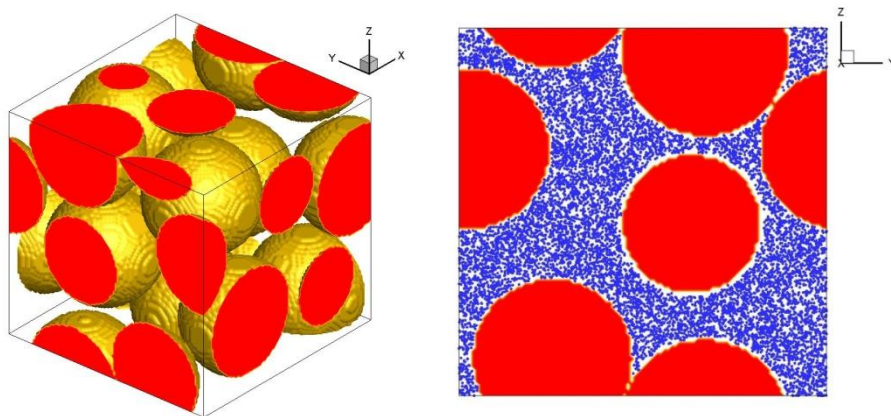
Figure II.3. Left: randomly-packed sphere array; Right: 10,000 particles initially released at inlet of the array.

The particles are assumed to be passive, *i.e.,* they do not affect the flow field, and massless, because the studied dispersed NP suspensions are quite dilute (on the order of 100ppm), so the presence of the NPs is not expected to affect the flow. In the current LPT simulations, the particle-particle interactions are not taken into account. This means that the dispersion of a single particle is not affected by other particles, and that particles do not have a chance to agglomerate and get bigger in size. Given that no particle-particle interaction is considered, the only factor hindering the particle dispersion is deposition. The NP motion, therefore, is a combination of convective transport (contributed by the velocity field that is obtained from the LBM flow simulation) and diffusive transport (contributed by Brownian motion). As a consequence, the equation of motion of particles is mathematically described as follows[48, 50, 51]

$$\vec{X}_{t+\Delta t} = \vec{X}_t + \Delta t \vec{U}_t + \Delta \vec{X} \qquad \qquad (\text{II.7})$$

where $\vec{U}_t$ is the particle velocity at time t and $\Delta \vec{X}$ is the travel distance by diffusive transport. As particles propagate in the flow field, Δt does not change, therefore we employ a static time-stepping approach. The chosen Δt is small enough in order to ensure that particles do not penetrate into the pore wall within one time step. Typically, Δt must satisfy $\Delta t < \dfrac{\Delta x}{U_{max}}$, where U_{max} is the maximum fluid velocity in the open space.

Equation (II.7) provides the new particle position at time $t + \Delta t$ from the old position at time t. It is very rare that the position of a particle would coincide with a computational mesh node, so that it could assume the fluid velocity at that node. In the rest of the

cases, a trilinear interpolation scheme is used to calculate the particle velocity, U_t, at the particle location from the eight neighboring grid nodes.

The Brownian motion of each of the particles is considered to be a sequence of random jumps that are distributed following a normal distribution with zero mean and a standard deviation σ, denoted as N(0,σ). The standard deviation is directly related to the molecular diffusivity with Einstein's theory for Brownian motion that results in the following equation in each of the three space dimensions[48, 52]

$$\sigma = \sqrt{2D_0 \Delta t} = \sqrt{\frac{2\nu\Delta t}{Sc}} \qquad (II.8)$$

where D_0 is the nominal molecular diffusivity, and Sc is the Schmidt number (i.e., the ratio of kinematic viscosity divided by molecular diffusivity). Equation (II.8) accounts for the dependence of the Brownian motion on D_0, which depends on the physical properties of the particle and the fluid. The LPT algorithm has been validated against Taylor-Aris diffusion theoretical predictions in prior work[48]. Because the Taylor-Aris equation is limited within diffusion of particles in a circular conduit, the agreement cannot be extended for more complex flows, i.e., flow in porous media. To add generality to our LPT implementation, hydrodynamic dispersion coefficients of particles dispersing through randomly-packed sphere arrays reported by Maier et al.[53] were reproduced by our LPT simulations, and plotted in Figure II.4 against the reported results for comparison.
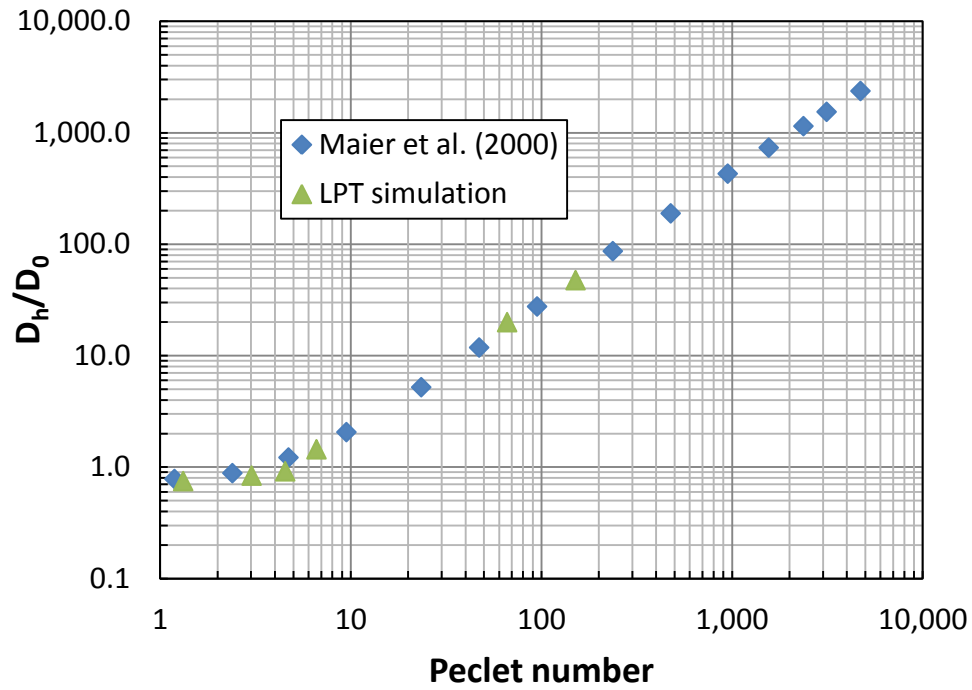
Figure II.4. Dimensionless hydrodynamic dispersion coefficients as a function of Peclet number. D_h/D_0 represents the ratio of dimensional hydrodynamic dispersion coefficient over the molecular diffusivity of the particles.

As evidenced in Figure II.4, results from the LPT simulations follow the same trend as data from from the reference with no significant discrepancies.

In order to simulate wall-particle interactions in our LPT implementation, particles are assigned a probability to be attached by the solid wall upon collision with the wall. Thus, when a particle hits the wall, a random number between 0 and 1 is generated based on a uniform distribution and compared to a predefined attachment probability, p_a ($0 \leq p_a \leq 1$). In order to keep the particle propagating, the random number must be larger than the attachment probability p_a. Otherwise, it will be retained by the solid wall and will remain attached onto the wall. During each simulation, p_a is assumed to be constant, since the injected particle suspensions in the experiments are quite dilute (100ppm). This implies that the amount of injected particles is not enough

20

to cover the wall surface significantly, and the deposited particles do not interfere with the deposition of new particles. In this case, the change in the wall capacity to capture particles is small and can be negligible. Similarly, the same approach is applied to examine whether a deposited particle can escape from the wall and remobilize. Thus, detachment will only occur if the predefined detachment probability, p_d, is larger than or equal to a randomly generated number that follows a uniform distribution between 0 and 1. This second random number is different from that generated in the attachment process. In reality, the attachment and detachment processes can happen at any instant, therefore it is necessary to check the conditions for particle attachment and detachment at every time step of the LPT simulation. Utilizing the predefined p_a values, we can simulate a wide range of solid surface conditions, covering both favorable and unfavorable conditions for particle deposition. In other words, the factors that affect the particle deposition process (such as surface roughness, surface charge, pH, etc.) are reflected by a single parameter, p_a. In analogy, the detachment of deposited particles is determined by the particle detachment probability, p_d, that can be used to predict the tail of the particle breakthrough curve.

CHAPTER III. FLOW RECOVERY FROM NANOPOSTS GROWN AT THE WALL OF A MICROCHANNEL

III.1 Introducion[*]

Since first reported by Iijima[54], CNTs have shown a huge potential for applications in several technological fields. Due to their cylindrical carbon molecular structure, CNTs exhibit unusual physical properties (e.g., thermal conductivity, electric current density, strength, etc.), which are extremely high compared to any other materials[55-57]. Because of very high thermal conductivity, CNTs are believed to be candidates for solving heat transfer issues in high performance electronic devices. Growing vertical CNT arrays on a surface can help to increase the performance of thermal interfacial materials (TIM)[58, 59]. Investigations that have explored the thermal performance of systems employing CNTs as microfins on channel walls have shown a dramatic increase in the amount of heat dissipated compared to bare channel walls. This amount strongly depends on the microcylinder array architecture, such as number of rows and number of columns[60-66]. All of these investigations, however, need to be supplemented with an understanding of the hydrodynamics of the flow around micro-structures, such as posts and cylinders that have been grown in array formation.

Low Reynolds number flow around an array of circular cylinders (both in macroscopic and microscopic scale) has been studied by mathematical models, experiments, and simulations. However, because an array of cylinders or posts can be placed in different formations, it is difficult to obtain a universal solution that can

---

[*]Most of the material presented in this chapter has been published in N. H. Pham and D. V. Papavassiliou, 2014, Nanoscale and Microscale Thermophysical Engineering, **18**(1), 1-17.

successfully describe all possible cases. In the present study, laminar, single-phase flow around nanopost arrays attached to the bottom wall of microchannels with square cross-section is explored by numerical simulation. Since the mean free path for gases is comparable to the size of the nanoposts examined herein, the results apply to the flow of liquids rather than flow of gases.

The height and diameter of the nanoposts are comparable to multi-walled CNTs (MWCNTs). Hydrophobicity effects of the nanopost surface are not simulated, so there is no slip of the fluid on the nanopost surface. Nanoposts are packed in such a manner that the volume fraction occupied by them is very small, and they act simply as momentum sinks, so that none of the other drag coefficient correlations with array volume fraction dependence can be applied. Center to center distance between the nanoposts in the streamwise direction is assumed to be very large, but the effects of the spanwise distance between nanoposts and the effects of nanopost height will be addressed. Nanoposts are further assumed to be rigid and non-deformable under the flow conditions. This assumption is justified based on prior related work [67], where it was calculated that for materials like MWCNTs the deflection is insignificant (about 3.4% of the nanotube diameter at the top of the nanotube) in nanotube array configurations and flow conditions such as those used herein. Furthermore, Battiato et al.[68] showed that the deflection effect is noticeable when the flow velocity is above 5m/s, which is one order of magnitude higher than our highest studied velocity.

III.2 Background and simulation set up

III.2.1   Background

Table III.1 is a summary of work done by several authors in the past five decades for the calculation of normalized drag force per unit length of one cylinder. The literature summarized in this table dealt with macroscopic arrays of infinite circular cylinders with equal diameter and equal center-to-center distance between neighboring cylinders. There is good agreement among analytical solutions with $0 < \Theta < 0.4$ and poor agreement at Θ larger than 0.4, especially when Θ approaches 1. The term Θ reflects how close cylinders are packed in the arrays, as it is the ratio of cylinder diameter divided by the center-to-center distance between two adjacent cylinders.

Table III.1. Literature overview of analytical solutions for calculating drag acting on one circular cylinder in the square array of cylinders. $F/\mu Vh$ denotes the drag per unit length exerted on one cylinder, Θ is the ratio of cylinder diameter to the center to center distance of two adjacent cylinders, R is the cylinder radius, b is the center to center distance of two adjacent cylinders, and Φ is the volume fraction of the cylinders.

Ref.	Expressions		Type of expression	Configuration
[69]	$\dfrac{F}{\mu Vh} = \dfrac{8\pi}{\Lambda_0} + O(\mathrm{Re}^2)$ $\Lambda_0 = 1 - 2\ln(\pi\Theta) + \dfrac{1}{6}(\pi\Theta)^2 - \dfrac{1}{144}(\pi\Theta)^4 + \dfrac{1}{1080}(\pi\Theta)^6$ $\quad - \dfrac{53}{345600}(\pi\Theta)^8 + \dfrac{139}{5443200}(\pi\Theta)^{10} + O((\pi\Theta)^{12})$	*where*	Analytical solution	Flow passed through an infinite row of circular cylinders with same diameter that were placed at equal space from the center of each cylinder.
[70]	$\dfrac{F}{\mu Vh} = \dfrac{4\pi}{\ln\left(\dfrac{b}{R}\right) - \dfrac{b^4 - R^4}{2(b^4 + R^4)}}$		Analytical solution	Flow passed through an infinite square array of circular cylinders with same diameter, placed at equal space from the center of each cylinder.
[71]	$\dfrac{F}{\mu Vh} = \dfrac{4\pi}{\ln\left(\dfrac{2}{\sqrt{\pi\beta}}\right) - 0.75 + \dfrac{\pi}{4}\Theta^2 - \dfrac{\pi^2}{64}\Theta^4}$		Analytical solution	Infinite many circular cylinders that were randomly and homogeneously distributed.
[72]	$\dfrac{F}{\mu Vh} = \dfrac{9\pi}{2\sqrt{2}(1-\Theta)^{5/2}}$		Analytical solution	Flow passed through an infinite square array of circular cylinders with same diameter, placed at equal space from the center of each cylinder.

Table III.1. (Cont.)

Ref.	Expressions	Type of expression	Configuration
[73]	$\dfrac{F}{\mu Vh} = \dfrac{4\pi}{0.5\ln(1/\Phi) - 0.738 + \Phi - 0.887\Phi^2 + 2.038\Phi^3 + O(\Phi^4)}$	Analytical solution	Flow passed through an infinite square array of circular cylinders with same diameter, placed at equal space from the center of each cylinder.
[74]	$\dfrac{F}{\mu Vh} = \dfrac{8\pi}{\ln(1/\Phi) - 1.47633597 + \dfrac{2\Phi - 0.7589781\Phi^2}{1 + 0.48919241\Phi - 1.60486942\Phi^2}}$	Analytical solution	Flow passed through an infinite square array of circular cylinders with same diameter, placed at equal space from the center of each cylinder.

However, this parameter is not appropriate for our cases, because the center-to-center distance in the streamwise direction is different than that in the spanwise direction, as stated earlier. The applicability of the above mentioned results to microscale systems still needs to be explored further both with continuum and subcontinuum models.

Both molecular based and continuum based methods have been used in the past to examine similar flow systems. Walther et al.[75], using nonequilibrium molecular dynamics simulation, investigated flow behavior around the vicinity of arrays of infinite CNTs. In that case, drag coefficients were in very good agreement with those obtained with the Stokes-Oseen solution, which is a solution obtained based on the continuum assumption for fluid mechanics. The opposite conclusion was reached in the work of Tang and Advani[76] when they used a similar molecular dynamics simulation approach to study uniform liquid argon flow past a finite CNT. Significant differences between drag coefficients calculated from their simulations and a macroscopic empirical correlation proposed by Huner and Hussey[77] indicated that the flow behavior is fundamentally different at the nanoscale level.

For the case of arrays with nanocylinders of finite length, numerical work by Ford and Papavassiliou[67] with the use of finite volume methods showed a discrepancy of up to 25% between two patterns of rigid CNTs attached on a surface: nanotubes attached in a straight line and in a forest formation. Battiato et al.[68] studied the flexibility of CNTs when elastic response to fluid flow was taken into account. Analytical solutions for the velocity profile and drag coefficient were obtained after solving the Navier-Stokes equation and the Brinkman equation simultaneously. Yeom et al.[78] took the effects of channel walls into account by investigating a finite array of

cylindrical microposts that were confined between two walls. Their results indicate that the drag force per unit length acting on each micropost can be found from a newly proposed correlation. This equation was a combination of Kuwabara's model[71] and Keller's model[72] when the effects of aspect ratios were neglected. The nanocylinder arrays (or microcylinder arrays) in the above mentioned studies had a significant volume fraction compared to the entire volume of the channels and each cylinder was placed in equal center to center distance. Effects of the cylinder length on the flow field as well as the contribution of the side walls of the channel to drag forces acting on nanocylinder arrays have not yet received enough attention.

III.2.2   Simulation setup

A fluid having a viscosity of 0.001Pa.s and density of 998kg/m^3, which is equivalent to that of water, was forced through microchannels with square cross-section and infinite length. A line of nanoposts with diameter D = 50nm was packed at the center of a periodic unit and nanopost height and distance between each individual varied on purpose. See Figure III.1 for a schematic of the computational domain.
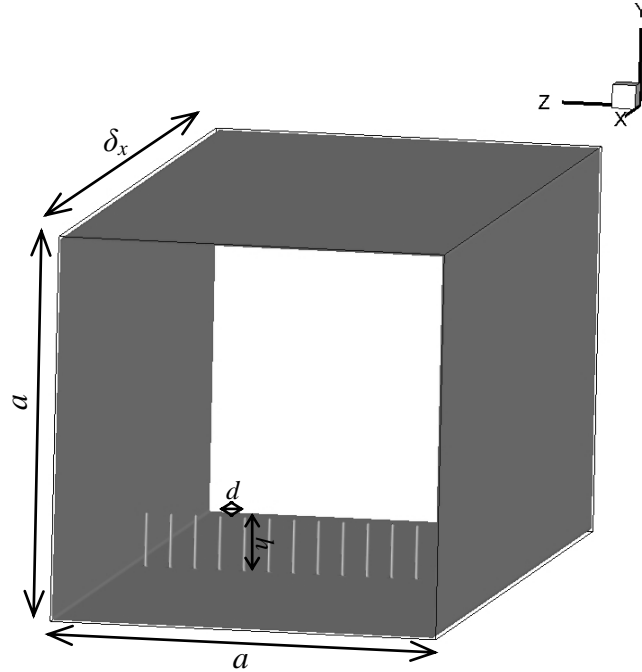
Figure III.1. A periodic unit of a micro square channel with a line of nanoposts located in the middle of the channel. The unit length, δ_x, was 15μm and remained constant at different simulations. The distance between each nanopost, d, was varied from 0.1μm to 0.7μm and the nanopost height, h, was varied from 0.5μm to 3.5μm. This implies that the nanopost aspect ratio was between 10 and 70.

The Reynolds number, Re, in this work is defined as

$$Re = \frac{aU_S}{\nu} \qquad\qquad (III.1)$$

where U_S is the superficial velocity and a is the size of the side of the square channels. Simulation results were mainly obtained from a square channel with $a = 5$μm. Numerical simulations in two other square channels, one with smaller side (4μm) and another one with larger side (7μm), were also performed for validating the results. The length of the periodic computational domain was 15μm and the simulation resolution was 0.05μm for all the simulations. In other words, the grid size of three different channel sizes was 82x82x301, 102x102x301, and 142x142x301 for the 4x4μm, 5x5μm,

and 7x7µm channels, respectively. The resolution was chosen so that the nanoposts with D = 50nm were treated in the simulation as line sinks of momentum, since they were simulated as lines of one grid point in diameter. The choice of nanopost diameter and grid resolution has limited the ability of our simulation to simulate gas flow through the microchannels. This is because the nanopost diameter is comparable with the mean free path of gases, and the continuum assumption might fail in such cases. Simulations at sub-continuum level are required if one wants to simulate the flow of gases in the current configurations. Nonetheless, this is out of the scope of our work, since we want to concentrate on the physics of liquid flows in micro channels for efficient removal of heat in high performance micro devices application.

Three different Re were considered, having the values of 0.0877, 0.438, and 2.19. Note that the reported Re is based on the channel size rather than cylinder diameter, as was done in prior work for cylinders in infinite flow domains[69-74]. When flow passes through a nanopost line, these "obstacles" (or line sinks of momentum) deform the flow field and turn it into a developing flow downstream from the posts. As we deal with a very small volume fraction of nanoposts, flow might have enough space to reform the fully developed pattern before being deformed again by other nanoposts downstream. Therefore, knowing the needed distance for fluid flow to retake its fully developed profile after passing through a nanopost line is important. That is the reason why we introduce the recovery length, L, and this is the distance at which the velocity can recover 99% of its fully developed value. In our simulation, this length is mathematically defined as the distance downstream of the posts, where the following condition is satisfied:

$$\max\left(\frac{\left|u_{I,J,K} - u_{I+1,J,K}\right|}{u_{I,J,K}}\right) < 0.01 \qquad\qquad\qquad\text{(III.2)}$$

where I, J, and K are discrete nodes in x, y, and z direction, respectively. It is expected to be a function of the nanopost height, h, the center-to-center distance between nanoposts, d, of a, and of Re of the free stream.

No slip boundary condition is applied at fluid-solid interfaces and this condition is achieved by applying the half-way bounce back technique, in which a fluid particle will return to its original position with opposite direction if it hits the wall[45]. Nanoposts are assumed to be hydrophilic in this study, so that fluid layers that are in contact with the nanopost surfaces are not repelled. Also, periodic boundary conditions are used at inlet and outlet to simulate an infinite channel.

III.3 Results and discussion
III.3.1 Recovery length

In Figure III.2 we plot the velocity pattern at the plane where nanoposts were packed. The non-parabolic velocity profile indicates a deformation of the flow field, even when only 6 nanoposts were packed at 0.7μm away from each other. Because of no slip boundary condition at the nanopost-fluid interfaces, the fluid velocity at the nanopost faces is immediately reduced to zero. Therefore, other fluid layers have to accelerate in order to not violate conservation of mass.
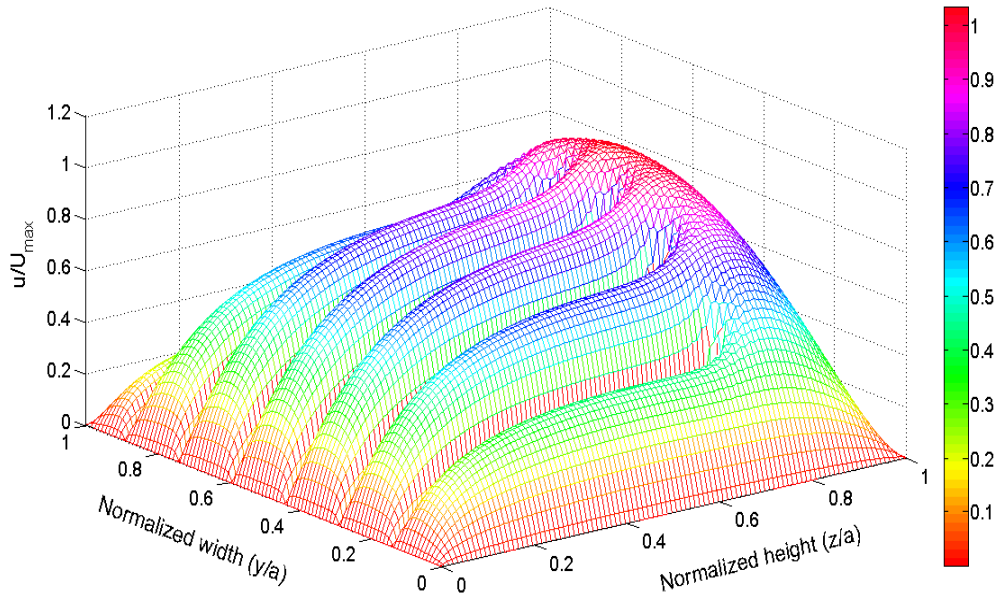
Figure III.2. Velocity profile at the plane containing the nanopost line and perpendicular to the flow direction. The side of the square channel side is 5μm and the nanopost height is 3.5μm. Each individual in the nanopost line is packed at 0.7μm away from the others and the flow is in the creeping regime with Re = 0.438. The fluid velocity in the *x* direction is normalized with maximum *x*-velocity when it reaches the fully developed pattern.
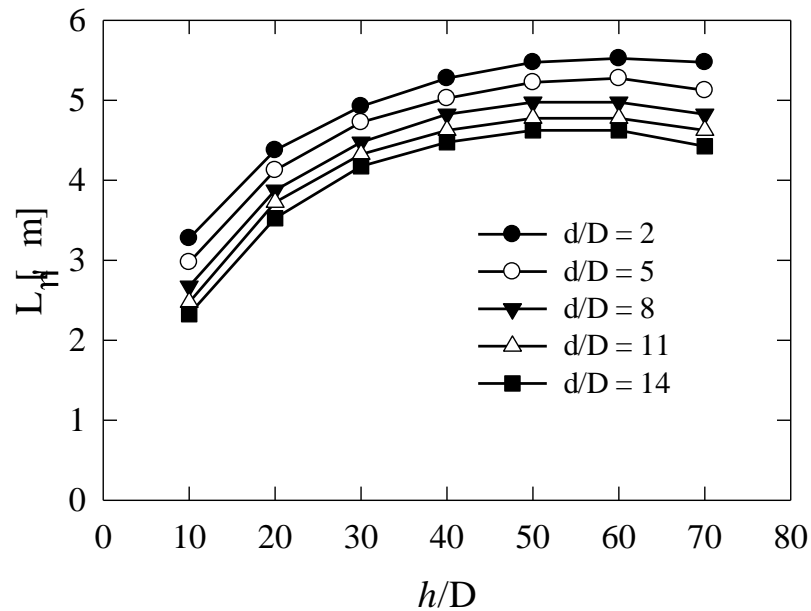
Figure III.3. Dependence of recovery length on dimensionless nanopost height at constant Re. Data were taken at Re = 0.0877. Simulations were done using 5μm-side channel.

32

This acceleration can be noticed from the maximum x-velocity in this plane, which is 1.033 times higher than the maximum X velocity of the recovered fully developed profile. Because the computational domain is periodic, the flow pattern showed in Figure III.2 is exactly the same at other planes that contain nanopost lines downstream.

Figure III.3 is an illustration of the relation between recovery length, L, and dimensionless nanopost height, h/D, at Re = 0.0877, and at different dimensionless spacing between two nanoposts, d/D. The behavior is clear: the higher the nanoposts, the longer the distance it takes to fully recover the fully developed shape, and one can predict this trend prior to conducting any simulations. The increase of L seems to be exponentially proportional to the increase of h/D. However, when h is larger than half-height of the duct, L slowly changes over the rest data points. This phenomenon can be explained by the contribution of the top of the nanoposts to flow deformation effects (this effect will be referred to as "top effects" from now on). It is apparent that the top effects, together with trailing edge effects, will grow with nanopost aspect ratio in free shear flow around nanoposts attached to the surface. When the flow is confined within four channel walls, however, the above mentioned proportional increase still holds at some nanopost heights that are significantly less than the channel half height. After that, the top effects will not be noticeable. When nanoposts extend to the top half of the channel, and reach towards the top wall of the channel, the effects of trailing edge of nanoposts and top and bottom walls are most prominent. It turns out from the simulation data that a modified exponential function of the form

$$L = B_1 \exp(-B_2 D/h) \qquad\qquad\qquad (III.3)$$

33

can successfully fit the simulation data where B_1 and B_2 are two constants that depend

on d and Re. The choice of this function is not arbitrary, but it has physical meaning.

The length L will depend on B_1 only when h tends to infinity. This is similar to the case

of flow passing through an array of infinite cylinders and L will change with changes in

either d or D.

The effects of space between nanoposts on the recovery length at different

nanopost aspect ratios are presented in Figure III.4.
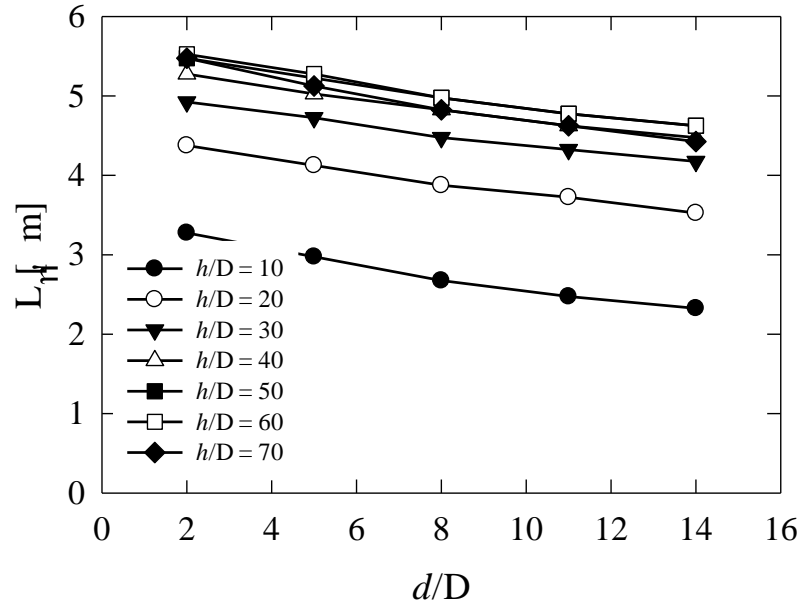
Figure III.4. Changing in recovery length when distance between two nanoposts is varied. This is the case for Re = 0.0877 and 5μm-side channel.

Simulations were again conducted in the creeping flow regime with Re = 0.0877. It can

be inferred from Figure III.4 that the closest packing of nanoposts (d/D = 2) causes the

longest L, whereas shortest L is caused by the farthest distance between two nanoposts

(d/D = 14) at a specific nanopost aspect ratio. Another conclusion inferred from Figure

III.3 and Figure III.4 is that recovery length is more sensitive to nanopost height than it

is to distance between individual nanoposts. Again, we see an exponential relation with a negative exponent rather than a linear dependence. Choosing

$$L=B_3\exp(-B_4d/D) \tag{III.4}$$

leads to L = 0 when d goes to infinity. This is reasonable because L = 0 means no nanoposts will be present in the flow field, so that we have no flow deformation effects. At $d = 0$, the physical meaning is that this is the case of flow past a solid wall of nanoposts and the recovery length will be dependent on the height of the nanopost wall.

The effects of different flow conditions on the recovery length are addressed next, since these effects are thought to be partially responsible for the distance that flow reforms. To investigate these effects, all other variables (d, h, a) were kept constant to fully isolate their contribution to the results. At each nanopost aspect ratio, three different simulations were carried out corresponding to three different Re, and the Re was varied by changing the driving force (pressure difference) rather than the size of the square channel. Interestingly, the results are independent from the variation of Re (see Figure III.5).
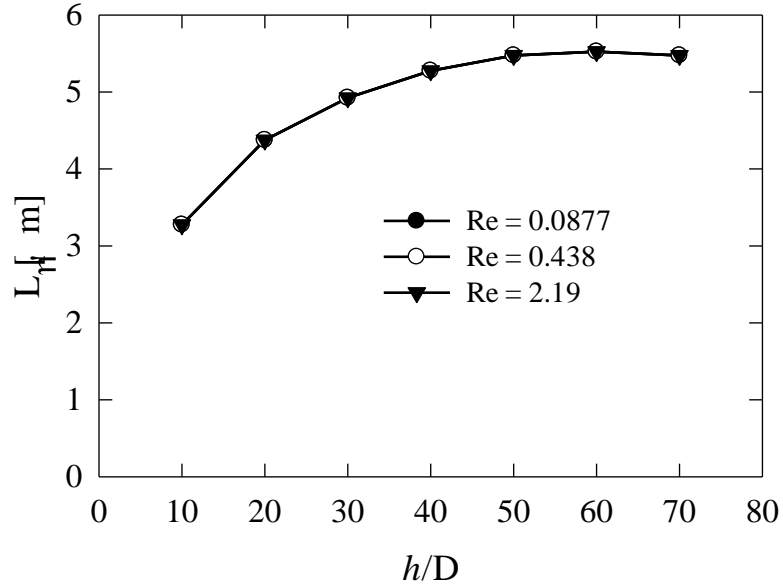
Figure III.5. Recovery length at different Re. This is the case when dimensionless distance, *d*/D, between individual nanoposts is 2 and the channel side is 5μm.

Our definition for recovery length is in analogy with the entrance length and one might expect a change in recovery length at different Re as usually seen for the entrance length. However, our finding indicates that for confined creeping flow over a nanopost array attached to a channel wall, the configuration of the array (such as *a, h* and *d*) is the unique factor that affects the length of recovery. Although this conclusion contradicts intuition, which says that entry length, and by extension recovery length, should be a function of configuration variables and Re, it is consistent with one of the most well-known classical fluid mechanics problem: flow around an infinite circular cylinder. The analytical solution for this problem is given in fluid mechanics text books as follows[79]:

$$\frac{V_r}{U_\infty} = \left(1 - \frac{R^2}{r^2}\right)\cos\theta \qquad (III.5)$$

$$\frac{V_\theta}{U_\infty} = -\left(1 + \frac{R^2}{r^2}\right)\sin\theta \qquad (III.6)$$

36

where V_r is the radial velocity, V_θ is the angular velocity, U_∞ is the constant free stream velocity, R is the cylinder radius, r is the radial distance, and θ is the azimuth. From Equations (III.5) and (III.6), the ratio of radial velocity to free stream velocity as well as angular velocity to free stream velocity is a function of the three geometric variables, namely the cylinder radius, the radial distance, and the azimuth. This implies that velocity magnitude of the free stream plays no role in the recovery distance of flow both in the case of infinite and finite cylinder.

Our goal is to obtain an empirical correlation that can predict, in general, the recovery length based on key configuration variables. An exponential form has been proposed for variation of L with either d/D or h/D (see suggested Equations III.3 and III.4). It is apparent that the final form of the correlation will inherit these features also presenting an exponential behavior. All the physical meaning discussed above has to be maintained. The expression of recovery length and dimensionless nanopost height takes the form L=B_1exp(-B_2D/h) where the dependence of B_1 and B_2 on dimensionless space (d/D) needs to be examined. The data presented in Figure III.3 allow us to perform data fitting of B_1 and B_2 over the studied range of d/D reaching a final correlation as follows:

$$\frac{L}{D} = 125\exp\left(-0.012\frac{d}{D} - 0.131\frac{d}{h} - 6.1\frac{D}{h}\right)$$

(III.7)

Note that the dependence on the channel size is missing from the above equation. Hence using the given expression for other square channels with a channel side either bigger or smaller than 5µm is inadequate. In order to include the channel size into Equation (III.7), the same amount of work needs to be replicated with many different square channel sides, and this, of course, is computationally time consuming. Fortunately, we have discovered that the channel side can be included in the expression

37

by introducing the so-called equivalent side, a_e, at the cross section of the square channels that contains the nanoposts. This equivalent side is equal to the square root of the void area of that cross section and is mathematically stated as follows:

$$a_e = \sqrt{a^2 - \Pi h \text{D}} \tag{III.8}$$

where Π is the number of nanoposts in the line.

After refitting the data, Equation (III.7) takes the form

$$\text{L} = 2.64(a_e)^{0.54} \exp\left(-0.012\frac{d}{\text{D}} - 0.131\frac{d}{h} - 6.1\frac{\text{D}}{h}\right) \tag{III.9}$$

The accuracy and applicability of Equation (III.9) are tested by comparing L calculated from Equation (III.9) (denoted by L_{cal}) and L obtained from simulations. Two other square channels, one with bigger side (7μm) and one with smaller side (4μm), were simulated at two distinct values of d (0.1μm and 0.4 μm), and each value of d was simulated with two cases of h/D (20 and 40). Simulation data from three different channel sizes were then put on the same plot, along with the data obtained from Equation (III.9) for comparison (see Figure III.6).
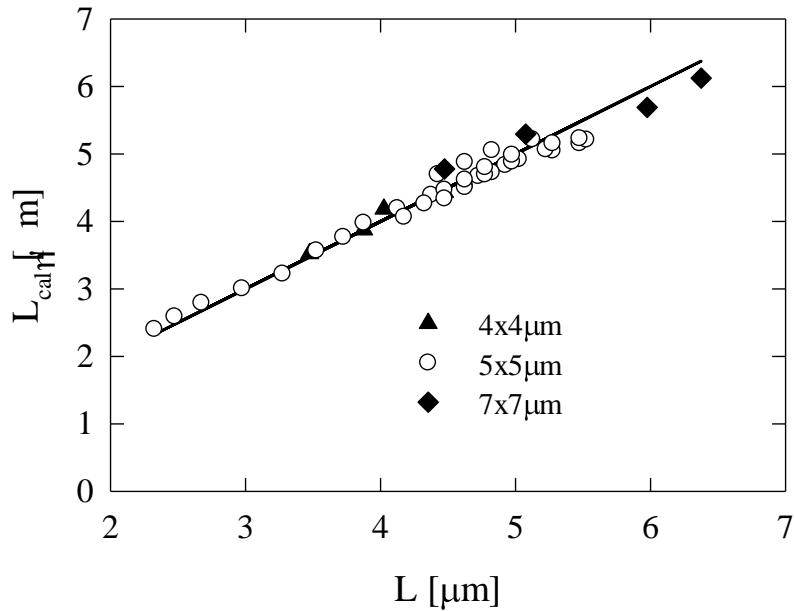
Figure III.6. Deviation of recovery lengths calculated from Equation (III.9) from the actual recovery lengths obtained from numerical simulations. The solid line which passes through the origin and has the slope of 1 represents $L_{cal} = L$, while the symbols are the actual data that were collected from simulations for three different channel sizes.

Accordingly, L_{cal} data deviate within $\pm 7\%$ from the simulation results, and these small deviations prove that the proposed correlation can successfully predict the recovery length of flow passing through an array of nanoposts grown from the bottom wall of square channels at different channel sizes.

III.3.2 Drag coefficient and appropriate Reynolds number

It is important to note that energy loss due to friction drag is proportional to the number of nanoposts that are packed in the square channels. Thus, it is useful to explore how much flow resistance will be generated at different flow conditions and array configurations in our study. Resistance to flow around an immersed object (or object moving inside a fluid environment) is usually expressed through the drag coefficient, C_D, which is defined as

39

$$C_D = \frac{F}{\frac{1}{2}\rho V^2 A} \tag{III.10}$$

where F is the drag force exerted on the object, V is a characteristic velocity, and A is the projected area normal to flow. The total drag force exerted on nanoposts can be known from our simulation by numerical integration of the flow-induced stresses at the nanopost surface. The stress tensor was first estimated as the product of the rate of strain tensor and the fluid dynamic viscosity

$$\underline{\underline{\tau}} = \mu(\nabla\underline{U} + \nabla\underline{U}^T) \tag{III.11}$$

where $\underline{\underline{\tau}}$ is the stress tensor, μ is the dynamic viscosity of the fluid, and $\underline{U}$ is the velocity vector. Then, the largest eigenvalue of this symmetric matrix was calculated and this largest eigenvalue was then considered to be the value of the flow-induced stress (see Porter et al.[80] and Voronov et al.[43]). Drag coefficients known from the empirical correlation proposed by Ford and Papavassiliou[67] for flow around an infinite linear array of finite nanotubes attached to a solid surface and drag coefficients calculated from the Stokes-Oseen's equation for the case of flow passing through an array of infinite cylinder are two possible cases that can produce results for comparison with our simulation data. The Stokes-Oseen equation (Equation III.12)[75] and the correlation of Ford-Papavassiliou (Equation III.13) are given as follows:

$$C_D = \left(\frac{8\pi}{Re_{S-O} \ln(7.4/Re_{S-O})} \right) \left(\frac{3 + 2\Phi^{5/3}}{3 - \frac{9}{2}\Phi^{1/3} + \frac{9}{2}\Phi^{5/3} - 3\Phi^2} \right) \tag{III.12}$$

$$C_D = \frac{48.62}{Re_{F-P}^{0.806}} \tag{III.13}$$

where Φ is the volume fraction of the array, $Re_{S-O} = \dfrac{VD}{\nu}$ is the Re used by Stokes-Oseen, and $Re_{F-P} = \dfrac{V\sqrt{Dh}}{\nu}$ is the Re used by Ford-Papavassiliou

The comparison is illustrated in Figure III.7 where a big gap is noticeable.
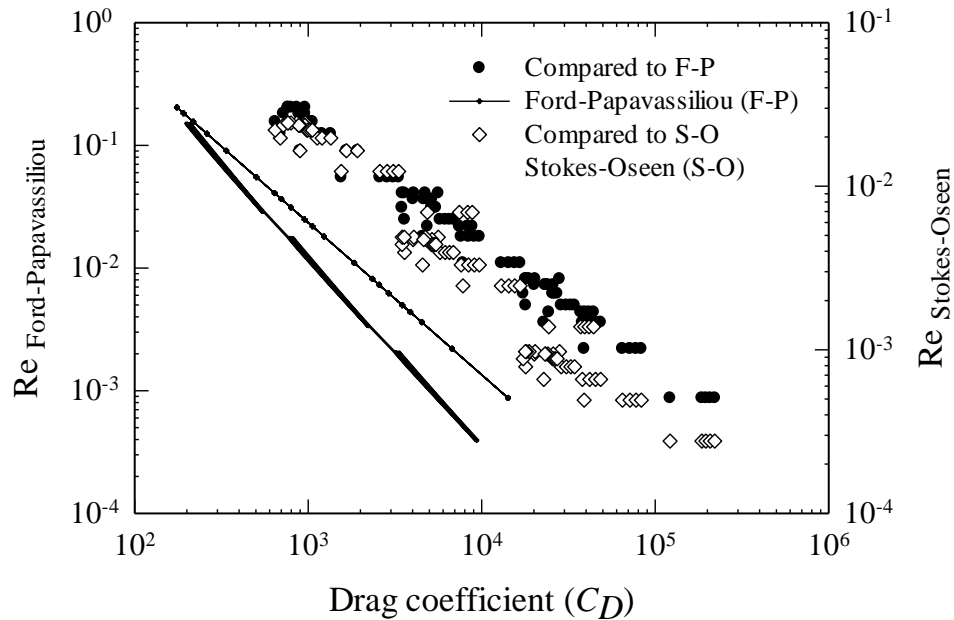
Figure III.7. The comparison of drag coefficient calculated from the Stokes-Oseen equation and Ford-Papavassiliou's empirical correlation to presently obtained simulation data (simulation data were collected from all simulations that were done in this study). The circles repesent simulation data to compare to the Stokes-Oseen equation, whereas the diamond symbols are data to compare with Ford-Papavassiliou's empirical correlation. Both Stokes-Oseen's equation and Ford-Papavassiliou's correlation underpredict the actual drag coefficients.

It is apparent from Figure III.7 that both the Stokes-Oseen equation and Ford-Papavassiliou empirical correlation under-estimate the simulation data. This comes from the fact that flow in a closed conduit is being considered here, and this will result in a parabolic velocity profile instead of ideally flat velocity profile as in Stokes-Oseen's equation. Although Ford and Papavassiliou took this parabolic profile into account, the applicability of their empirical correlation is limited by investigating only

41

constant height of nanotubes and constant distance between neighboring nanotubes. Furthermore, their channel was 2-dimensional, open sides, and was constructed in a way that effects of the top wall were neglected. In order to establish a new empirical correlation of drag coefficient valid for our case, a new Re that accounts for the channel size and nanopost characteristic height was introduced, as follows

$$\mathfrak{Re} = \frac{ah}{D}\frac{\mathrm{U_S}}{v} \tag{III.14}$$

Drag coefficients obtained from different simulations were collected and plotted together with $\mathfrak{Re}$ calculated from Equation (III.14) in Figure III.8.
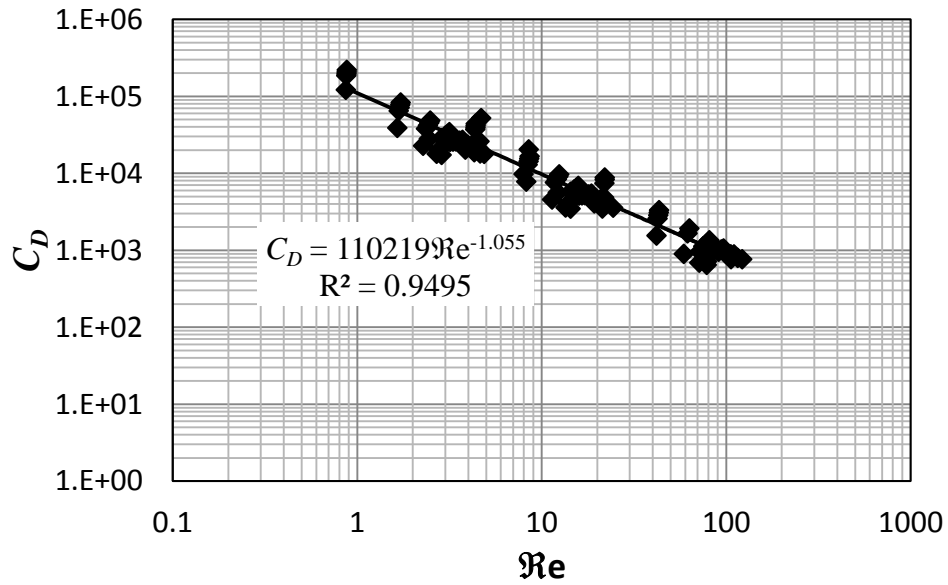
Figure III.8. Drag coefficients gotten from numerical simulations relative to appropriately defined Reynolds number. The relation was found to be $C_D \sim 1/\mathfrak{Re}$.

The relation for the drag coefficient to the newly defined Re is found to be

$$C_D \sim 1/\mathfrak{Re}^{1.055} \tag{III.15}$$

which is approximately identical to the 1/Re dependence that has been well-known for the case of flow around an infinite cylinder at low Re[81].

CHAPTER IV. STRESS DISTRIBUTION STRUCTURED SCAFFOLDS

IV.1 Introduction[†]

Currently, in the US, almost 10% of deaths are caused from lacking compatible organs for transplantation[82]. Driven by tissue and organ shortage, tissue engineering has emerged as an alternative to transplantation for the reconstruction of lost or damaged organs. For bones, the regeneration process involves seeding of biodegradable scaffolds with pre-osteoblastic adult stem cells (e.g., mesenchymal stem cells, adipose derived stem cells etc.) obtained from the patient, culturing of the cells *in vitro* to grow bone tissue, and re-implantation to the patient[83]. These scaffolds, which must satisfy the four fundamental qualities of form, function, formation, and fixation as described in [23], typically have high porosity (over 75%) and high surface to volume ratios, in order to allow the seeding and proliferation of cells within their pore space during the culture stage.

These constructs are typically cultured dynamically in flow perfusion bioreactors, because cells in their natural environment experience moderate cyclic mechanical loading, and their growth is known to be stimulated by flow-induced stresses[27, 84-87]. Average stress in the range of $0.1 - 25 dyn/cm^2$ is reported to correspond to increased cell proliferation[87]. On the other hand higher stresses (in the range of $26 - 54 dyn/cm^2$) can cause cell detachment (since 75% of cells are attached in a bridged morphology,[88]), and/or cytolysis[89]. Therefore, knowledge of flow-induced stresses

---

[†]The work presented in this chapter appeared in N. H. Pham, R. S. Voronov, S. B. VanGordon, V. I. Sikavitsas, and D. V. Papavassiliou, 2012, Biorheology, **49**(4), 235-247.

experienced by the seeded cells in scaffolds is important for a successful artificial bone tissue culture.

Stress distributions within scaffolds can be estimated with computational fluid dynamics (CFD) simulations, or measured using sophisticated and costly experiments[80, 86, 90-95]. Interestingly, however, Voronov, VanGordon, Sikavitsas and Papavassiliou[43] observed that a single statistical distribution is followed by surface stresses within highly porous, randomly structured scaffolds (the work of Voronov et al. will be referred to as VVSP from now on).

Briefly, VVSP used micro-computed tomography in conjunction with LBM simulations to calculate flow-induced wall stresses within 36 different highly porous bone tissue engineering scaffolds (porosity was varied from 80% to 95%) prepared via salt leaching[47, 96, 97]. They found that the flow-induced stresses followed a PDF that was very similar for all scaffolds. In fact, VVSP tested 65 different PDF types to find that a single three-parameter gamma (gamma-3P) PDF was the best statistical fit for all these scaffolds. The three-parameter gamma PDF [usually designated as $\Gamma(\bar{\alpha}, \gamma, \beta)$] is defined as

$$\mathrm{f}\!\left(\tau_W^*\right) = \frac{\left(\tau_W^* - \gamma\right)^{\bar{\alpha}-1}}{\beta^{\bar{\alpha}}\,\Gamma(\bar{\alpha})}\,exp\!\left[-\left(\tau_W^* - \gamma\right)\!/\beta\right] \qquad\qquad \text{(IV.1)}$$

where $\bar{\alpha}$ is the shape parameter, β is the scale parameter, γ is the location parameter, and $\Gamma(\bar{\alpha})$ is a complete gamma function. In the case of $\gamma = 0$, the distribution becomes the standard gamma distribution $\Gamma(\bar{\alpha}, 0, \beta)$, i.e., the two-parameter gamma distribution. VVSP found that $\bar{\alpha} = 2.91$, $\beta = 0.45$, and $\gamma = -1.43$ provided the best overall fit for the surface stress PDFs obtained from their LBM simulations, when the stress on the fluid-

solid surface was normalized by subtracting the mean stress, $\bar{\tau}_w$, and dividing by the

standard deviation, σ_τ, of the stress distribution, as follows:

$$\tau_W^* = \frac{\left(\tau_W - \bar{\tau}_W\right)}{\sigma_\tau} \qquad \text{(IV.2)}$$

They also found that the $\Gamma(2.91,-1.43, 0.45)$ PDF fit within statistical accuracy (at a

20% significance level based on a goodness of fit statistical test) PDFs of stresses

obtained in highly porous scaffolds of different types (such as non-woven fiber mesh

scaffolds) and PDFs published by other laboratories that were obtained either through

simulations or by experiments[91, 92, 98].

The VVSP finding (applicable for random and highly porous media), if further

understood, would allow the possibility that flow-induced wall stresses within scaffolds

can be predicted analytically, within statistical accuracy. The motivation of this study is

to explore whether a common stress distribution exists for porous media with structured

architectures, such as those that can be obtained with prototyping techniques. The goal

is to compute the normalized flow-induced wall stress distribution in scaffolds that have

an ordered internal architecture (e.g., scaffolds with regular, repeated geometric shapes

as opposed to those that have a random architecture, like in VVSP), since it is often

desired to control the architecture of the porous medium[26, 99, 100]. In order to do that we

also have to answer the following questions: (a) Does the VVSP distribution describe

the stresses within different types of highly porous media consisting of regular

geometries? And if it does not, what is the underlying reason for its failure? (b) Are

there any conditions that need to be satisfied in order for this distribution to work? (c)

Does it work for scaffolds with oriented geometry, but lower porosity? Findings from

this work can help to anticipate the wall stress distribution when designing scaffolds with ordered architecture, and can also help in determining the best operating conditions for a perfusion bioreactor. Recent efforts to optimize the scaffold architecture in terms of yielding controlled and specified shear stress distributions[101] are also going to benefit from results presented herein.

IV.2 Methods

Prior simulations appearing in VVSP were conducted with LBM. In the present study, we used commercial software in order to scrutinize the VVSP results with a different numerical methodology. Numerical experiments were carried out by the finite volume-based CFD software FLUENT, version 12.0.16. Periodic boundary conditions were applied at the flow inlet and outlet (the YZ inlet and outlet planes, as seen on Figure IV.1) in order to simulate an infinite, periodic medium, while symmetry was used in the other two directions (XY and XZ planes).
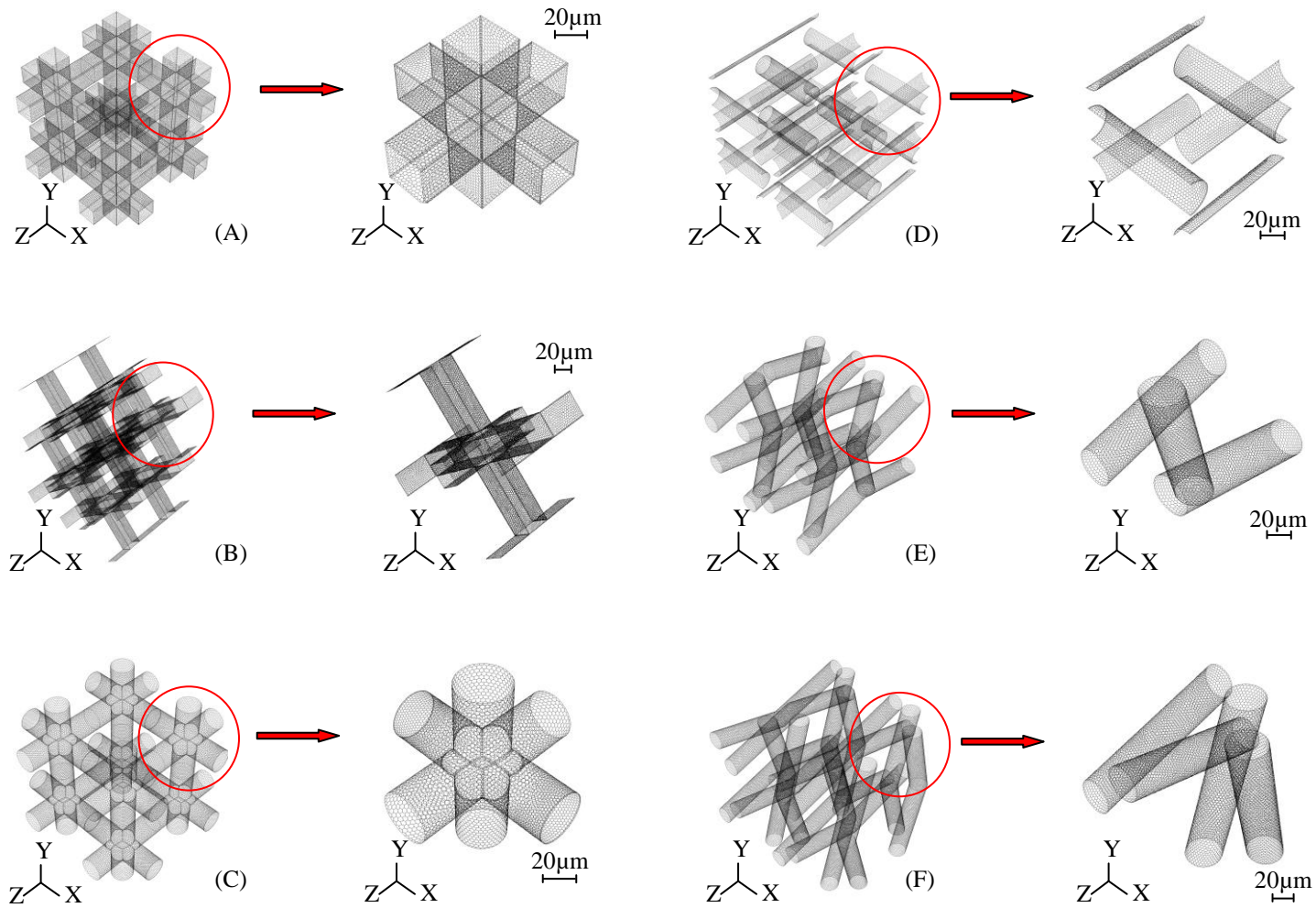
Figure IV.1. Internal architecture of the different scaffold types simulated. The panels to the right depict the periodic unit cell simulated in each Case, from A to F.

A fluid having a viscosity of 0.001Pa.s, which is equivalent to that of water, was driven through the media by a pressure gradient of 100,000Pa/m. The use of water properties to represent the culture medium is a reasonable choice[90, 92, 102], and the actual value of the pressure gradient is not crucial, since laminar flow through porous media is a linear process and the results are normalized with average values. Six different porous media geometries were created and meshed with GAMBIT 2.3.16. Tetrahedral elements were firstly used for meshing and then converted to polyhedral elements when imported to FLUENT in order to minimize computational time[103]. Simulation tests with tetrahedral and with polyhedral meshes gave the same results. Grid-independence was verified by initially creating a geometry with 223,109 grid cells (configuration such as shown in Figure IV.1A) and then increasing the number of grid cells by a factor of 2, 4, 5, and 10. The average shear stress, computed from each case, changed less than 1% even when the number of grid cell was ten times higher. Hence geometries with about 220,000 grid cells were used for the rest of the simulations.

All of the media in the first part of this study were constructed to have a porosity of 85%, in order to control for this parameter. The solid region was assumed to be rigid and stationary. Table IV.1 is a summary of the geometric characteristics of the six porous media used in this study, described below in more detail:

- CASE A – the periodic unit cell contains three similar bars with square cross section that intercept each other perpendicularly at their respective midpoints. Flow is in X direction, which is parallel to the direction of one of the bars and perpendicular to the other two (see Figure IV.1A).

48

- CASE B – the unit cell contains the same bars as Case A, but the direction of the flow is rotated such that the fluid flow meets the perpendicular bar edge-first, and has a 45° angle with the other two bars. Flow is in the X direction, as shown on Figure IV.1B.

- CASE C – the unit cell is the same as in Case A, but the cross section of the bars is circular. The flow direction is the same as in Case A, as seen on Figure IV.1C.

- CASE D – the unit cell contains four cylinders oriented parallel to the Y axis and perpendicular to the direction of flow (X direction). Another two cylinders (one on top and one at the bottom) are parallel to the direction of flow, as seen on Figure IV.1D.

- CASE E – the unit cell contains two cylinders oriented parallel to the Z axis, and rotated in opposite directions to each other about the X axis. A third cylinder is situated on the YZ plane and has a 15° angle with the Y axis. Flow is in the X direction (see Figure IV.1E).

- CASE F – the unit cell is similar to Case E, but has four cylinders. All four cylinders are located on the YZ plane, with two of them rotated in opposite directions to each other about the X axis, such that they have a 15° angle with the Y axis. Similarly, the other two cylinders have a 15° degree angle with the Z axis. Flow is in the X direction (see Figure IV.1F).

Table IV.1. Geometry configuration of six different constructed porous media

	Case A	Case B	Case C	Case D	Case E	Case F
Domain size [μm^3]	143.2^3	$202.5^2 \times 143.2$	127^3	113.26^3	141.14^3	162.97^3
Porosity ϕ [%]	85	85	85	85	85	85
Cylinder diameter [μm]	-	-	35	35	35	35
Edge of bar cross section[μm]	35	35	-	-	-	-
Surface area to volume ratio A_s/V [$1/\mu m$]	0.015476	0.015477	0.002563	0.01714	0.017143	0.01714
Superficial velocity [m/s]	0.036758	0.035617	0.031555	0.023096	0.035885	0.038207
Permeability k [m^2]	3.7×10^{-10}	3.6×10^{-10}	3.2×10^{-10}	2.3×10^{-10}	3.6×10^{-10}	3.8×10^{-10}

The configurations of the scaffolds described above were inspired by published scaffold configurations, even though the goal was to investigate the effects of general characteristics of scaffold surfaces and not to simulate specific brands of scaffolds. Cases A-C were inspired by poly (propylene fumarate) (PPF) scaffolds with regularly designed pore structures[23], and cases E and F were inspired by poly-L-lactate-epsilon-caprolactone (PLC) scaffold structures[104]. Case D is a well-constructed fiber web structure that was numerically reconstructed in order to explore our hypotheses. In experiments, some scaffolds do not have beams in contact to support their internal structure, but the fibers supported by an outer "cylindrical shell" structure preventing the geometry from collapsing (see, for example Figure 4, in Yang et al.[104]). Thus, in our simulations for cases D-F the contribution of the outer "cylindrical shell" structure to the overall stress distribution is not calculated, but note that a common scaffold size is about 1cm in diameter and our unit cell is about 100μm, which is 100 times smaller.

This leads to the conclusion that findings from a periodic structure are most valuable, although we do not take the cylindrical shell into account, since the seeded cells should be attached to the interface of the interior of the porous scaffolds.

The scheme suggested by Porter et al.[80] was employed to calculate the flow-induced stress everywhere in the pore space. Specifically, the stress tensor was estimated as follows:

$$\underline{\underline{\tau}} = \frac{1}{2}\mu(\nabla\underline{U} + \nabla\underline{U}^T) \tag{IV.3}$$

The largest eigenvalue of this symmetric matrix was considered to be the value of the flow-induced stress. The analysis focused only on the fluid-solid interfaces, so the stresses calculated by Equation (IV.3) at surface nodes were included in the calculation of the wall stress PDF. The stresses were also normalized by Equation (IV.2) and the obtained dimensionless stresses were then distributed into 50 equally-sized bins, ranging from the smallest to the largest normalized stress value. The wall stress PDFs were calculated by dividing the fractional occurrence of stresses in a particular bin by the width of that bin. A Kolmogorov − Smirnov (KS) goodness of fit test was used to examine whether the stress PDFs followed the gamma-3P distribution.

IV.3 Results and discussion

IV.3.1   Stress distribution at different scaffold geometries

The PDFs of the dimensionless wall stresses obtained from the six porous media configurations from Table IV.1 are shown in Figure IV.2.
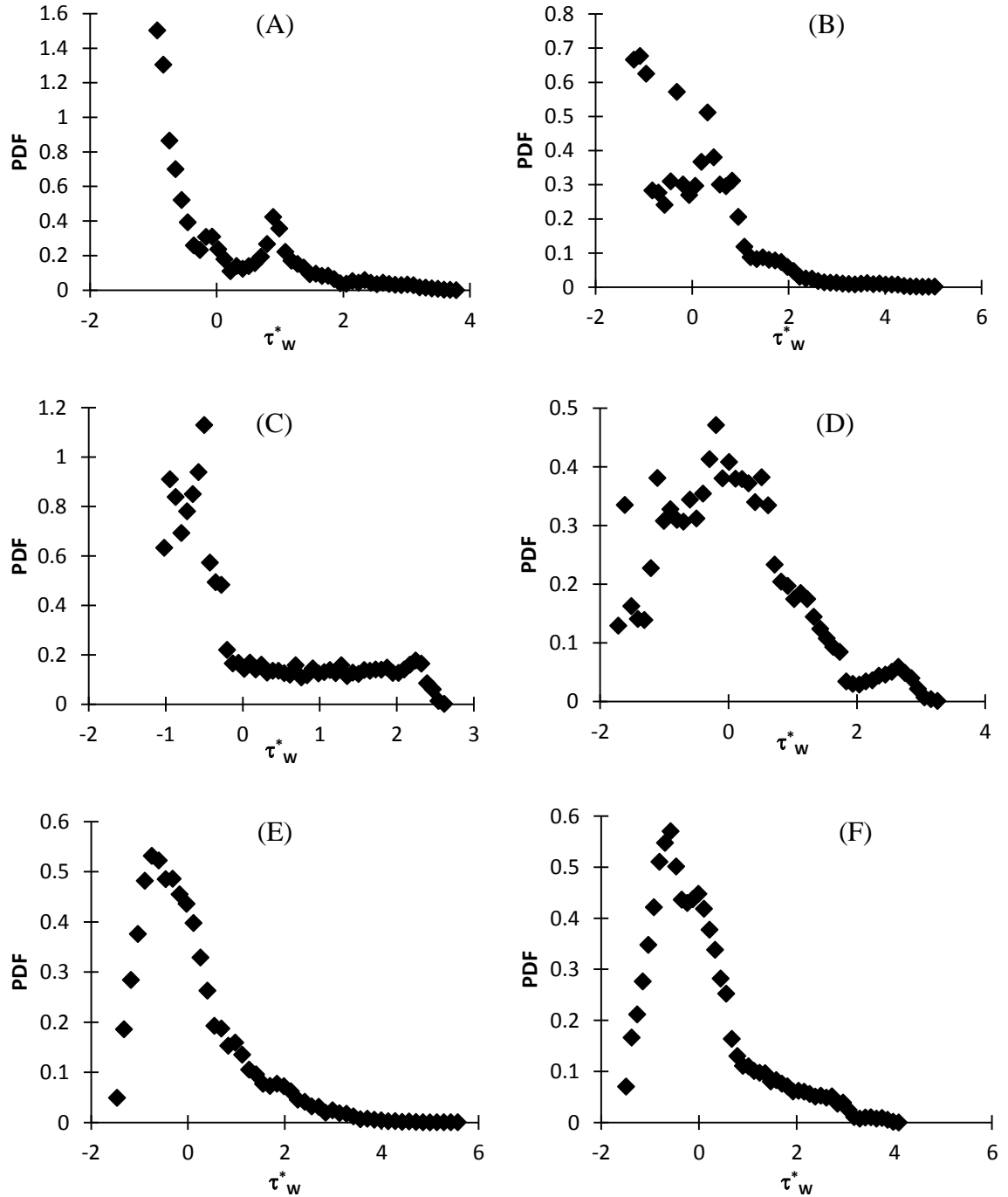
Figure IV.2. PDFs followed by the non-dimensional flow-induced stress obtained from the six geometries examined in this study, Cases A to F.

The stress distribution in Case A has positive skewness and is bimodal. The two local peaks appear, as expected, because the fluid flows around two types of solid surfaces, based on the geometry of the scaffold. The drag for an immersed body of square cross

section is smaller when it is aligned parallel to the flow direction than when it is aligned vertically relative to the flow direction[81]. As seen on Figure IV.2 for Case A, this leads to one peak value for the shear stress corresponding to the fluid flowing around the structural elements (the bars) of the scaffold that are parallel to the flow, and a second peak, at higher stress values, corresponding to the flow around the bars that are perpendicular to the flow direction. It becomes apparent from Figure IV.2 that when structure elements of the scaffold are aligned with the flow direction, there is going to be a corresponding stress peak. Based on the above observation we generated Case B, where the flow direction was at an angle relative to the internal structure of the scaffold. In Case B, the scaffold is not aligned with the flow direction, which is a situation that can be controlled in a flow perfusion bioreactor by rotating the scaffold. In this case, the PDF also displays discrete high frequency modes, but the two peaks are closer together, when compared to Case A. The distribution of the angle of impingement of the fluid on the surface of the scaffold is different than Case A. Further consideration of Figure IV.2 indicates that the range of angles of impingement of the fluid on the internal surface of the scaffold affects the stress distribution, and scaffolds that are constructed so that they can ensure a wide range of flow impingement angles might be the ones that can be described by a common stress distribution.

If the above observation were true, then cylindrical scaffold elements rather than bars would result in an even wider range of angles of impingement than case B due to the curvature of the cylindrical surface. That is why scaffolds with cylindrical structural elements were tried next. It can be noticed from the results for cases C–F that the stress distribution changes when the cross section of the scaffold elements is circular. For

example, in Case C (see Figure IV.2) there seems to be no evidence of a peak at high

stresses, and the shape of the PDF approaches that of a gamma-3P distribution.

However, the obtained PDF indicates a high frequency of low stresses. These stresses

occur close to the intersections of the scaffold branches, where the velocity is low (see

Figure IV.4). Case D has no branch intersections in its configuration, and the PDF of

flow-induced wall stresses approximately matches the gamma-3P distribution. A KS

goodness of fit test shows that the null hypothesis: "the actual PDF follows Γ(2.91, -

1.43, 0.45)" cannot be rejected even at the 20% significance level, indicating that there

is no statistically significant difference between the obtained PDF and the VVSP

gamma-3P distribution. Likewise, a very good agreement was found in Cases E and F,

which exhibit an ordered internal architecture. The internal scaffold architecture in these

two cases looks similar to fiber mesh scaffolds that have been used in perfusion

bioreactors[105].

Figure IV.3 is a comparison of PDFs obtained from Cases E and F to the

gamma-3P distribution. The PDFs obtained from Cases E and F fit the analytical

distribution, although some difference in the peaks is apparent. Again, no statistically

significant difference between the actual distribution and the distribution Γ(2.91, -1.43,

0.45) was found when the KS test was carried out (the null hypothesis cannot be

rejected at the 20% level). Table IV.2 is a summary of the KS test results.

From Table IV.2 it is apparent that reasonable agreement between the observed

stress PDF and the gamma-3P is obtained for all cases, except for Cases A and B, where

the beam cross-section is square. Furthermore, among the different cases it becomes

obvious that the geometries with scaffold elements oriented parallel or perpendicular to

the direction of flow (Cases A-D) result in a poorer agreement with the analytical distribution.
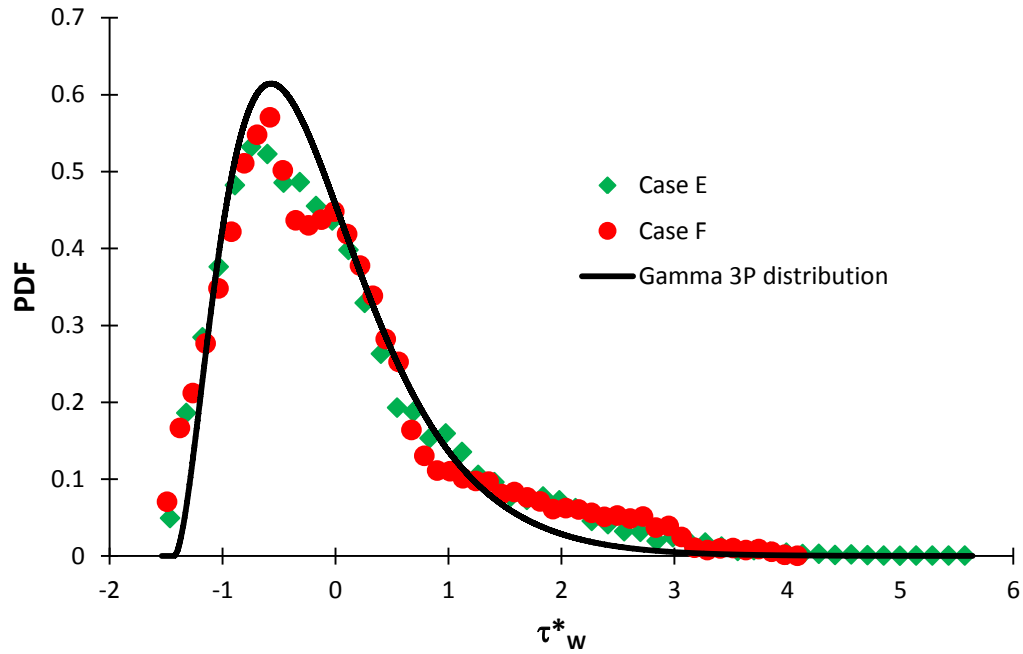
Figure IV.3. Non-dimensionalized stress distributions computed from Case E and Case F and compared to the gamma-3P distribution Γ(2.91, -1.43, 0.45) suggested by VVSP.

Table IV.2. Level of significance from Kolgomorov – Smirnov goodness of fit test at which the null hypothesis cannot be rejected. Dimensional stress was only calculated for Cases E and F.

Cases	Level of significance	
	Normalized stress	**Dimensional stress**
A	< 0.05	-
B	< 0.01	-
C	> 0.2	-
D	> 0.2	-
E	> 0.2	-
F	> 0.2	-
Prediction of Case E	-	> 0.2
Prediction of Case F	-	> 0.2

To investigate this behavior, PDFs of the angle, ω, of the flow direction relative to the normal vector, $\vec{\mathbf{n}}$, pointing away from the surface of the scaffold elements are constructed. Cases A and E, which exhibit the worst and the best agreement with the VVSP distribution, respectively, are chosen for comparison. Contour plots of wall shear stresses for these two cases are also shown in Figure IV.4.
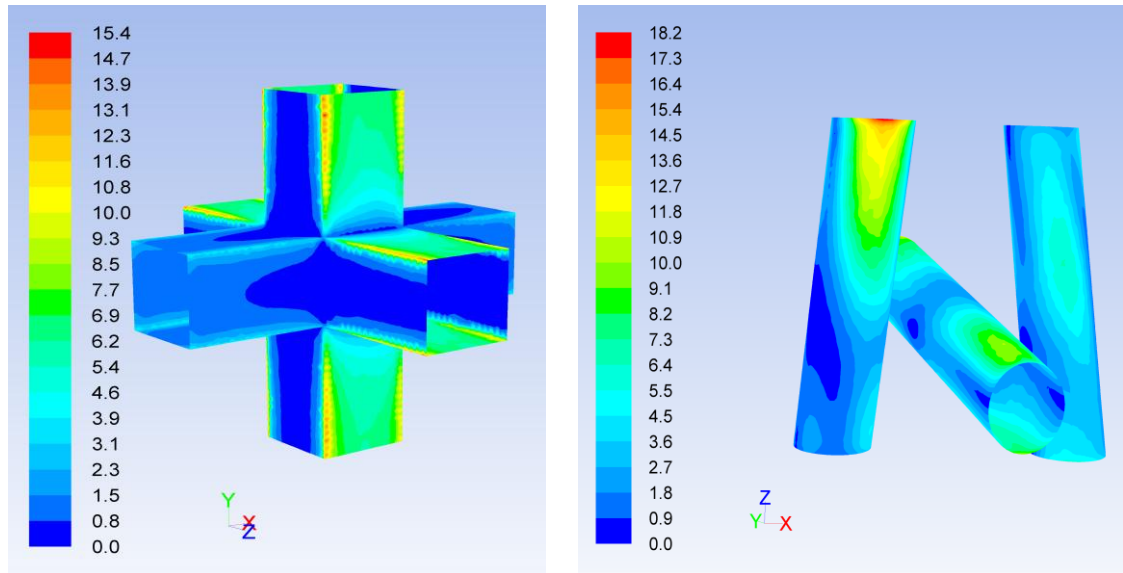
Figure IV.4. Contour plots of the wall shear stress for flow with pressure gradient equal to 100,000Pa/m in Cases A and E.

In Case A, low stresses are mainly distributed on the horizontal branch (i.e., the one parallel to flow direction) while high stresses are seen on the rest of the surface. On the other hand, both low and high stresses can be seen on each one of the cylinders that comprise the internal architecture of the Case E scaffolds. This result agrees with the discussion about drag forces acting on each element of the scaffolds. Its configuration and orientation relative to the flow makes Case A to exhibit only five observed values of ω (0, $\pi/2$, π, $3\pi/2$, and 2π), whereas the PDF of ω in Case E is continuous and

uniform over the range 0 to 2π. One can construct the PDFs of ω of the rest of the cases, which yield discontinuous PDFs for the cases of square cross-section of the scaffold architectural elements. When ω takes values over a wider range, the surface stresses follow a distribution that can be described with the VVSP distribution. In other words, the continuity and uniformity of the PDF of ω can be used to predict whether or not flow-induced stresses in a highly porous scaffold will follow a modal distribution or a distribution that can be described by Equation (IV.1).

IV.3.2   Effects of porosity on the stress distribution

The question of the effects of porosity on the stress distribution is addressed next. This is important, since the porosity of cell-seeded scaffolds that are cultured for a long time will change as cell layers and tissue are generated due to cell proliferation and extracellular matrix deposition, and the space open to fluid flow will decrease. In our case, the porosity of constructed scaffolds was varied by assuming that cell layers will uniformly cover the scaffold surface: the diameter of each beam in the scaffold was decreased (or increased) by the same amount, and the axis of the beam was fixed. Our assumption of uniformly covered scaffold surfaces by cell layers is justified in some aspects with the SEM images shown in Raimondi et al.'s work[102] (Figures 5b and 5d) . This assumption has also been used by Lesman et al.[86], when they modeled cell layers as layers added to all pore walls of the scaffold. Figure IV.5 is a demonstration of how a change in porosity impacts the normalized stress distribution for Cases D and E. Both present the same tendency: the extent of agreement with the VVSP distribution diminishes when the scaffold porosity decreases. The KS test is again employed with null hypothesis: "the actual PDF follows the VVSP distribution". Based on the KS

goodness of fit results, it is found that a critical porosity for the VVSP distribution exists in Case D, and it is between 60% and 70%, because the null hypothesis can be rejected at the 20% significance level when the porosity is 60% (see Table IV.3 for details).
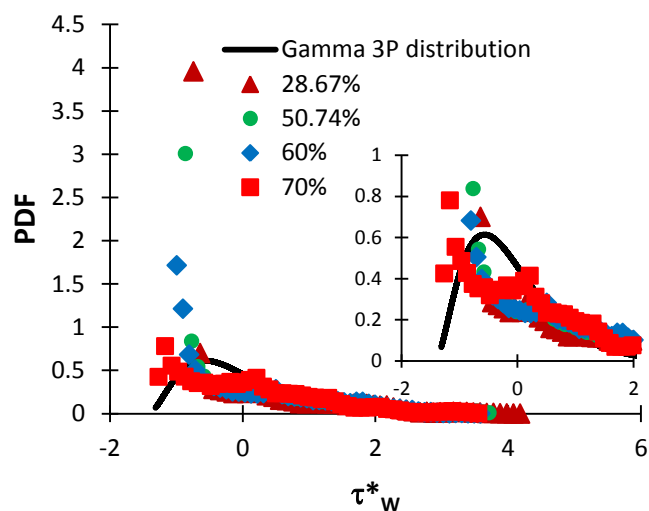
(D)
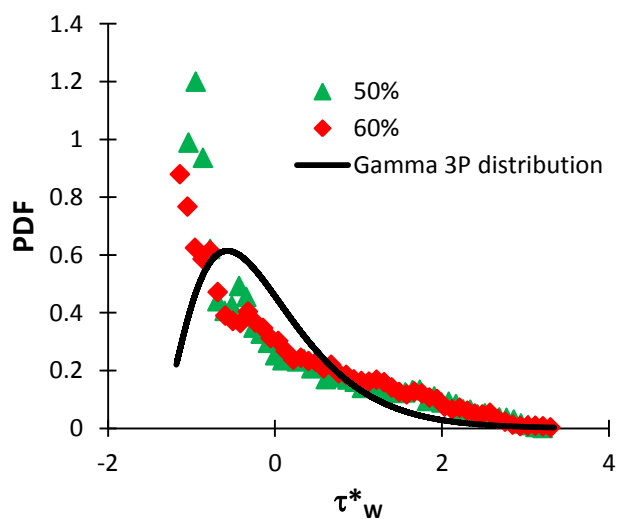
(E)

Figure IV.5. PDFs of normalized flow-induced stress obtained from Case D (top panel) and Case F (bottom panel) at different scaffold porosity. The solid line denoted as "gamma 3P distribution" is the VVSP distribution and the data points correspond to CFD calculations at different scaffold porosity values. The insert figure in the top panel is a close-up of the PDF for case D close to the peak of the distribution.

Table IV.3. Level of significance from Kolgomorov – Smirnov goodness of fit test at which the null hypothesis cannot be rejected at different porosities of Case D and Case E.

Porosity (%)	Level of significance	
	Case D	**Case E**
28.67	<0.02	-
50	-	>0.2
50.74	<0.2	-
60	<0.2	>0.2
70	>0.2	-

Interestingly, in Case E, in which the PDF of ω is continuous and uniform, the VVSP distribution can be acceptable at lower porosity (50%), and obviously the critical porosity for this case is below 50%. This finding implies that one could not only predict, but also control the stresses during the culture process, by manufacturing scaffolds of specific geometric characteristics.

IV.3.3   Use of normalized stresses to obtain dimensional stresses

When the normalized flow-induced wall stress distribution follows a known gamma-3P analytical form, then the dimensional stresses also follow a gamma distribution that can be obtained from the knowledge of only the mean stress (since the standard deviation of the distribution was found in VVSP to be a function of the the mean stress, $\sigma_\tau = 0.7\,\bar{\tau}_W$.) In order to illustrate this concept for the geometries examined in this study, the methodology reported in VVSP is followed. Namely, the $\Gamma(2.91, 0, 0.315\,\bar{\tau}_W)$ distribution, which is the PDF that τ_w follows when the dimensionless stress is given by Equation (IV.2), was used in order to calculate the dimensional stress for

Cases E and F. The only unknown variable is the average stress $\bar{\tau}_W$, which can be calculated by the Wang – Tarbell[106] equation as follows:

$$\bar{\tau}_W = \frac{B\mu}{\sqrt{k}} U_S \qquad\qquad\qquad (IV.4)$$

where B is a constant that accounts for the geometric characteristics of the medium. The value of B for the case of flow around an array of spheres and around a square array of cylinders has been found to be $3/\pi$ and $4/\pi$, respectively. In VVSP, the correlation of $\bar{\tau}_W$ to U_S resulted in a straight line and the value of B ≈ 1 was suggested. The permeability can be calculated with either measurements (as was done in our simulations) or by a semi-empirical equation like the Blake-Kozeny-Carman equation that can provide permeability for porous media and laminar flows. Figure IV.6 is a comparison between the prediction and the actual PDF that the dimensional stress follows for Cases E and F. It is apparent from Figure IV.6 that there is a good agreement between the two. The KS test also showed that there is no statistical difference between them, even at the 20% significance level.
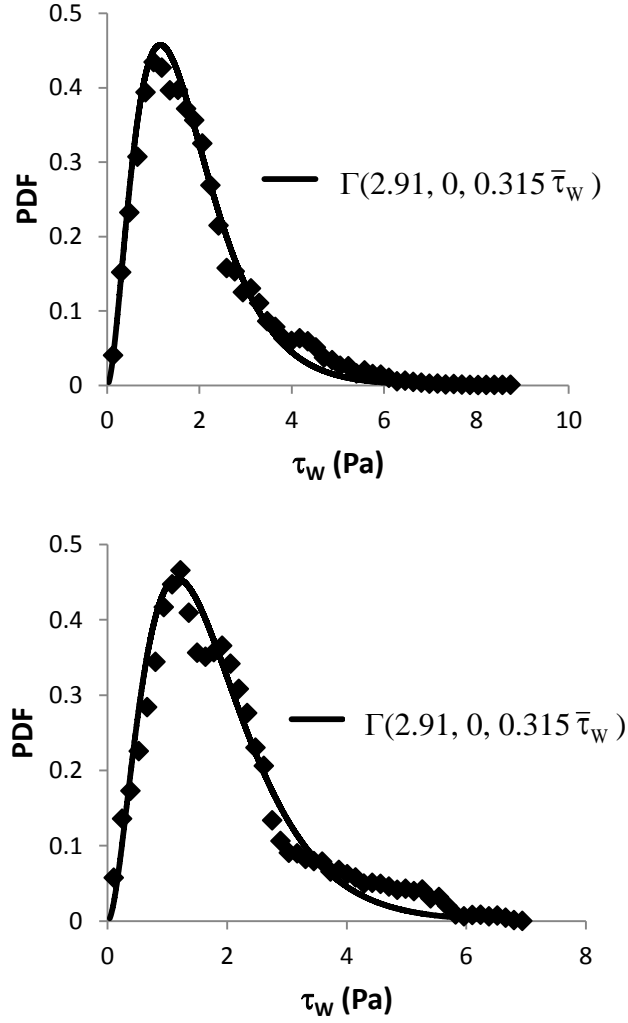
Figure IV.6. Comparison of PDFs of dimensional stress obtained in Case E (top panel) and Case F (bottom panel) to predicted PDF obtained by the methodology suggested in VVSP. The permeability of the Wang-Tarbell equation was calculaled from the simulations and the value B = 1 was used. The diamond-shaped points are the CFD results.

Finally, the determination of a preferential geometry for stimulating cell proliferation and reducing cell detachment is implicitly addressed by our findings. Having an analytical expression, like Equation (IV.1), which can be used to obtain a-priori characteristic values of the stress distribution can be helpful in choosing a scaffold geometry. For example, the most frequent value of the distribution (i.e., the mode value of the variable rather than the average) for a gamma distribution is given as $(\bar{\alpha} - 1)\beta$,

and in the case of the suggested distribution this is about $0.6\,\bar{\tau}_w$. Our suggestion would

be to use a scaffold geometry that produces a stress distribution that is predictable, and

then tune the flow rates to result in the most frequent stresses to be in the range that is

desirable, as already described in the Introduction[87, 88].

CHAPTER V.   BULK STRESS DISTRIBUTION IN PACKED BEDS

V.1   Introduction[‡]

Motion of colloidal particles, microparticles and NPs through porous media has been found to be important in many engineering disciplines such as tissue engineering, environmental engineering, and petroleum engineering. In tissue engineering, deposition of biocolloids (cells) on the surface of a porous scaffold and cell proliferation is a desired process. This process is strongly affected by the flow-induced stresses that can either enhance the attachment of the suspended particles to the pore surfaces or wash attached particles away from the surfaces[89, 107-109]. In environmental applications, NPs released to the subsurface during the disposal of nanomaterials might penetrate the soil and contaminate the water table and aquifers. Several types of NPs have been reported to be toxic to many animal species and humans[110-116]. In petroleum engineering, the evolution of nanomaterials has opened up an opportunity for developing nanosensors that can be helpful in enhanced oil recovery (EOR)[117-120]. Those NPs should be specifically fabricated so that they can propagate through the reservoir rock. By measuring their responses to external signals, detailed information about the reservoir can be obtained[117-120]. In addition, surfactant-based EOR depends on the stability of colloidal particles propagating through a hydrocarbon reservoir[121], while the self-assembly of surfactants into micelles is strongly sensitive to flow-induced shear stresses[122, 123].

The stability and mobility of micro and NPs in the above scenarios depend on flow-induced stresses. These stresses can cause aggregation of NPs/micelles and, in turn, result in sedimentation or size exclusion of large particles, while moving through the pores[122, 124-128]. These are unwanted phenomena in applications where suspension stability, mobility, and long travel distance of NPs are crucial prerequisites (e.g., EOR). It is therefore important to either predict or measure the stress distribution in the flow field occurring in a porous material when releasing particles into that field. Unfortunately, knowing how stresses distribute from experimental measurements is a cumbersome task[129]. On the other hand, simulation results have been recently obtained that present the distribution of flow-induced stresses on the fluid-solid interface in the pore space of media with different geometric configurations, ranging from fiber-webs to packed-beds[43, 82, 86, 130-135]. Based on such results, a common 3P gamma distribution describing normalized surface stress distributions has been proposed[43]. While a lot of attention has focused on surface stresses, neither simulation models nor mathematic models address how bulk stresses distribute in the open pore spaces of the geometry. This is critical, because particles in stable suspensions might not settle on the solid surfaces, but instead they might be anywhere in the geometry. As stated earlier, this is especially important for those processes that require particles of high mobility that do not deposit and do not aggregate.

In this work, normalized stress distributions inside the open spaces (in the bulk of the fluid) of ideally packed beds with spherical beads [*i.e.,* face centered cubic (fcc), body centered cubic (bcc), simple cubic (sc), and random packing], consolidated Berea sandstone, and structured fiber-web geometries were numerically investigated. The

contributions of this work are to (a) examine whether the stress distributions can be described by a common form of a PDF; (b) explore the physical reason behind the observation of a common PDF, if it exists; and (c) determine how the stresses within the open space of porous media can be theoretically predicted.

V.2 Simulation setup

Stress distributions in the open spaces of ideally packed spheres (sc, bcc, and fcc) and randomly packed spheres were mainly investigated. Among these, the random sphere packing was created by using event-driven molecular dynamics and a modified Lubachevsky-Stillinger algorithm[136]. Packed spheres were rigid, impermeable, and 1mm in diameter. To simulate an infinite array of spheres, periodic boundary conditions were applied in the three space directions X, Y, and Z. In addition, other porous media configurations that may be found to describe synthetic scaffold geometries that are structured were generated. In biomedical applications, like tissue engineering, porous scaffolds serve as three dimensional structures on which seeded stem cells can attach, proliferate, and finally form 3D extracellular matrix producing functional tissue for transplantation. It has been found that all of these processes are promoted by flow-induced stresses, so flow perfusion bioreactors are often used for the dynamic culturing of the cell-seeded scaffolds[27, 84-87]. These cases were analyzed using commercial, finite volume-based CFD software[23, 104, 137].

Furthermore, the stress distribution within the pore space of a consolidated reservoir rock, in this case Berea sandstone, was also computed with LBM. The digital three dimensional (3D) geometry of the Berea rock sample was reconstruced from micro-computed tomography (μCT) images obtained by an Xradia MicroXCT 400

machine. Over nine hundred grayscale images, each representing a slice of the rock, were taken with a resolution of 4.5μm. These images were then converted into binary images with only two intensities, 0 and 1, containing information of either empty nodes or solid nodes, and reattached to form virtual 3D geometry by a custom-written code in Matlab®. A thin slab of the virtual 3D geometry was used as the representative elementary volume of the porous medium.

Details of the geometry characteristics and the flow conditions of all studied cases are summarized in Table V.1. An incompressible and Newtonian fluid with a viscosity of 0.001Pa.s, which is equivalent to that of water, was employed as the working fluid. Three different pressure drop values of 10, 100, and 1000Pa/m were applied for all the sphere packing cases. A pressure drop of 100,000Pa/m was used for flow in the six porous scaffolds and a pressure drop of 10,000Pa/m was used for flow in the Berea sandstone.

Table V.1. Geometric characteristic of examined porous media

Geometry	Domain size [μm^3]	Porosity [%]	Permeability [m^2]	Size of structural element* [μm]
fcc spheres	1414.2^3	25.95	1.848×10^{-10}	1000
bcc spheres	1143.3^3	31.98	5.226×10^{-10}	1000
Randomly packed spheres	2000^3	39.76	1.116×10^{-9}	1000
sc spheres	1000^3	47.64	2.841×10^{-9}	1000
Case (a)	143.2^3	85	3.701×10^{-10}	35
Case (b)	202.5^2×143.2	85	3.606×10^{-10}	35
Case (c)	127^3	85	3.174×10^{-10}	35
Case (d)	113.26^3	85	2.315×10^{-10}	35
Case (e)	141.14^3	85	3.608×10^{-10}	35
Case (f)	162.97^3	85	3.848×10^{-10}	35
Berea slab	900^2×1800	20.08	2.428×10^{-12}	-

The structural element is the sphere diameter in sphere packing cases, the cylinder diameter in Cases (c)-(f), and the edge of the bar cross section in Cases (a)-(b).

The flow-induced stress tensor $\underline{\underline{\tau}}$ was calculated from the rate of strain as stated in Equation (IV.3). The largest eigenvalue of this tensor was then considered to be the most important flow-induced stress, as previously done in Porter et al.[80] and in prior work in our laboratory[43]. The calculation of the PDF of the fluid stresses in the open spaces excluded the surface stresses on the fluid-solid interfaces. The stresses obtained from Equation (IV.3) were then normalized by subtracting the mean stress, $\bar{\tau}$, and dividing by the standard deviation of the stress distribution, as follows:

$$\tau^* = \frac{\left(\tau - \bar{\tau}\right)}{\sigma_\tau} \tag{V.1}$$

Note that this dimensionless variable is defined similarly to the random variable of the standard normal distribution (in that case the variable has a mean of zero and a standard

deviation equal to one). It is justified to use this normalization here, since we want to obtain a general form of the stresses that can be applicable in different porous media geometries, rather than a case-specific distribution. The obtained dimensionless stresses were then partitioned into 100 bins of equal width, and the stress PDF was calculated by dividing the fractional occurrence of normalized stresses in a particular bin by the width of that bin. A Kolgomorov – Smirnov (KS) goodness of fit test, conducted using the software Easyfit version 5.4 (http://www.mathwave.com), was used to examine whether the stress PDF followed a known form of PDF.

V.3   Results and discussion

V.3.1   Distributions of dimensional and normalized stresses in columns packed with spheres

In Figure V.1 we plot four different geometries of sphere packings with contours of the associated stresses in the pore space.
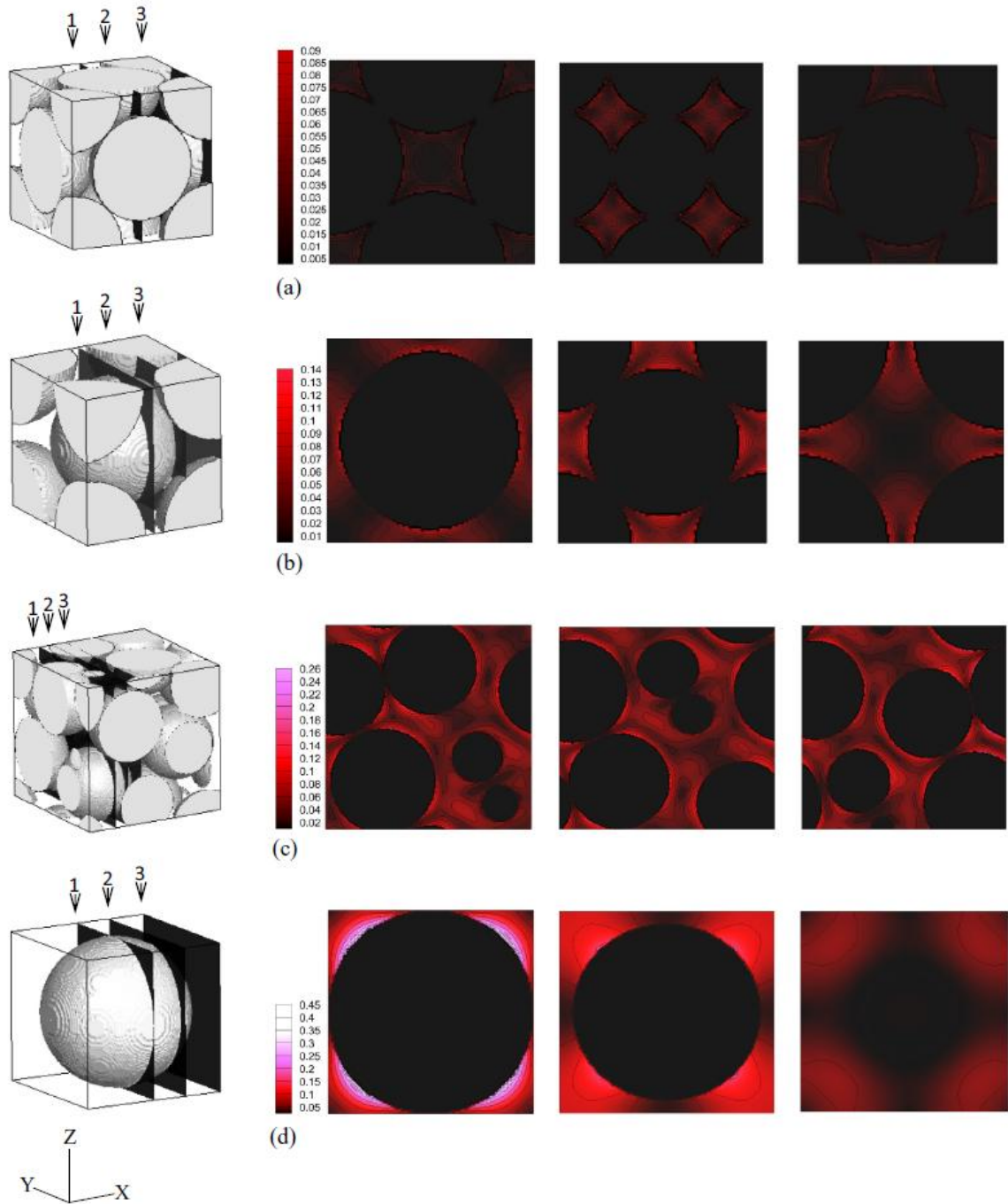
Figure V.1. Contour of stresses in the open spaces of studied sphere packing geometries. Stresses at three different positions, marked by 1, 2, and 3 are showed in slices from left to right. The color scaled bar unit is of $g/cm^2.s^2$. This is the case when a pressure drop of 100Pa/m is employed. (a) is fcc packing, (b) is bcc packing, (c) is random packing, and (d) is sc packing sphere.

In each case, the contours of the pore stresses in three different planes that are

perpendicular to the flow direction are shown. It can be seen from the color maps in

Figure V.1 that stresses in the low range are dominant. In fcc and randomly packed spheres, it seems like there are large areas with low stresses and small areas of high stresses. On the other hand, in bcc and sc sphere packing cases, the low stresses and the high stresses cover almost equal areas.

Figure V.2 is a presentation of the stress distributions in dimensionless form of the four sphere packing types at three different pressure drops in the Darcy flow regime.
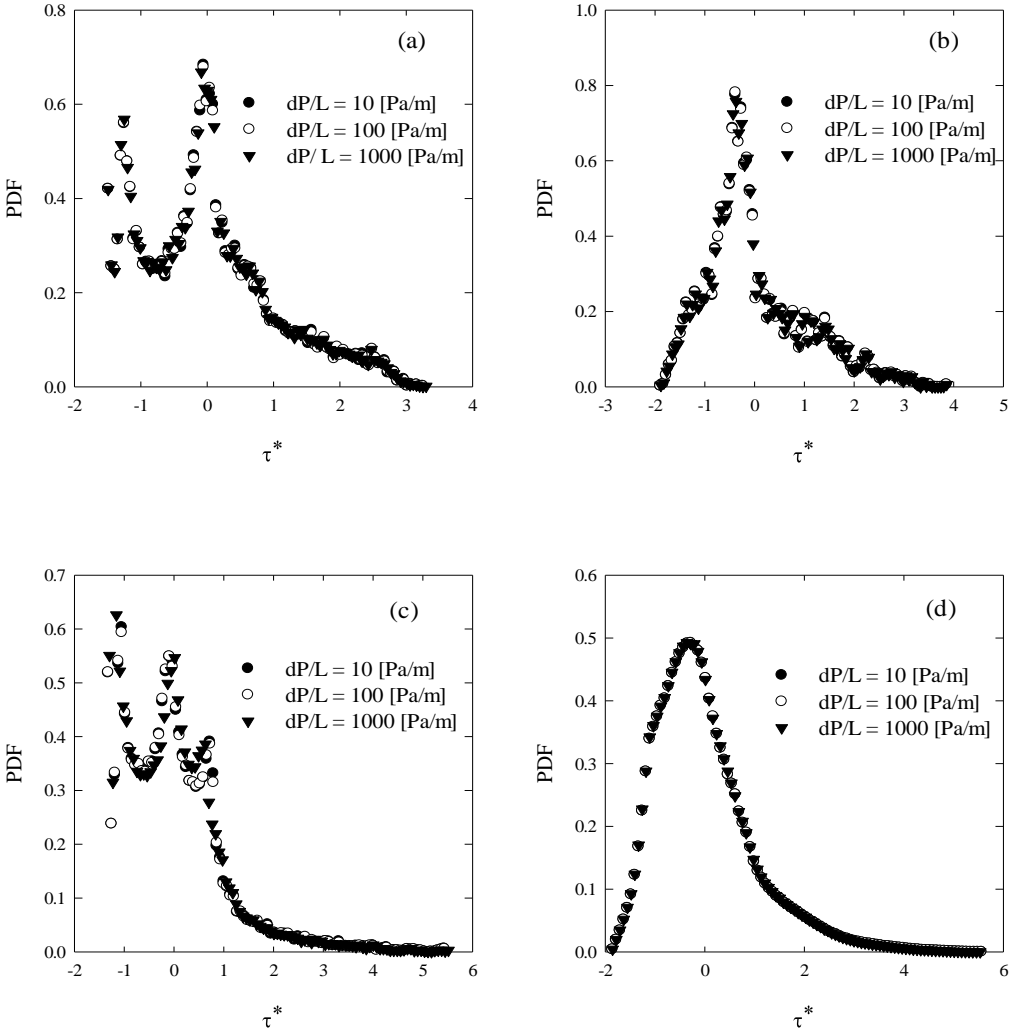
Figure V.2. Normalized stress distributions of four tested sphere packing types at three different pressure drop values. (a) is bcc, (b) is fcc, (c) is sc, and (d) is random packing sphere. Under Darcy flow conditions, the pattern of the distribution in particular sphere geometry is unchanged.

The stress data were normalized by utilizing Equation (V.1). A common feature in all the distributions observed in Figure V.2 is the positive skewness, i.e., the tail of the PDF to the right is longer. It is also seen that the normalized stress distribution corresponding to each particular configuration of packed spheres is characteristic to that specific configuration, i.e., the fcc packing and the random packing result in distributions with a single mode, whereas those of the bcc packing and the sc packing are bimodal and trimodal, respectively. Knowing this distribution is critical to quantitatively predict the probability of finding a certain range of stresses in the flow field. When the dimensional mean stress and the standard deviation of the stress PDF are known, then obtaining a dimensional stress distribution from a normalized one is straightforward. The difference in the number of modes might be attributed to the nonuniformity of the pore sizes, in the sense that a continuous pore size distribution without modes leads to a bulk stress distribution with a single mode (see Figure A.3 in the Appendix A.3 for the pore size distributions of the four sphere packing types). By that logic, the multiple modes of the bcc and sc sphere packing are expected, because the pore size distribution in these cases is multimodal and can be represented with capillary tubes with distinct but almost uniform diameters. Although the shape of these distributions differs from packing to packing, there is no change in their shape when a particular type of packing undergoes different pressure drops, because of the linear dependence between the pressure drop and the stresses in the Darcy flow regime[135]. Voronov et al.[47], based on a numerical investigation of flow of an incompressible Newtonian fluid through salt-leached porous scaffolds, have proposed the following empirical correlation for the average stress in the open pore space:

$$\bar{\tau} = (0.0851 \pm 0.0064)\left(\frac{\Delta P}{L}\right)^{0.503 \pm 0.015} U_S^{0.497 \pm 0.015} \tag{V.2}$$

where $\Delta P/L$ is the pressure drop. In flow following Darcy's law, $\Delta P/L$ is proportional to the superficial fluid velocity, U_S. Equation (V.2) then leads to a linear relation between $\bar{\tau}$ and $\Delta P/L$, which is consistent with expectations, for example with the Wang & Tarbell equation for flow around spheres and cylinders[106, 138]. Note also that the constant involved in the expression is proportional to $\sqrt{\mu}$.

Another important consideration is to find a common PDF model that can fit the normalized distributions within statistically acceptable accuracy. Such common PDF models, describing different physical phenomena ranging from the distribution of rain droplet sizes to the distribution of friction coefficients (among others), have been obtained in other cases[139-141]. In order to reveal a common PDF, normalized stress data presented in Figure V.2 were tested with 65 different common PDF models, available in the Easyfit software, version 5.4 (http://www.mathwave.com). The goodness of fit test between the PDF models and our data was conducted using the Kolmogorov-Smirnov (KS) test. The null hypothesis was: "the normalized stress PDF follows the tested PDF model". The level of significance, α, was chosen to be 0.2. By choosing $a = 0.2$, the acceptance of the null hypothesis is more rigorous than acceptance at the usual choice of $a = 0.05$. Note that, in the KS test, the critical value of the KS statistic decreases when α increases, and that the null hypothesis is rejected when the critical value is smaller than that of the test statistic of a data sample. Thus, at a given value of the calculated test statistic, testing for the null hypothesis at a higher α increases the probability of rejecting the null hypothesis. Such a high level of α has been used for

testing null hypotheses in other published works[43, 142, 143]. Table V.2 is a summary of
PDF models that best describe the actual dimensional and normalized PDF data along
with the KS statistic, the corresponding p-values and the level of significance for
rejecting a true null hypothesis.

Table V.2. Results from the Kolgomorov – Smirnov goodness of fit test for 8 among 65 PDF
models. Values obtained from one pressure drop ($\Delta P/L = 10Pa/m$) are presented, as statistics of
other cases do not change significantly, because of the linearity between stress and pressure
drop in the examined range. The p-values are also shown in parentheses. Note that the values of
the critical Kolmogorov-Smirnov statistic for $\alpha = 0.05$ and $\alpha = 0.2$ are 0.1340 and 0.1056,
respectively. We accept the null hypothesis when the KS statistic is smaller than the critical
value for the respective level of significance.

PDF model	Kolmogorov-Smirnov statistic value (p-value)							
	Normalized stress				**Dimensional stress**			
	bcc	fcc	sc	Random	bcc	fcc	sc	Random
4P-Burr	0.0792	0.0752	0.0748	0.0218	0.0696	0.0764	0.2444	0.0739
	(0.53)	*(0.59)*	*(0.60)*	*(1.0)*	*(0.70)*	*(0.58)*	*(9.7×10^{-6})*	*(0.62)*
3P-Fatigue life	0.0755	0.0736	0.0753	0.0273	0.0754	0.1208	0.0753	0.0273
	(0.59)	*(0.62)*	*(0.59)*	*(1.0)*	*(0.59)*	*(0.099)*	*(0.59)*	*(1.0)*
3P-Gamma	0.0909	0.0781	0.0839	0.0331	0.0909	0.0782	0.0838	0.0332
	(0.36)	*(0.55)*	*(0.46)*	*(1.0)*	*(0.36)*	*(0.55)*	*(0.46)*	*(1.0)*
3P-Inverse Gaussian	0.0734	0.0733	0.0731	0.0273	0.2161	0.1204	0.0727	0.0889
	(0.63)	*(0.63)*	*(0.63)*	*(1.0)*	*(1.4×10^{-4})*	*(0.101)*	*(0.64)*	*(0.38)*
3P-Log-logistic	0.0659	0.0583	0.0667	0.0297	0.0659	0.0585	0.0667	0.0298
	(0.75)	*(0.86)*	*(0.74)*	*(1.0)*	*(0.75)*	*(0.86)*	*(0.74)*	*(1.0)*
3P-Lognormal	0.0693	0.0719	0.0703	0.0268	0.0693	0.0721	0.0703	0.0269
	(0.70)	*(0.65)*	*(0.68)*	*(1.0)*	*(0.69)*	*(0.65)*	*(0.68)*	*(1.0)*
3P-Pearson type 5	0.0642	0.0705	0.0648	0.0261	0.2087	0.1504	0.1703	0.1148
	(0.78)	*(0.67)*	*(0.77)*	*(1.0)*	*(2.7×10^{-4})*	*(0.019)*	*(5.2×10^{-3})*	*(0.13)*
4P-Pearson type 6	0.0726	0.0710	0.0762	0.0266	0.0852	0.0764	0.0745	0.2818
	(0.64)	*(0.67)*	*(0.58)*	*(1.0)*	*(0.44)*	*(0.58)*	*(0.61)*	*(1.7×10^{-7})*

The KS test results in Table V.2 indicate that 8 listed PDF models can predict the
normalized stress distributions of packed beds with spheres within the prescribed

statistical accuracy. Among those listed, the three-parameter gamma (3P-gamma) , the three-parameter log-logistic (3P-log-logistic), and the three-parameter lognormal (3P-lognormal) were found to be also valid for all the dimensional distributions shown in which a true null hypothesis cannot be rejected at $\alpha = 0.2$. The p-value for the case of randomly packed spheres is one for these cases.

V.3.2 Relation between the pore size and space stress distribution, and prediction of the common PDF

At this point one may inquire which one among the three models is the most appropriate to use. One way to answer this question is to explicitly show how the stresses distribute in the pore space through the use of analytical results. The governing equations for creeping flow over an array of spheres are usually obtained in integral form from a transformation of the Navier-Stokes equation[131, 144]. Unfortunately, solving these equations is not simple. Instead we draw a connection between the pore size distribution and the stress distribution by utilizing a simplified model of the pore network as a bundle of capillary tubes[145-147]. In brief, we assume that the pore network of an array of spheres can be represented by a bundle of circular straight capillary tubes with different diameters. This simplification has been found to be valuable in studies of flow behavior in unconsolidated porous media[148, 149]. Since the pore network is regarded as an ensemble of circular capillary tubes, the stress profile in any one individual tube is found as follows[150]:

$$\tau = \frac{\Delta P}{L} \frac{r}{2} \qquad (V.3)$$

Statistically, if the PDF of r is known, then knowing the PDF of the dependent variable τ can be calculated from the PDF of r, the inverse function of Equation (V.3) and its

74

derivative[151]. According to published reports[152-154], the pore size distribution of soil and some types of ultra-filtration membranes follows the log-normal law. In other words, the pore radius is log-normally distributed and is formulated as

$$f(r) = \frac{\exp\left[-\frac{1}{2}\left(\frac{\ln r - \zeta'}{\chi'}\right)^2\right]}{r\chi'\sqrt{2\pi}} \quad (V.4)$$

where f(r) is the PDF of the pore radius, ζ' and χ' are the continuous parameters of the distribution ($\chi' > 0$) [the log-normal is denoted by log-normal(ζ', χ') for convenience]. Applying the transformation method for Equation (V.3), the PDF of the dependent variable, τ, is found as follows [151]:

$$f(\tau) = \frac{\exp\left[-\frac{1}{2}\left(\frac{\ln \tau - \zeta}{\chi}\right)^2\right]}{\tau\chi\sqrt{2\pi}} \quad (V.5)$$

where $\chi = \chi'$ and $\zeta = \zeta' - \ln\left(\frac{2}{\Delta P/L}\right)$. It is obvious from Equation (V.5) that the pattern

of f(τ) is identical to that of f(r) in which χ' is unchanged and $\zeta = \zeta' - \ln\left(\frac{2}{\Delta P/L}\right)$.

Consequently, the average stress, $\bar{\tau}$, and the standard deviation, σ_τ are related to the two continuous parameters of the distribution as[155]

$$\begin{cases} \bar{\tau} = e^{\zeta + \frac{\chi^2}{2}} \\ \sigma_\tau = e^{\zeta + \frac{\chi^2}{2}}\sqrt{e^{\chi^2} - 1} \end{cases} \quad (V.6)$$

The connection between the pore size distribution and the stress distribution in a porous medium where the pore network is represented as a bundle of capillary tubes is strengthened by an extreme case presented in the Appendix A.1.

It is also important to note here that if the PDF of the dimensional stresses is log-normal(ζ, χ), then the PDF of the normalized stresses, τ^*, is 3P log-normal(γ^*, ζ^*, χ) and the PDF can be written as follows:

$$f(\tau^*) = \frac{\exp\left[-\frac{1}{2}\left(\frac{\ln(\tau^*-\gamma^*)-\zeta^*}{\chi}\right)^2\right]}{\chi\sqrt{2\pi}(\tau^*-\gamma^*)} \qquad (V.7)$$

where $\gamma^* = -\dfrac{\bar{\tau}}{\sigma_\tau}$ is the continuous location parameter, $\zeta^* = \zeta - \ln\sigma_\tau$, and χ remains the same as that of $f(\tau)$. Proof of this result can be obtained with a procedure analogous to the transformation of the normal distribution, $N(\overline{X}, \sigma_X^2)$, of a random variable X to the standard normal distribution, N(0, 1), of the random variable $(X - \overline{X})/\sigma_X$ (see Appendix A.2)[156]. The above relation of γ^* to $\bar{\tau}$ and σ_τ implies that one can calculate γ^* from the minimum normalized stress value, since the physical interpretation of the location parameter γ^* is that it represents the minimum value of the random variable (the starting point of the normalized stress distribution). This relation along with Equation (V.6) yields the relationship between γ^* and χ as follows:

$$\gamma^* = -\frac{1}{\sqrt{e^{\chi^2}-1}} \qquad (V.8)$$

Furthermore, the expression $\zeta^* = \zeta - \ln\sigma_\tau$ leads to the relation of ζ^* and χ, as follows:

$$\zeta^* = -\frac{\chi^2}{2} - \ln\sqrt{e^{\chi^2}-1} \qquad (V.9)$$

Therefore, when γ^* is known, the parameters of the log-normal(γ^*, ζ^*, χ) can be predicted. However, it is somewhat difficult to analytically estimate the value of γ^*, since the flow conditions and the pore structure exert strong influences on $\bar{\tau}$ and σ_τ.

76

Our simulation data can be used to obtain the value of γ^* from the minimum normalized stresses, τ^*_{min}, of the normalized stress distributions. It is seen on Figure V.2 that τ^*_{min} for all the packing morphologies is approximately -2, or $\gamma^* = -2$. Subsequently, χ and ζ^* can be calculated from Equations (V.8) and (V.9), leading to the result that the common distribution of the normalized stresses is the log-normal(-2, 0.588, 0.47). The predicted log-normal(-2, 0.588, 0.47) is depicted in Figure V.3 with the normalized stress distributions in the open space of four examined sphere packing geometries. The agreement is apparent with the naked eye without the aid of statistical analysis in the case of fcc and randomly packed spheres.
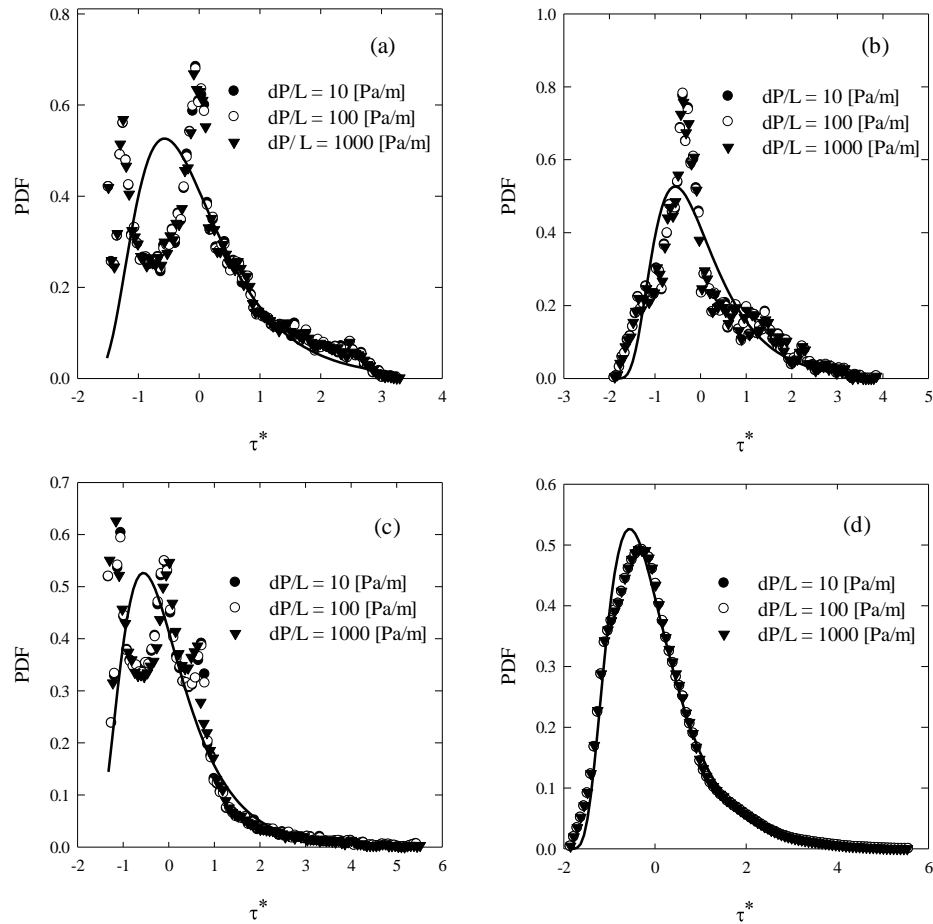
Figure V.3. Normalized stress data in Figure V.2 along with the 3P log-normal distribution (solid line). The goodness of fit was tested using Kolgomorov − Smirnov test at the level of significance $\alpha = 0.2$. (a) is bcc, (b) is fcc, (c) is sc, and (d) is random packing sphere.

V.3.3 Validity of the predicted log-normal PDF in porous scaffold structures

The above considerations suggest that the 3P log-normal(-2, 0.588, 0.47) might be a good approximation for the stress distributions in the open space of packed-sphere beds under Darcy flow conditions. In order to examine whether this finding holds for other cases of porous media, stress distributions in the pore space of highly porous scaffolds were examined next. A finite volume-based numerical method (available in the commercial CFD software Fluent, version 12.0.12), was used as an alternative approach to the LBM for the simulation of the flow. Six different porous scaffold geometries were simulated, such as those that can be fabricated by rapid prototyping or 3D printing techniques. The porosity was chosen to be 85%, in the range often used in scaffolds (see Figure IV.1 in Chapter IV). The physical properties of the fluid were the same as those for the packed bed cases simulated with LBM. The flow was periodic in the X, Y and Z directions. The details of these simulations, the computational mesh size generation, and the stresses on the surface of the solid structure elements of these scaffolds have been discussed in Chapter IV. The fluid stresses in the open pore space for these geometries were also normalized by applying Equation (V.1). The normalized stress distributions of all examined scaffold geometries are illustrated in Figure V.4 along with the 3P log-normal(-2, 0.588, 0.47) distribution.
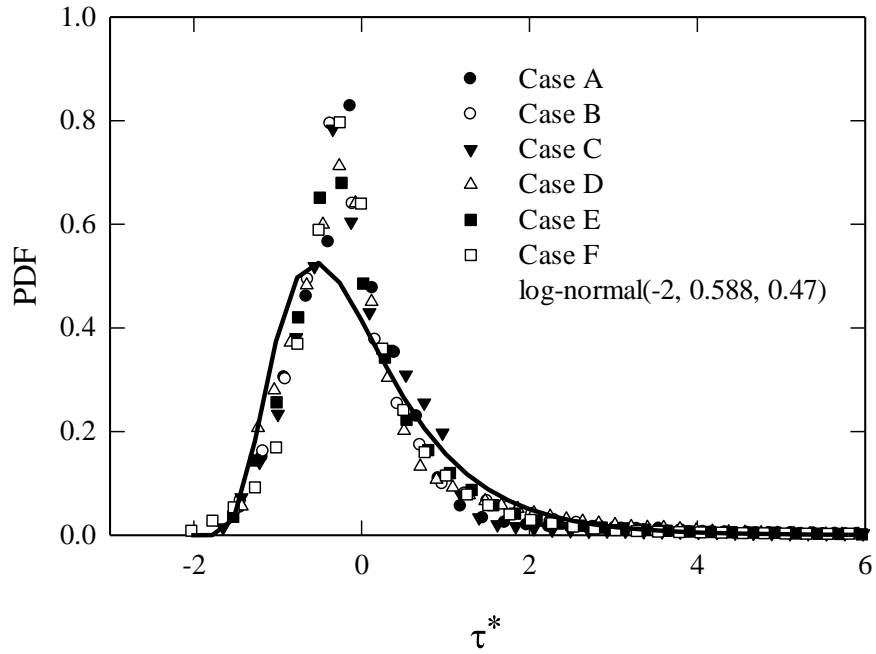
Figure V.4. Normalized stress distributions in the pore spaces of six different porous scaffolds along with the common 3P log-normal distribution.

Despite different geometric morphologies, the normalized stress distributions exhibit similar features, such as positive skewness, the same peak position, and single mode. Within six scaffold geometries, the agreement of the normalized stress distribution of structure A, B, C, D, and E with the 3P log-normal(-2, 0.588, 0.47) law was confirmed by the KS test results, when the null hypothesis cannot be rejected at $\alpha = 0.2$ (p values are 0.21, 0.26, 0.32, 0.66, and 0.35 for structure A, B, C, D, and E, respectively). For the remaining case, the level of significance to accept the null hypothesis is $\alpha = 0.1$ (p value is 0.14).

V.3.4   Validity of the predicted log-normal law in Berea sandstone and obtainment of log-normal law of dimensional bulk stress distributions

When the normalized stress distribution of a certain porous medium follows the log-normal(-2, 0.588, 0.47), it is straightforward to find the log-normal(ζ, χ) of the dimensional stresses as follows (see Equation (V.9) and related comments):

$$\begin{cases} \zeta = 0.588 + \ln\dfrac{\overline{\overline{\tau}}}{2} \\ \chi = 0.47 \end{cases} \qquad \text{(V.10)}$$

So long as $\overline{\tau}$ is unknown, the dimensional stress distribution of the porous medium remains unpredicted. To address this issue, Darcy's law is rearranged to solve for $\Delta P/L$, and then substituted into Equation (V.2) to obtain the following expression (note that the constant in Equation (V.2) is considered to be $B\sqrt{\mu}$):

$$\overline{\tau} = B\frac{\mu}{\sqrt{k}}U_s \qquad \text{(V.11)}$$

It is noted that the form of Equation (V.11) is identical to the Wang & Tarbell equation, in which the average shear stress for flow around a periodic square array of cylinders is estimated[106]. The B value for the porous media considered in this study was found by fitting $\overline{\tau}$, computed from simulation data, to a linear function of $\dfrac{\mu}{\sqrt{k}}U_s$. The slope of the trend line turned out to be 1.41 with a coefficient of determination $R^2 = 0.997$ for beds packed with spheres, and it was found to be 0.526 with $R^2 = 0.9$ for highly porous scaffolds. Thus far, since the correlation for predicting the average stress has been revealed, the dimensional stress distribution of a porous medium, for which the

normalized stress distribution follows the 3P log-normal law suggested above, is

predicted to be log-normal$[0.588 + \ln\left(B\frac{\mu}{2\sqrt{k}} U_s \right), 0.47]$.

Finally, the dimensional stress distribution and the corresponding normalized

stress distribution in the pore spaces of a consolidated Berea sandstone slab were

determined and fit to the log-normal$[0.588 + \ln\left(B\frac{\mu}{2\sqrt{k}} U_s \right), 0.47]$ and log-normal(-2,

0.588, 0.47), respectively. In this case, B = 1.41 was employed. The 3D geometry of the

sandstone was reconstructed from its 2D grayscale images, obtained after scanning the

rock sample by a micro-CT machine (X-Radia, 4.5 μm resolution). A 2D image

analysis was also applied to the pore size distribution. Afterwards, the 3D rock sample

was meshed into 16,000,000 grid points using a structured mesh. The low permeability,

high tortuosity, and randomness of the pore space of the rock are factors that challenge

the validity of the two proposed log-normal laws (see Table V.1 for physical properties

of the examined rock). To obtain the stress distributions, the stress field was computed

using the LBM simulation after forcing water to flow through the rock sample at a

pressure gradient of 10,000Pa/m.

In contrast to the case of sphere-packed beds as well as highly porous scaffolds,

the normalized stress distribution in the pore spaces of the consolidated Berea sandstone

shows a completely different behavior. The values of the PDF of finding a certain range

of stresses dramatically decreases over the whole range of normalized stress, from the

smallest to the largest value, and no peak is recognized. It is more likely that the stress

distribution computed from the simulation of the Berea rock sample follows the

exponential distribution rather than the 3P log-normal distribution (data not shown).

The finding that high PDF frequency values correspond to low stresses in sandstone can be physically interpreted by the existence and dominance of flow regions with velocities that are very slow or even in the negative flow direction. This is expected, since common Berea sandstones exhibit highly tortuous pore networks that can create pockets of fluid with circulation patterns and flow retardation. However, the motion of NPs injected into the empty space of the rock will not be significantly affected by those regions, since the particles would tend to follow streamlines that guide them to the outlet. Such behavior was affirmed by conducting tracer particle simulations in the Lagrangian framework (not presented herein). Briefly, after the velocity field was computed by the lattice Boltzmann simulation, a set of conservative tracers was injected into the pore space of the examined Berea sandstone sample using the technique described in Voronov et al.[48] and in Section II.2. The results of these simulations indicate that the tracer particles follow the streamlines guiding them to the outlet of the porous domain rather than entering low velocity regions within the pore network. Such low velocity regions include negative and near-zero velocities that can dramatically delay the particle effluent time. It is then reasonable to reconstruct the stress distribution after filtering out stresses caused by negative velocities. The reconstructed stress distribution of the examined Berea sandstone in dimensionless and dimensional form is depicted in Figure V.5a and Figure V.5b, respectively.
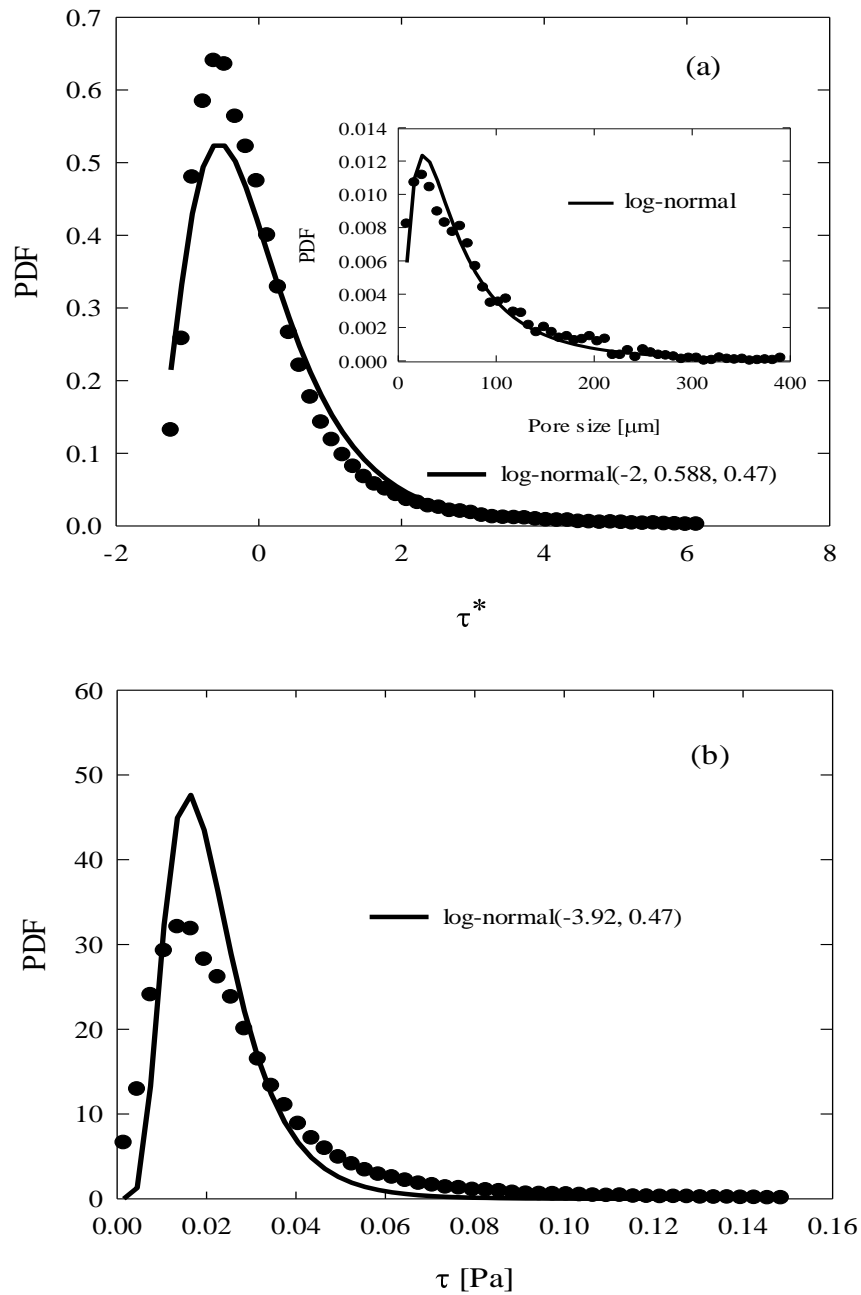
Figure V.5. Stress distribution in the pore spaces of the $0.9^2 \times 1.8 \text{mm}^3$ Berea sandstone slab in dimensional and dimensionless form. (a): Normalized stress distribution in comparison to the common 3P log-normal. The insert illustrates the pore size distribution of the Berea slab; (b): Dimensional stress distribution along with its prediction, computed from the log-normal(

$$0.588 + \ln\left(B\frac{\mu}{2\sqrt{k}}U_S \right), 0.47 \right).$$

Note that the stresses over 0.15Pa are not included in these distributions, since the probability of finding stresses above that value is extremely low, and thus are neglected. The KS test results with the null hypothesis: "the actual PDF follows the 3P log-normal(-2, 0.588, 0.47) distribution" indicated that the null hypothesis cannot be rejected at $\alpha = 0.2$ (p value is 0.92).

It should be noted that this PDF form is found to be similar to the shape of the pore size distribution for the Berea sandstone presented as an inset in Figure V.5a. As was also found using the model of a bundle of capillary tubes, there is a theoretical connection between the pore size distribution and the stress distribution in the pore spaces of a porous medium. The prediction for the dimensional stresses is log-normal(-3.92, 0.47), obtained by plugging k and U_S into the predictive formula, i.e. the log-normal$[0.588 + \ln\left(B \dfrac{\mu}{2\sqrt{k}} U_S\right), 0.47]$ with B = 1.41, is presented in Figure V.5b. (See Table V.1 for the permeability of the Berea slab and other geometries.) It is apparent from Figure V.5b that the acceptance of the null hypothesis: "the dimensional PDF follows the predicted log-normal(-3.92, 0.47)" at $\alpha = 0.2$ (p value is 0.29) implies that the predicted stress distribution holds even for structures with low porosity and sophisticated pore network like Berea sandstone. While Figure V.5b is a presentation of the same data as in Figure V.5a in dimensional form, Figure V.5b provides a visual assessment as to how well the predicted 2P log-normal fits to the dimensional stress data. It is also apparent from Figure V.5b that further considerations are needed to determine the value of the geometric factor B for the reservoir rock type geometries.

CHAPTER VI. TRANSPORT OF NANOPARTICLES AND KINETICS IN PACKED BEDS

VI.1 Introduction[§]

Engineered nano-sized particles, or NPs, have recently attracted much attention due to their potential for applications in various sectors of engineering. This class of materials possesses unusual and unique physical, chemical, and mechanical properties that make them ideal for many significant applications[157-162]. Metal-based NPs, for example, have found applications in improving biosensors, in cancer therapy, cell labeling, and targeted drug delivery[31, 163]. Likewise, carbon-based NPs have been intensively utilized in high-flux membranes, composite fillers, pollution prevention, and energy storage[164-168]. At the same time, concerns have been raised that the widespread use of NPs would lead to releases of significant amounts of them into the environment. Due to their tiny size, NPs released uncontrollably can migrate through soils and sentiments and can penetrate deeply in the subsurface, reaching aquifers and groundwater resources[169-171]. In other situations, however, the dispersion of NPs in the pore space of a porous medium might be desirable, when one wants to track the path of injected hydraulic fracturing fluids or to potentially affect enhanced oil recovery in petroleum reservoirs[172].

To protect the aquifers and mitigate environmental risks, better prediction of NP transport in soil, or porous media in general, is highly desirable. Flow-through experiments with granular material packed columns are usually conducted to investigate

---

[§]Most of the material presented in this chapter has been published in N. H. Pham, D. P. Swatske, J. H. Harwell, B. J. Shiau, and Dimitrios V. Papavassiliou, 2014, International Journal of Heat and Mass Transfer, **4**, 319-328.

the effect of various factors on the transport of NPs, as well as their interaction with the pore surfaces. It has been shown that propagation of NPs through the pores can be hindered by size exclusion (or straining), but most importantly by pore surface deposition effects[30, 173-175]. The former effect is simply the physical retention of particles by the porous medium due to the larger size of dispersed particles relative to pore throats[176]. In the case of NPs, straining might occur due to agglomeration of the NPs. It has also been found that breakthrough or retention of a particle in the column depends on several parameters, such as the pH of the NP suspension, the ionic strength of the aqueous phase, the surface charge of the medium, the surface roughness, the pore fluid velocity, and the size of the particle[30, 177-187]. In addition to experiments conducted in physical models, particle breakthrough behavior is predicted by utilizing the one-dimensional convective-diffusion equation[188, 189]. The terms of this mathematical equation indicate that the rate of change of particle concentration in the effluent is controlled by molecular diffusion (due to Brownian motion), convective diffusion (due to an external driving force), and the saturation level of deposited particles onto the pore surface area. Among these, the accurate modeling of the physics related to the pore surface saturation has attracted significant attention. As a result, the filtration equation has evolved to account for surface saturation by introducing a nonlinear term representing the so-called *blocking effect*[190-192]. In addition, particles lost due to size exclusion can also be accounted for by adding a straining term into the convective diffusion equation[193].

In this work, we present a numerical approach to the transport and kinetics of NPs migrating through the pore space. We adopt the LBM to simulate the flow of an

incompressible Newtonian fluid creeping through an infinite array of spheres packed in a random manner. Sequentially, a set of passive particles, representing the NPs, are injected into the flow field and the trajectory of each individual particle is monitored in space and time using the LPT algorithm. The instantaneous position and velocity of each individual particle is calculated and recorded in each time step. To simulate the attachment and detachment kinetics, particles are assigned a probability value related to their retention rate when they collide with the wall, and when attached a different probability related to their remobilization and detachment rate from the wall (see Section II.2). To validate our simulation approach, laboratory experiments were conducted in a column packed with inert glass beads, and the simulation results were further compared with theoretical predictions. The NPs were purified MWCNTs that were stabilized in suspension with the use of polymers.

VI.2 Simulation setup and experimental methodology

VI.2.1 Simulation setup

Geometries for the simulations consist of typical ideal sphere packing arrays (bcc, fcc, and sc) and arrays of spheres packed in a random manner. Figure VI.1 is a visualization of these packing styles in the simulation box. Among these, arrays of randomly packed spheres were created by using event-driven molecular dynamics and a modified Lubachevsky-Stillinger algorithm[136]. The spheres were considered to be rigid and impermeable. Simulation boxes were all meshed such that $nx \times ny \times nz = 101 \times 101 \times 101$.
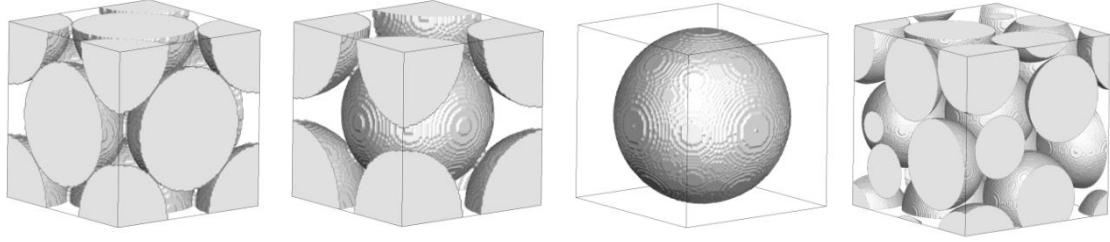
Figure VI.1. Types of sphere packing employed in this study. From left to right: fcc, bcc, sc, and randomly packed spheres.

The choice of this mesh size is a balance between grid independence[26] and reasonably fast convergence. Table VI.1 is a summary of simulation configurations and conditions implemented in the simulations presented in this work.

Table VI.1. Simulation configurations and conditions

Simulation	Box size [μm^3]	$\Delta P/L$ [Pa/m]	Packing manner	d_c mm]	ϕ	Presented in figure
1	375^3	687	Random	0.15	0.35	VI.3
2	1798^3	100	Random	1	0.55	VI.4, VI.5
3	1798^3	100 - 500	Random	1	0.55	VI.7, VI.8
4	1414^3	100	fcc	1	0.267	VI.8
5	1143^3	100	bcc	1	0.325	VI.8
6	1000^3	100	sc	1	0.476	VI.8
7	375^3	100	Random	0.15	0.35	VI.6, VI.9, VI.10

Note that the reported permeabilities were directly calculated from simulations by employing Darcy's law for flow in low Reynolds number regime. Briefly, a series of simulations with various pressure drops were performed for each sphere packing type, yielding different values of superficial velocity. A plot of superficial velocity versus pressure drop was then constructed and the permeability was obtained from the slope of the line.

At the beginning of the LPT implementation, 100,000 particles were randomly and uniformly released at the inlet plane, which was perpendicular to the flow direction. These particles (with initially assigned p_a and p_d) often collided with the pore walls and underwent the attachment-detachment process, leading to different residence time for the particles. At the outlet plane, one simulation box length away from the inlet, exit particles were captured and counted within an interval of 0.05 dimensionless particle residence time, that is related to the pore volume (PV). This dimensionless time scale is the ratio of the particle residence time over the average residence time at which a particle travels through the porous medium with a velocity equal to the mean fluid velocity (or pore velocity) without deposition. The concentration ratio (C/C_0) is then interpolated from the number of particles injected and the number of particles found in each PV interval as follows

$$\frac{C}{C_0} = \frac{N}{N_0} \frac{\text{number of PV injected}}{\text{PV interval}} \qquad \text{(VI.1)}$$

where C is the particle concentration in each PV interval, C_0 is the initial particle concentration in the solution, N is the number of particles captured in each PV interval in LPT simulation, and N_0 is the number of particles, initially released in the LPT simulation.

VI.2.2 Experimental set up[**]

Nanoparticles: The NPs used in this work are purified MWCNTs, stabilized by a mixture of polyvinyl-pyrrolidone (PVP with molecular weight = 40,000, Sigma Aldrich Lot#080M0242V) and a stabilizing polymer obtained from DOW Chemical

---

[**]Experiments were conducted by Daniel Swatske (D. P. Swatske, 2013, Development of binary dispersant systems for nanoparticle transport in porous media, Master thesis, University of Oklahoma). The description is offered here in order to provide complete information.

Corporation (Lot#B-1222LABS) subject to a confidentiality clause that does not allow us to determine its composition. The purified MWCNTs were obtained after purification of MWCNTs-Al_2O_3 particles with the process described in detail in Baez et al.[194]. The obtained purified MWCNTs were stabilized by sequentially adding PVP and the DOW proprietary polymer in 10% standard API brine (i.e., 8wt% NaCl and 2wt% $CaCl_2$). Briefly, the procedures involved first sonication (sonicator model FB505, Fisher Scientific) of a solution of 100ppm purified MWCNTs and 250ppm PVP in API brine at 25% amplitude for 2 hours. After 750ppm of the DOW proprietary polymer was added to the solution, a second run of sonication took place for another 30 minutes. Finally, the dispersion was centrifuged for 1 hour at 2000rpm to remove any excessively large particle agglomerates that were not adequately exfoliated during multiple sonications[194].

Column packing and propagation experiment: Inert glass beads of 1mm diameter were packed into a low pressure glass column (Kimble Chase, Kontes Chromaflex) of 2.54cm inner diameter. Dry packing was employed until the column height reached two targeted heights: either 2.54cm or 7.62 cm (one or three-inch height), yielding a porosity of 0.55 (see Figure VI.2 for experimental set up). The packed column was then saturated by injecting 10PV of the 10% brine to ensure equal ion concentration in the effluent and the injection. A Masterflex L/S peristaltic pump (Cole Parmer) was used to inject experimental fluid from a reservoir into the column. Sequentially, either a pulse injection (3in-column) or a 2PV of continuous injection (1in-column) of the dispersed PMWCNT solution was injected from bottom to top at the volumetric flow rate of 0.3mL/min, followed by a 5PV post-flush with the particle-free API brine solution. During the injection with the particle suspension, the column remained saturated with

prior API brine. Effluent samples were automatically collected at every 0.5PV (for the 1in-column) or 0.25PV (for the 3in-column) using a timed sample collector. Particle concentration in each PV interval was then measured by a UV-vis spectrophotometer (Thermoscientific, Genesys10s) using 3.5mL quartz cuvette by comparing the readings with a calibration curve prepared daily.
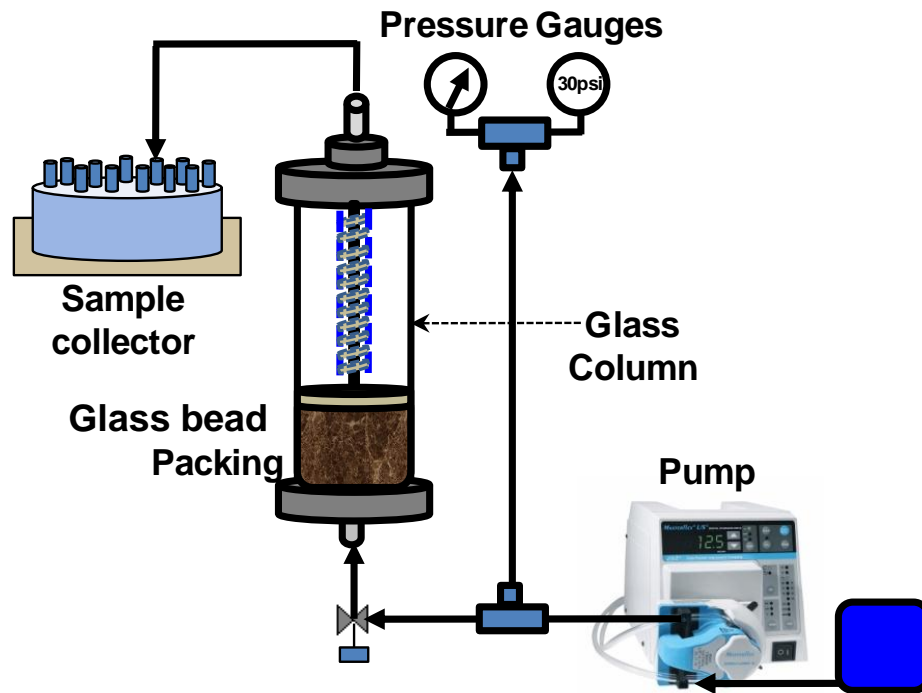
Figure VI.2. Schematic diagram of column experiments with glass bead packing.

VI.3 Results and discussion

As described earlier in the LPT implementation section, particle breakthrough behavior is subject to change upon different values of p_a and p_d. The numerically-obtained particle breakthrough curves are presented in Figure VI.3 for different p_a and p_d at two different injection modes: a pulse of 1.76×10^{-5}PV and a 5PV injection.
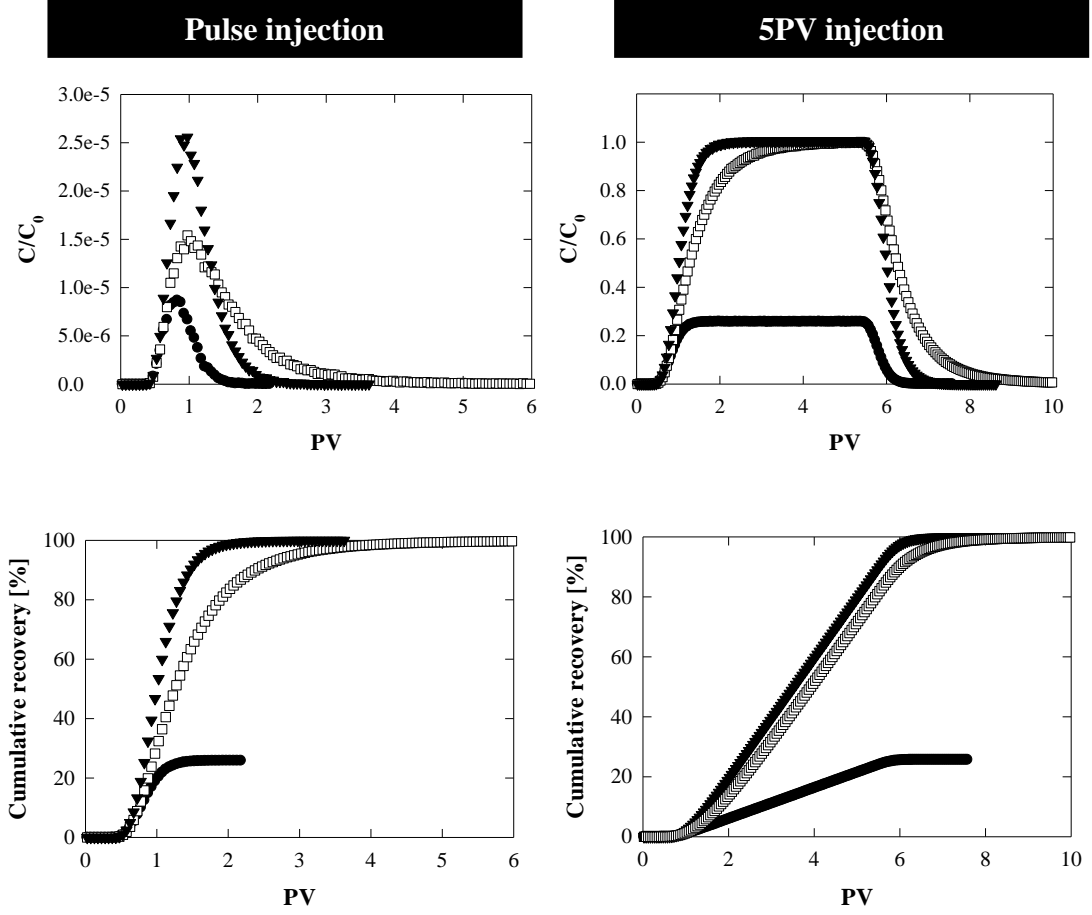
Figure VI.3. Breakthrough and cumulative recovery curves of particles passing through a randomly packed array of spheres with 0.35 porosity. ▼ $p_a = 0$, $p_d = 0$; ● $p_a = 0.01$, $p_d = 0$; □ $p_a = 0.01$, $p_d = 0.0001$. The panels on the left are for the case of an instantaneous pulse injection, and the panels on the right are for a 5 pore volume (PV) injection.

The properties of water at room temperature were used to describe the fluid that was passed over the sphere packing by a pressure difference of 687Pa/m. Released NPs were assumed to be spherical with 10nm in diameter, resulting in the Sc = 21880 based upon the Stokes-Einstein relation for particle diffusion with the Cunningham correction[195]

$$D_0 = \frac{C_n k_B T}{6\pi\mu r_p} \tag{VI.2}$$

where C_n is the Cunningham correction factor, k_B is the Boltzmann constant, T is the absolute temperature, and r_p is the particle radius. In order to simulate a continuous

injection into the porous medium, data from the instantaneous injection were used instead of continually adding NPs in the simulation in each time step. For example, in order to determine how many particles migrate through the column from the initial injection at time t_o to time $t_o + t$, the number of particles that go through the column for pulse injections at time t_o, $t_o + \Delta t$, $t_o + 2\Delta t$, $t_o + 3 \Delta t$ ... $t_o + t$ are calculated and summed up.

In either pulse or 5PV injection scenario, the most favorable case in which particles were free from deposition ($p_a = 0$) is shown. It is obvious that in this case no particle retention is recorded (100% recovery of the particles is observed, as can be seen in the cumulative recovery curve – filled triangles) irrespective of what the injection manner was, and the delay of particle breakthrough is likely due to some particles that move through the column in regions with slow velocity. This case corresponds to the breakthrough of conservative tracer particles in common column experiments. In contrast, more than 74% of particles are lost if $p_a = 0.01$ with no detachment ($p_d = 0$, Figure VI.3 – filled circles). This case is equivalent to conducting a column experiment without post-flushing the column with particle-free solution. The case in which particles are allowed to detach from the wall and remobilize is also presented, utilizing a specified detachment probability for attached particles ($p_a = 0.01$ and $p_d = 0.0001$). Similar to the case of tracer particles, 100% particles are recovered in this case, and the breakthrough curve is skewed to the right with a long tail. It can be anticipated that, for non-zero p_a and p_d, the larger the p_a/p_d ratio is, the longer the right tail of the breakthrough curve. This occurs when the detachment rate is significantly smaller than the attachment rate, causing a delay in the elution of the particles. Ideally, if the

particles are all in constant contact with the pore walls and the attachment rate is of first order, p_a in our model can be linked to the nominal attachment rate constant k_0 as expressed below [48]

$$k_0 = \frac{1}{\Delta t} \ln \left(\frac{1}{1 - p_a} \right) \tag{VI.3}$$

VI.3.1 Validation with experiments

In Figure VI.4 and Figure VI.5, breakthrough curves of tracer particles generated by LBM/LPT simulations ($p_a = 0$) are compared to those of PMWCNTs obtained by experimentally injecting the dispersed PMWCNTs through the bead-packed columns. Figure VI.4 is a presentation of results for a pulse injection of 0.087PV of suspension through the 7.62cm high column (the 3in column), whereas Figure VI.5 is a presentation of results for 2PV injection of the same suspension.
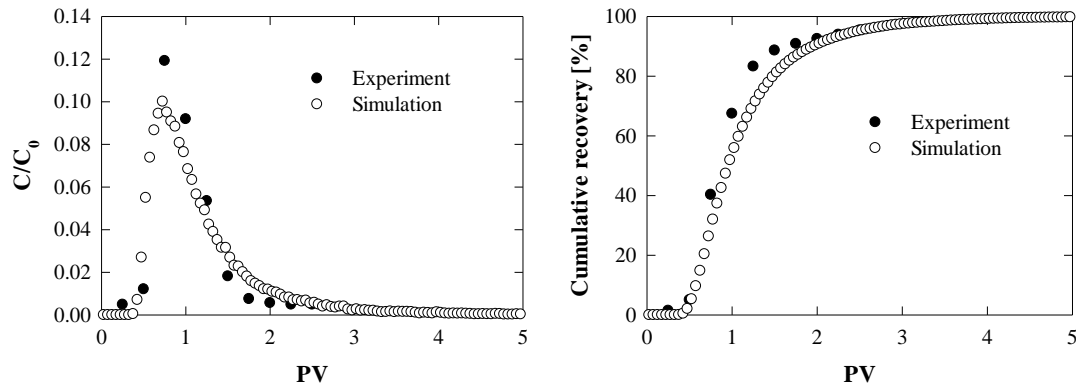
Figure VI.4. Simulation of conservative tracer versus dispersion of PMWCNTs in the inert glass bead packed column. The experimental column is of 3in-height and 0.55 porosity. NPs were introduced into the pore matrix as a pulse input.

It is noticed from Figure VI.4 that PMWCNTs are retained by neither pore surface deposition nor size exclusion, and the cumulative recovery curves plateau at 100% in both cases. Early breakthrough in the experimental column is observed when the

experimental breakthrough curve reaches a peak level (C/C_0) at about 0.12 against 0.1 from the simulation prediction. In contrast to this difference, the position of peak concentration is almost identical. A deviation of the peak values is expected from the pulse injection in the bead-packed column, mainly due to instrumental constrains. In the experiment, samples were collected at every quarter of a PV and the particle concentration was measured with light absorbance. Due to the pulse injection, the highest particle concentration in the effluent sample is fifteen times smaller than the injected concentration and collecting samples at smaller PV intervals would lead to measurements around the detection limit of the equipment. This average of the results over a fourth of a PV in the experiment can lead to differences with the simulation. However, in general, the agreement between the simulation data and the experimental results is quite reasonable. Later, to overcome the measurement uncertainty, 2PV of suspension was injected in a continuous manner into the column, instead of a pulse input. The comparison between these experimental results and simulations is depicted in Figure VI.5.
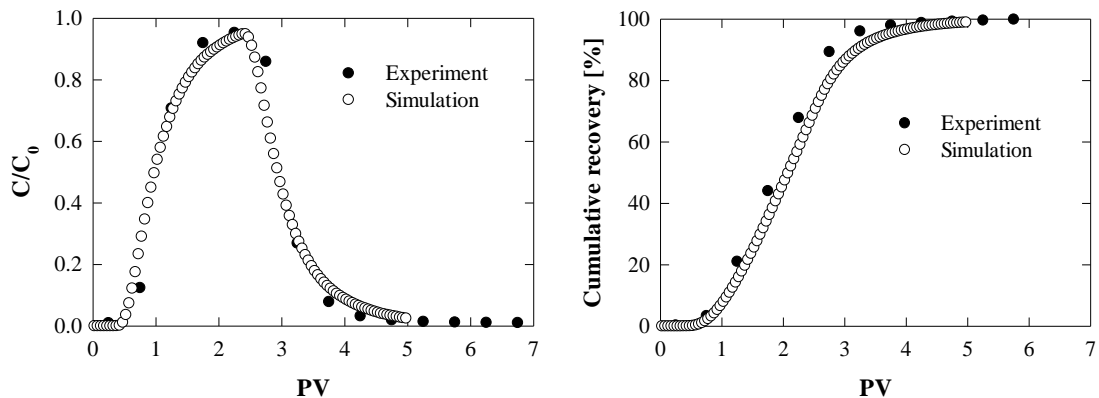
Figure VI.5. Simulation of conservative tracer (i.e., $p_a = p_d = 0$) versus dispersion of PMWCNTs in the inert glass bead packed column. The experimental column is of 1in-height and 0.55 porosity. NPs were introduced into the pore matrix as a 2PV input.

Note that the column length in this case (1-in column) was one-third of the above-described experiment (i.e., 3-in column). The results in Figure VI.5 reveal that the agreement between experiments and simulations is improved, and both the peak position and the concentration value at the peak are identical.

VI.3.2 Validation with theoretical predictions

In addition to comparisons to experiments, validation of our simulation results can be done by using the conventional one-dimensional convective-diffusion equation[188, 189]. The governing equation is based on Fick's second law of diffusion with the convective and particle filtration terms added

$$
\begin{cases}
\dfrac{\partial C}{\partial t} = D_h \dfrac{\partial^2 C}{\partial x^2} - u \dfrac{\partial C}{\partial x} - \dfrac{\rho_b}{\phi} \dfrac{\partial S}{\partial t} \\[2mm]
\dfrac{\partial S}{\partial t} = \dfrac{\phi}{\rho_b} k_a C - k_d S
\end{cases}
\tag{VI.4}
$$

where D_h is the hydrodynamic dispersion coefficient of the particles in the porous media, u is the pore velocity, ρ_b is the bulk density of the column, S is the deposited particle concentration, k_a is the attachment rate constant, and k_d is the detachment rate constant. Exact solution for this nonlinear unsteady state equation with a pulse input boundary condition at the inlet is known for specific cases. For a pulse injection of particles and conditions of irreversible deposition, the distribution of the particle concentration at different times and column locations downstream is given by[185, 196]

$$
C(x,t) = n_0 \frac{x}{2\sqrt{\pi D_h t^3}} \exp(-k_a t) \exp\left[-\frac{(x - ut)^2}{4D_h t} \right]
\tag{VI.5}
$$

where n_0 is the ratio of the total volumetric amount of particle solution injected to the volumetric flow rate, and x is the location along the flow direction. This equation is

useful in order to upscale simulation results by fitting them with this equation and obtaining, thus, the two macroscopic parameters, D_h and k_a, accounting for the irreversible deposition kinetics. For constant fluid velocity and particle diffusivity, the particle concentration in the fluid at a certain column location is affected by k_a, and the higher the attachment rate the smaller the particle concentration. The attachment rate, k_a and the predefined attachment probability, p_a, in our simulation have the same physical meaning, and establishing their relation is now straightforward. Additionally, so long as k_a is known, calculating the single collector efficiency, η, is also straightforward. The term *single collector efficiency* represents the ratio of the number of NPs striking a single glass bead (the collector) over the number of particles approaching the collector in a unit of time[197]. This parameter can be directly correlated to k_a as[198, 199]

$$k_a = \frac{3}{2}\frac{(1-\phi)}{d_c\phi}U_S\eta \qquad\qquad (VI.6)$$

where η is the single collector efficiency and d_c is the collector diameter. Knowing the value of η is helpful in determining the travel distance, ℓ, in which a certain fraction (1-C/C_0) of particles are captured by the porous medium

$$\ell = -\ln\left(\frac{C}{C_0}\right)\left[\frac{2d_c}{3(1-\phi)\eta}\right] \qquad\qquad (VI.7)$$

At this point, it is of importance to emphasize that Equations (VI.6) and (VI.7) allow the upscaling of the mesoscopic simulation results to apparent parameters that are macroscopically observed in the column experiment.

Figure VI.6*a* is an illustration of how well our simulation results fit to Equation (VI.5). As seen in Figure VI.6*a*, simulation predictions agree with Equation (VI.5), and out of each variation of p_a, a pair of k_a and D_h is obtained. The relationship between k_a

and p_a is presented in Figure VI.6*b* for two different Sc number cases: 21880 and

233545, corresponding to two different sizes of NPs with diameters 10nm and 100nm.

The pulse experiments and the data-fit to Equation (VI.5) also determine how the

hydrodynamic dispersion coefficient, D_h, behaves when the deposition rates change. It

turns out that there is a rather small deviation from the mean value of D_h at various p_a in

the two cases of Sc simulated ($D_{h\text{-}ave} = 5.83 \times 10^{-7} \pm 1.06 \times 10^{-8}$ and $6 \times 10^{-7} \pm 1.03 \times 10^{-8}$cm^2/s at Sc = 21880 and 233545, respectively).
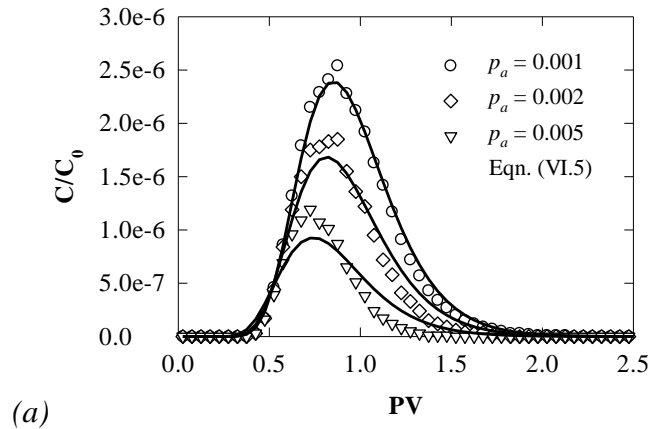
(a)
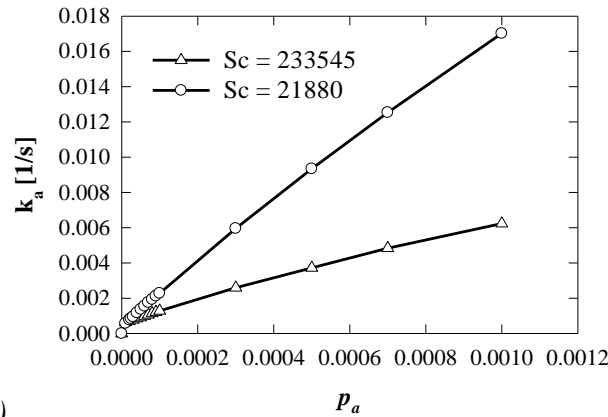
(b)

Figure VI.6. (*a*) Agreement between simulation data and the predictions from Equation (VI.5) for a pulse release. There is irreversible deposition at Sc = 233,545. (*b*) Variation of k_a at various p_a at two different Sc.

This finding suggests that the hydrodynamic dispersion coefficient of the NPs is affected mostly by their physical properties (*e.g.,* particle size) and flow conditions rather than the deposition rate. Thus, one can conduct a tracer experiment (with no deposition) for the particle of interest and determine D_h, which would still hold for other cases where particle deposition is involved.

In the conventional filtration theory, particle deposition is formulated with a first order kinetics term, as seen in Equation (VI.4). In our simulation, this first order rate law is simulated by creating random numbers and comparing them to the predefined p_a, and this approach is found to be consistent with the theory, as evidenced by a monotonic increase of k_a versus p_a in the small p_a region on Figure VI.6*b*. It is also seen in Figure VI.6*b* that the slope of the k_a-p_a relation for small p_a decreases with increasing Sc, which implies that, at a particular p_a, the attachment rate is higher at smaller Sc. This finding is consistent with the role of the Brownian motion of particles at small Sc. The smaller the Sc, the farther the particles can jump off the fluid streamlines due to random Brownian movement and the more often they can collide with the pore walls, thereby giving particle deposition a higher chance to occur. Note that the Brownian motion is explicitly accounted in the LPT algorithm through the standard deviation σ of the probability distribution that the random jumps follow. If the mass retention is only via particle deposition as assumed in LBM/LPT simulations, it can be concluded from Equation (VI.2) that large particles are unfavorable for deposition[193]. A similar observation was reported in the work of Ko and Elimelech[179] when they experimentally investigated the surface coverage efficiency under various flow rates, ionic strengths, and particle sizes. In Figure VI.6*b*, the decrease of k_a with increasing Sc and vise versa

implies that the particle deposition process is reaction limited at large Sc, and that is convection limited with small Sc. The role of these two factors can be revealed with the Damköhler number, the dimensionless quantity that accounts for the characteristic fluid time over the characteristic chemical reaction time

$$Da = \frac{k_0 \sqrt{k}}{u} \tag{VI.8}$$

where Da is the Damköhler number. In the expression of Da, $\sqrt{k}$ is used as the length scale instead of the column length, since the column length is unreasonable for considering an infinite medium. Another possibility would be to use the bead diameter, d_c, as the length scale. However, for the case of a porous column with monodisperse beads the use of the medium permeability in Equation (VI.8) is equivalent to the use of the representative collector diameter, since $\sqrt{k} \sim d_c \phi^3/(1-\phi)^2$, found by substituting Darcy's law into the Blake – Kozeny equation. In addition, using the medium permeability to obtain a length scale helps to differentiate between different configurations of the porous medium, including polydisperse bead diameter columns and unconsolidated porous media, and provides generality to Equation (VI.8). It should be further noted that the Da - type (I) is used instead of the Da - type (II), since no significant interphase mass transfer limitation exists in our results. The calculated diffusion layer thickness corresponding to each case of simulations is less than 1.5nm (data not shown).

Figure VI.7 is a log-log plot of k_a at various Da, when the porous medium is represented by the randomly packed spheres array at three different p_a.
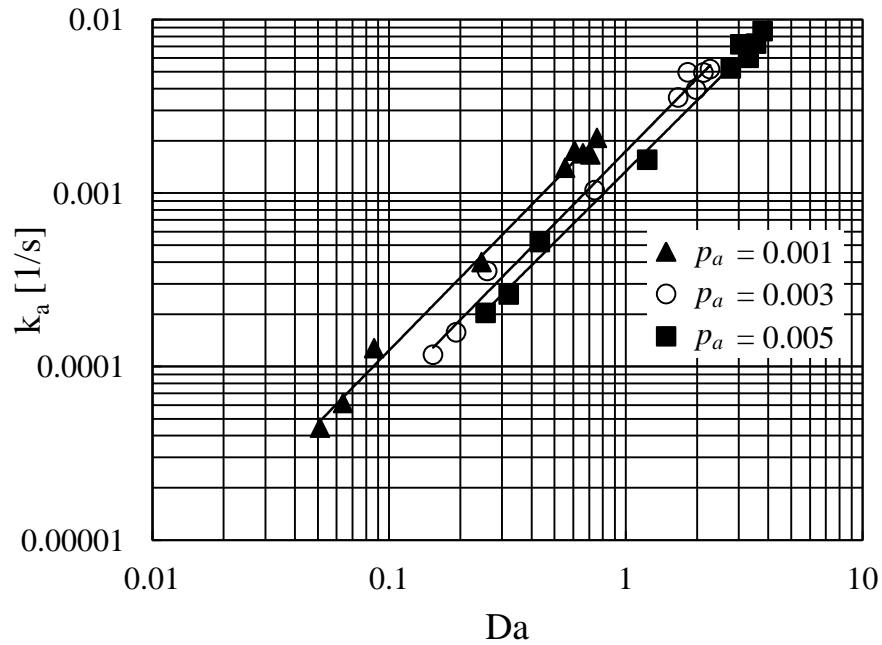
Figure VI.7. Relation between the Damköhler number and the attachment rate constant in a randomly packed array of spheres. Data obtained from simulations with constant pressure drop ($\Delta P/L = 100Pa/m$) and variable Sc (Sc = 384, 1000, 5000, 10000, and 20000) and simulations with constant Sc (Sc = 384) and different pressure drops ($\Delta P/L$ = 200, 300, 400, and 500Pa/m).

Notice that four different simulations at constant pressure drop (constant u) but different Sc (k_0 changed) and another five simulations with changing u but constant Sc were carried out to yield a series of Da and k_a. In our model, k_0 is determined by the simulation conditions (see Equation VI.3), so different flow velocities also indicate changes in k_0. It is apparent from Figure VI.7 that k_a is logarithmically proportional to Da and the slope is qualitatively unchanged despite different p_a. The fitting equations are recorded to be $k_a = 0.0031Da^{1.4}$, $k_a = 0.0017Da^{1.39}$, and $k_a = 0.0013Da^{1.36}$ from the smallest to the biggest p_a, respectively. The same relation is logarithmically depicted in Figure VI.8 with different sphere packing morphologies and constant p_a of 0.001. Series of Da were obtained by keeping u unchanged and Sc varied in five distinct simulations for each type of sphere array.
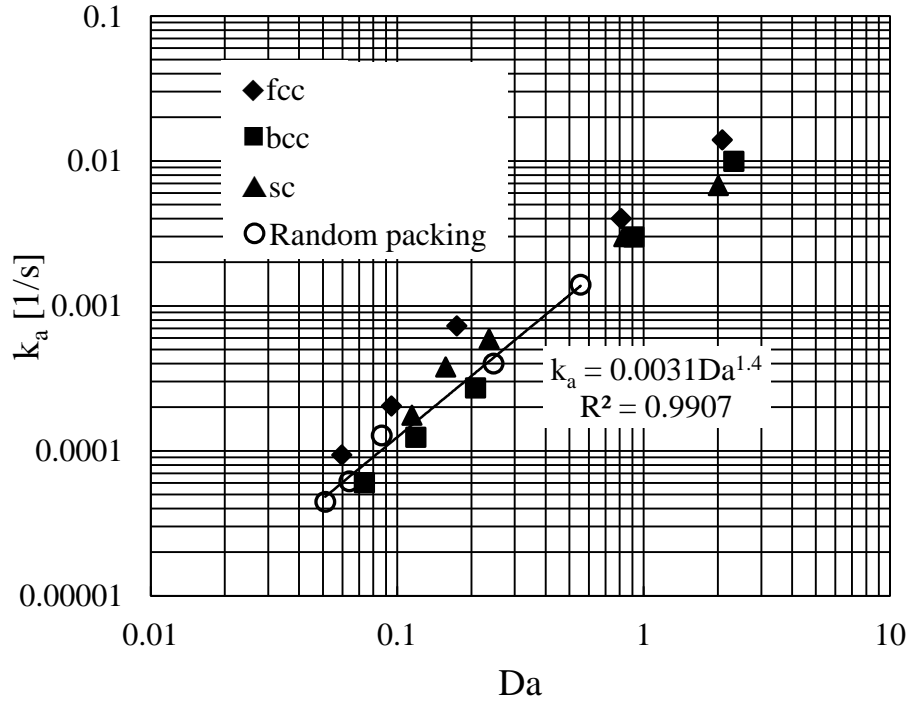
Figure VI.8. Dependence of attachment rate constant on Damköhler number under different geometric morphologies. Simulations were conducted under a constant pressure drop ($\Delta P/L$ = 100Pa/m), a constant attachment probability (p_a = 0.001), and a range of Sc (Sc = 384, 1000, 5000, 10000, and 20000). The fitting equation presented is for randomly packed spheres.

The data in the plot are seen to be correlated with a power correlation. Particularly the fitting equation to data points of random packing spheres turns out to be

$$k_a = 0.0031 Da^{1.4}. \tag{VI.9}$$

Substitution of Equation (VI.8) in Equation (VI.9) indicates that the non-linear correlation between Da and k_a can be due to a non-linear relation between the attachment rate constant k_a and the nominal attachment rate constant k_0, and/or due to a non-linear relation of k_a and the pore velocity u. A non-linear relationship between k_a and *u* would be in agreement with the theory of Tufenkji and Elimelech[199], where it is argued that $k_a \sim U_S \eta_0$, with η_0 being a non-linear function of U_S and, thus, of u. One would expect that the value of k_a would depend on the flow, on the pore structure, and

on the diffusivity of the particles. Figure VI.7 is an indication that convection and pore structure are more important than diffusion. The effect of the medium configuration on particle dispersion and deposition is remarkable, and that might be due to either the tortuosity and/or the porosity of the medium.

Similarly, the detachment probability in the LBM/LPT simulation can be correlated to the detachment rate constant, k_d, by matching the solution of Equation (VI.4) to the simulation data when particle detachment is activated in the simulation. Unfortunately, solving this equation analytically with no sink term is not trivial. We instead used the method of lines, a general finite difference technique for the numerical solution of partial differential equations, in which the central difference representation was employed for the first and second derivatives in space[200]. The accuracy of the central differencing scheme has been proven to be second order[201]. Figure VI.9 is a depiction of the relation of p_d versus k_d at identical simulation conditions as in Figure VI.6, except p_a stays unchanged at 0.001 ($k_a = 0.00631s^{-1}$) and p_d is varying from 3×10^{-6} to 1. It is evident from Figure VI.9 that k_d monotonically increases with p_d at $p_d < 10^{-3}$. This behavior is expected, as first order kinetics are applied to simulate the detachment process. Notice that, in our LPT algorithm, the detachment process is allowed to take place after the first particle gets deposited on the sphere, and detachment of a particle is not hindered by others that are moving toward the same collector.
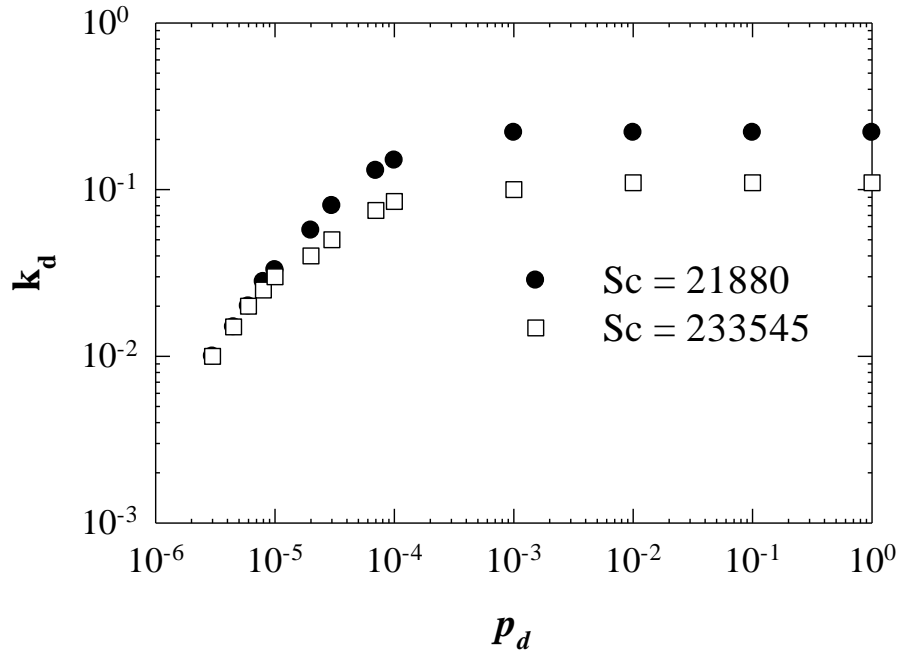
Figure VI.9. Variation of k_d at various p_d for two different Sc at reversible deposition condition. The value of the p_a was fixed at 0.001 and p_d was varied from 3×10^{-6} to 1. Other than that, the simulation conditions were identical to those depicted in Figure VI.6.

There is no doubt that the delay in the particle breakthrough in the absence of size exclusion effects is controlled by the probability of detachment, p_d. In other words, particle retention in this case is detachment limited. Figure VI.10 is a presentation of the dimensionless elapsed time (presented in terms of PV) at which all the particles are recovered for various detachment rates (left panel) and equilibrium coefficients (right panel) at two different Sc numbers. The equilibrium coefficient is the ratio of attachment rate constant over detachment rate constant, and is denoted by *K*.
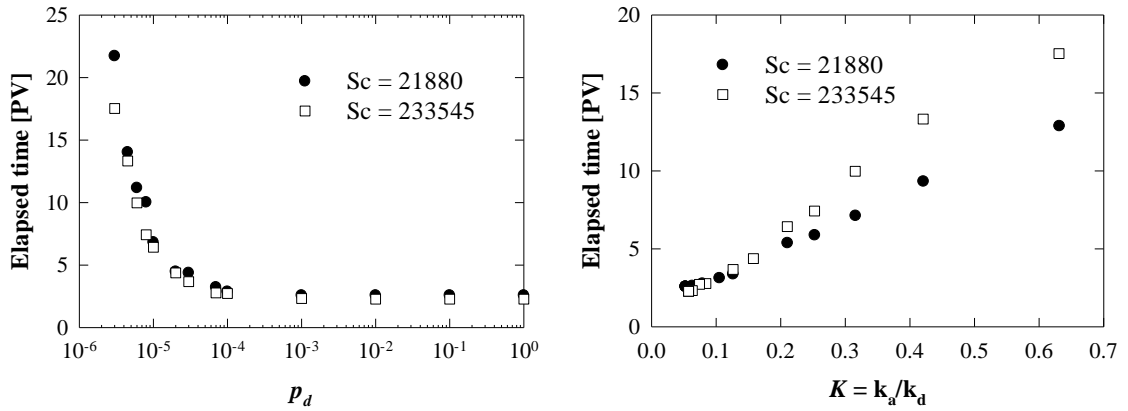
Figure VI.10. Elapsed time for complete particle recovery versus p_d (left plot) and equilibrium constant, K (right plot).

The plot on the left indicates that the delay in particle breakthrough is pronounced at p_d $< 10^{-3}$ for the two studied Sc. Recall that k_d is almost constant at $p_d > 10^{-3}$ as seen in Figure VI.9, and thereby the data presented in the left plot of Figure VI.10 are not contradictory. It is also seen in this plot that particles with higher Sc cause an earlier breakthrough than those with smaller Sc. Longer retention of smaller Sc particles is expected due to higher collision frequency with the pore surfaces with the same probability of attachment and detachment. Likewise, the plot on the right demonstrates the dependence of the elapsed time scale on different K. In contrast to the tendency recorded on the left one, particles with smaller Sc demonstrate an earlier breakthrough at a certain K, and the difference is more significant when K increases.

CHAPTER VII. NEW FILTRATION EQUATION TO PREDICT TRANSPORT AND KINETICS OF PMWCNTs IN PACKED BEDS

VII.1 Introduction

The world energy demand is projected to maintain a rapidly growing trend in the next few years and might reach 14,500 megatonne of oil equivalent (Mtoe) in 2040[117, 202]. Despite the increase of energy production from alternative sources, such as nuclear and renewable energy, it is expected that traditional hydrocarbon sources will continue to dominate global energy markets[117]. As the demand for oil and gas is strong, it is quite appealing to recover residual oil, which is estimated to be nearly $2x10^{12}$ barrels of conventional oil and $5x10^{12}$ barrels of heavy oil in reservoirs worldwide after the use of current enhanced oil recovery technologies[203]. On the other hand, ideas for improving sweep efficiency by either improving the mobility ratio between oil and displacing fluids or changing the wettability of rock surfaces at oil-rock interfaces using nano-fluids are promising for overcoming current technological and economical difficulties in tertiary recovery[41, 204, 205]. Mobility control is feasible by reducing the interfacial tension between displaced and displacing phase or increasing the viscosity of the displacing phase[41, 206]. Wettability alteration, on the other hand, is targeted at modifying rock surfaces from oil-wet to mixed-wet or water-wet[207]. If rock surfaces become more hydrophilic, residual oil will be expected to easily roll off from the surfaces in secondary flooding. If one were to employ NPs in the aforementioned ways, NPs would have to be present in the injected fluid. Nanoparticle mobility in highly tortuous pore networks, such as those of reservoir rocks, under harsh salinity and temperature conditions would be a challenge.

In general, it has been well-documented in the literature that various physical and chemical factors impact nanoparticle transport through porous media, both in a positive and a negative sense. These factors might involve size exclusion, pore surface roughness, and electrostatic repulsion/attraction due to the solution chemistry or patch-wise surface charge heterogeneity. To isolate and investigate each single factor, many experimental studies on nanoparticle transport have been conducted[176-178, 180, 182, 185, 197, 208].

Mathematical models have been proposed that capture the main physics of the process and can predict the effects of the aforementioned factors. Generally, these models can be classified into two categories: one-site models and two-site models. One-site models assume a uniform deposition rate of particles on the collector surface, while two-site models take into account the heterogeneity of the surface represented by a fast and a slow deposition rate constant. Among those classified as one-site models, the conventional filtration equation is widely used[188, 189, 191, 196, 209, 210]. The main feature of this equation is that the attachment and detachment of particles or colloids are modeled by first order kinetics[191, 196, 211]. In addition, it is implicitly assumed that the attachment capacity of the collectors is infinite, resulting in the absence of any term corresponding to the blocking parts of the surface from further deposition. This fact limits the validity of the model to cases where the surface coverage is negligible[191]. Reversely, when the deposition rate of particles or colloids in the bulk phase is noticeably affected by the already attached particles, a Langmuirian blocking function is usually incorporated[30, 186, 191, 212]. The incorporation of a blocking function changes the assumption about the kinetics of the deposition process from first order to second order. Unlike the

conventional filtration model, no plateau behavior (steady state) is observed in the Langmuirian blocking model, unless the collector surfaces are completely saturated[191].

It has been shown that the one-site model with Langmuirian blocking successfully captures the gradual climb of experimentally obtained particle breakthrough curves after the clean bed state, and before the complete saturation state, in different ionic strengths of the electrolyte solution[30]. Despite that, it has been argued that the model with a Langmuirian blocking is inadequate in the case of big colloidal particles, since it was originally targeted to the coverage of point-size molecules on crystalline lattice sites[190, 213]. Thereby, using a Langmuir approximation for large colloidal particles, which can occupy many surface deposition sites at once, might cause some deviations. Instead, the random sequential adsorption (RSA) dynamic blocking function has been employed and found to be a significant improvement. The RSA blocking model is in fact based on the random placement of hard disks adsorbing on a flat surface without overlapping[190, 213, 214].

Together with the one-site models, two-site models have also been proposed. The term two-site means that surface charge heterogeneity is considered in the models, reflected by favorable and unfavorable deposition rate constants[215-217]. Similar to one-site models, if surface deposition site blocking is significant, the Langmuir approximation or RSA blocking might be included. Additionally, a heterogeneity parameter can be added as a weighting factor for the presence of favorable regions relative to unfavorable regions for deposition[197, 208, 218, 219]. So far, in the mentioned models, the retention of colloids and/or particles is attributed to chemical interactions between colloids and collector surfaces. In an attempt to elucidate the effect of physical

108

factors on colloidal retention, two-site models that employ a dual permeability concept and two-site models with a combination of chemical and physical non-equilibrium have also been developed[220-222].

Considering the agreement between experimental data and model predictions, it is found that two-site models, even without a blocking term, exhibit an improvement compared to the conventional one-site model[215, 216]. Furthermore, experimentally observed behavior, such as the gradual increase of the normalized particle concentration seen in experimentally obtained breakthrough curves after the clean bed state, is also well-captured. Note that, in the clean bed state, particles deposit onto collector surfaces with a constant rate with no interference of deposited particles[223]. It should be further noted that electrostatic repulsion is a factor that can hinder the deposition of colloids in regular conditions. Thereby, when electrosteric effects play a role and the suspension has rather high ionic strength (on the order of thousands mM), both one-site and two-site models might deviate notably from experimental measurements.

In this study, experimental breakthrough data for PMWCNTs that were stabilized in suspension by a polymer mixture and then propagated through columns packed with crushed Berea sandstone are presented. The columns were saturated with brine at different salt concentrations. The electrolyte solutions contained a mixture of sodium chloride (NaCl) and calcium chloride ($CaCl_2$) with different weight fractions, corresponding to different salinity levels. In addition, the effects of pore velocity on particle retention were studied. Finally, a new filtration equation with a modified blocking function is proposed, which is in good agreement with the experimental data.

VII.2 Materials and methods[††]

VII.2.1 Nanoparticles

Purified MWCNTs are employed in this work. To obtain the NPs, MWCNTs-Al$_2$O$_3$ particles supplied by SouthWest Nanotechnologies, Inc. (SWeNT), Norman, Oklahoma, USA, were purified by immersing them in flourhydric acid to dissolve the alumina core as described in detail in Baez et al.[194] and Kadhum et al.[224] The remaining MWCNTs were then dried. After purification, two polymer solutions were sequentially added to generate stable, suspended NPs that do not aggregate because of electrosteric effects. The envelopment procedure consisted of sonication (sonicator model FB505, Fisher Scientific) of a solution of 100ppm purified MWCNTs and 200ppm primary polymer in salt or salt-free solutions at 25% amplitude for 2 hours. In the column experiments, polyvinyl-pyrrolidone (PVP) of molecular weight 40,000 (Sigma Aldrich) was used as the primary polymer. Except for the case of deionized water, a mixture of NaCl and CaCl$_2$ was added into the solution at a fixed weight ratio of 4:1[224]. The weight percentage of the salt mixture in the solution series was 0% (deionized water), 0.1%, 5%, and 10%, with respective ionic strengths of $10^{-2.5}$, 19.1, 1010, and 2140mM. After the first sonication process, 1600ppm of hydroxyethyl cellulose (HEC-10, Dow Chemicals) was added, and a second sonication was operated for 30 minutes. The resulting suspensions then underwent centrifugation for 1 hour at 2000rpm as the final step to remove any large particle agglomerates. The reason for using two polymers is the following: the first polymer helps to stabilize and disperse the nanotubes and the second allows the suspension to be stable at different salinity levels. The effectiveness

[††]Experiments were conducted by Daniel Swatske (D. P. Swatske, 2013, Development of binary dispersant systems for nanoparticle transport in porous media, Master thesis, University of Oklahoma). The description is offered here in order to provide complete information.

of these particular polymers in disrupting the MWCNT – MWCNT hydrophobic interactions (using PVP) and resisting NP-pore surface deposition under harsh salinity conditions (using HEC-10) has been documented elsewhere[224]. Also, the addition of these polymers showed no interference with the UV-vis technique used for the measurement of the particle concentration, which is described in the section below.

VII.2.2 Crushed Berea sandstone column

Consolidated Berea sandstone was crushed with a ceramic mortar into grains. The obtained grains were subsequently sieved to different grain sizes in a mechanical shaker (sieve designations: #60/250 µm and #200/75 µm). The packing grains (referred to as sand grains from now on) were those that remained on the 250µm down to 75µm sieve, resulting into a grain size distribution of the packing material that was between 75µm and 250µm. The sand grains were dryly packed into a low pressure glass column (Kimble Chase, Kontes Chromaflex) of 2.54cm inner diameter until a column height of 7.62cm was achieved. After each experiment corresponding to one salinity level was concluded, the column was emptied and repacked to carry out experiments with different salt concentrations in the series of experiments. The average porosity and permeability of the packing column was 0.35 and 4.2D, respectively. The permeability of the packing column was measured by applying Darcy's law for low Reynolds number flow. Briefly, water was pumped vertically from the bottom of the column at different volumetric flow rates. At every particular flow rate, the pressure difference between the two ends of the column was measured. According to Darcy's law, volumetric flow rate is linearly dependent on pressure difference, and the plot of these

two variables should be a straight line, passing through the origin. The permeability was then obtained from the slope of the line.

The transport of NPs in the sand packed column was investigated using a 3-phase injection procedure (see Figure VII.1 for a schematic drawing of the experimental setup). At phase 1, the column was saturated by injecting 10 pore volumes (PV) of a NP-free solution to equalize ion concentration in the effluent and the injection. Phase 2 was the injection of 10PV of the solution of phase 1 containing 100ppm NP into the bottom of the column at the rate of 0.3mL/min. Finally, phase 3 consisted of a 5PV post-flush with the same solution as that of phase 1. A timed sample collector was utilized for automatic collection of effluents at every 1/3PV interval. In each interval, NP concentration was examined by a UV-vis spectrophotometer (Thermoscientific, Genesys10s) using a 3.5mL quartz cuvette. The detection limit of the method was 1ppm. Exceptionally, in the case of the 10% salt solution, two single pulse inputs of 0.067PV each were injected into the column at the end of phase 3. This additional pulse injection procedure was aimed to determine the hydraulic dispersion coefficient of the NPs from the breakthrough curve resulting from these two pulses. The delay time between the two pulses was 3PV.
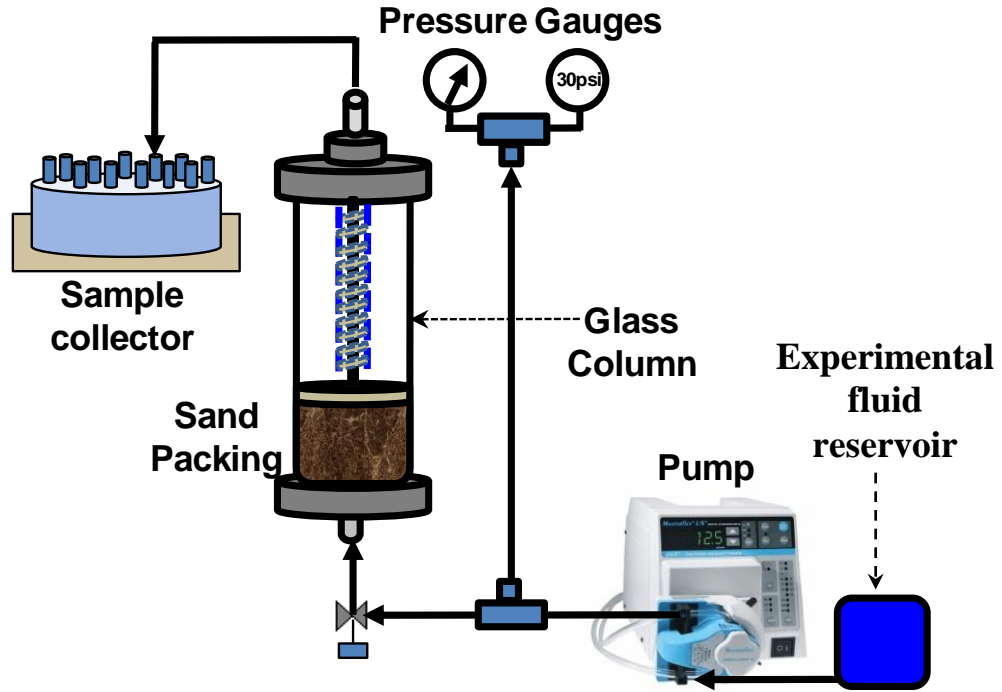
Figure VII.1. Schematic diagram of column experiments with crushed Berea sandstone packing.

VII.3 Results and discussion

VII.3.1 Effect of salt on polymer-coated NPs

The effect of salt on particle deposition of uncoated particles in packed beds has been investigated and well-documented in the literature[30, 185, 187, 210]. It is widely known that increasing salt in injected solutions provokes particle retention due to the compression of the electrical double layer, which results in a reduction of electrostatic repulsion[225]. This reduction has been evidenced by the diminishing of the energy barrier in the interaction energy profile, predicted by the theory of Derjaguin, Landau, Verwey and Overbeek (DLVO theory) when increasing salt concentration[226-228]. It is thereby expected that an increase in salt concentration would result in an increase of particle retention. In contrast to that, our experimental results

113

with different salt levels show no such behavior when the salt concentration is within

0% and 5% (see Figure VII.2).
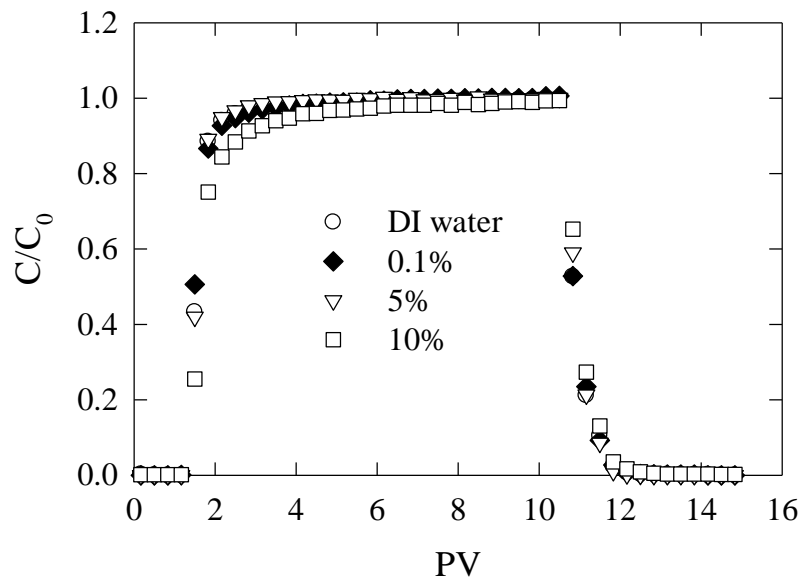
Figure VII.2. Particle breakthrough of NPs under various weight percent of salt. The particle was wrapped by PVP and HEC-10 polymer and was injected as a 10PV slug into 1in-diameter and 3in-length sand packed columns.

The NP breakthrough curves overlap with each other, indicating that there is no

significant effect of salt concentration on NP retention for up to 5% salt. When the salt

concentration is increased to 10%, however, more NPs are retained in the column. The

integrated area of the 10% salt breakthrough curve is less than that of the other three salt

concentrations. It is also seen that the portion of the 10% salt breakthrough curve

between 2PV and 6PV is clearly below the other curves. The fact that the salt

concentration for up to 5% shows no impact on NP retention does not negate the role of

ionic strength in facilitating particle retention, but instead emphasizes the steric effects

of the polymer wrapping. Because the amount and configuration of polymer coating

each NP was not controlled in the coating process, the thickness of the polymer shell

was likely non-homogeneous. Therefore, the NPs that break through the column are those with a polymer shell thick enough to keep them away from the pore surfaces, where the Van der Waals attractive force is not sufficiently strong to pull them toward the pore surface. The overlapping of the curves in Figure VII.2 reveals that there is an equal amount of NPs deposited either in the primary or the secondary minimum of the DLVO energy profile, regardless of the salt concentration up to 5%. Note that attachment in the primary minimum is not difficult at high salinity level, because of the absence of the energy barrier. At 10% salt, however, the NPs undergo a stronger attractive force at the same separation distance, since the action of electrostatic repulsion is further weakened, caused by increasing salt concentration. Calculations based on DLVO theory showed a strong compression of the electrical double layer, as its thickness is inversely proportional to the square root of solution ionic strength[229]. Therefore, it is hypothesized that the strengthening of the attractive force is sufficient in pulling more NP toward the pore surfaces and resulting in more deposition. Another plausible explanation is that higher salt concentration affects the integrity of the polymer coating around the MWCNTs.

VII.3.2 Agreement between the experimental data and commonly used filtration equations

A further consideration is whether commonly reported filtration equations can fit the experimental data presented in Figure VII.2, and yield the kinetic parameters (i.e., deposition rate constant, detachment rate constant, and maximum surface deposition) through the model fitting process. For this purpose, conventional filtration theory one-site (CFT-1S), one-site with Langmuirian blocking (L-1S), one-site with RSA blocking (RSA-1S), and two-site without (CFT-2S) and with Langmuirian

blocking (L-2S) models were employed for fitting. The general expression of these models is given as follows:

$$
\begin{cases}
\dfrac{\partial C}{\partial t} = D_h \dfrac{\partial^2 C}{\partial x^2} - u\dfrac{\partial C}{\partial x} - \dfrac{\rho_b}{\phi}\dfrac{\partial S}{\partial t} \\[2mm]
\dfrac{\partial S}{\partial t} = \dfrac{\phi}{\rho_b}\psi k_{a,1}C + \dfrac{\phi}{\rho_b}k_{a,2}C - k_d S
\end{cases}
\qquad\qquad (VII.1)
$$

in which

$\psi = 1$ and $k_{a,2} = 0$ in the CFT-1S model

$\psi = 1 - \dfrac{S}{S_{max}}$ and $k_{a,2} = 0$ in the L-1S model

$\psi = 1 - 4\lambda_\infty \dfrac{S}{S_{max}} + 3.308\left(\lambda_\infty \dfrac{S}{S_{max}}\right)^2 + 1.4069\left(\lambda_\infty \dfrac{S}{S_{max}}\right)^3$ and $k_{a,2} = 0$ in the RSA-

1S model. If $S/S_{max} > 0.8$, $\psi = \dfrac{(\lambda_\infty - \varepsilon S)^3}{2k^2}$

$\psi = 1$ and $k_{a,2} \neq 0$ in the CFT-2S model

$\psi = 1 - \dfrac{S}{S_{max}}$ and $k_{a,2} \neq 0$ in the L-2S model

where S_{max} is the maximum deposited particle concentration, $\lambda_\infty = 0.546$ is the hard sphere jamming limit, ε is the conversion factor from surface coverage (λ) to surface concentration, $k_{a,1}$ is the deposition rate constant in sites of type 1, and $k_{a,2}$ is the deposition rate constant in sites of type 2.

The hydraulic dispersion coefficient, D_h, is usually obtained by running a tracer test through the examined column. In this study, D_h was obtained from the fitting of Equation (VII.1) and the pulse responses, obtained as described in Section VII.2 for the

116

case of 10% salt concentration. In this case, the analytical solution of Equation (VII.1) for a pulse input is given as follows:[185, 196]

$$C(x,t) = n_0 \frac{x}{2\sqrt{\pi D_h t^3}} \exp(-k_{a,1}t) \exp\left[-\frac{(x-ut)^2}{4D_h t} \right] \qquad (VII.2)$$

According to the model fit seen in Figure VII.3a, D_h is found to be 0.000765 cm^2/s using the sum of least squares procedure. This value of D_h obtained in this manner was fixed and used in all models that are discussed hereafter. It was not fitted again when other parameters were obtained using models based on Equation (VII.1) and the rest of the experimental data at various salt concentrations. The model results compared to the experiments are depicted in Figure VII.3b.

(a)   (b)
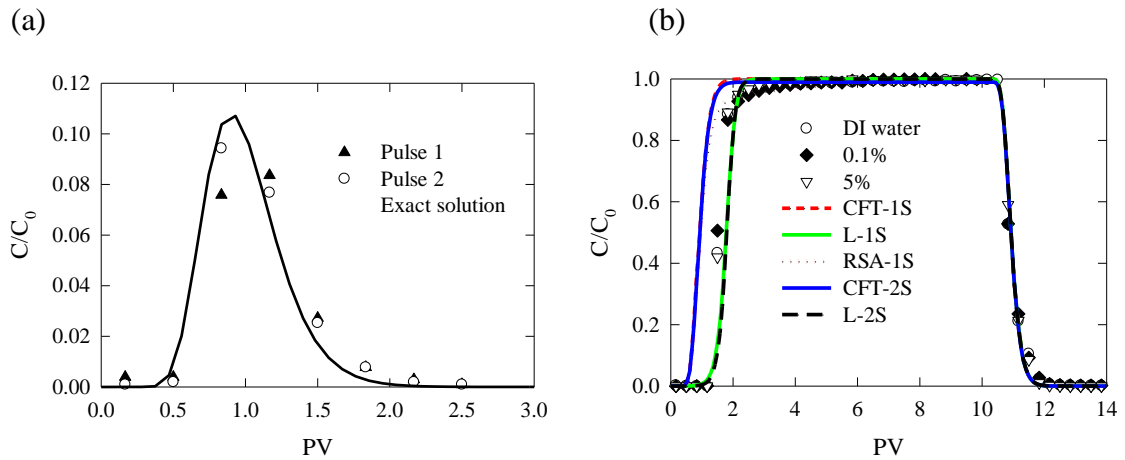
Figure VII.3. (a): Pulse responses of 0.067PV of NP injection and fitting with the exact solution [Equation (VII.2)]. The salt concentration is 10wt%; (b): Agreement between experimental results at various salt concentrations and those predicted by the most common filtration models.

It is seen that most of those models fail to match the gentle increase of C/C$_o$ observed in the experimental data. Except for the RSA-1S model, concentrations predicted by other models exhibit a steep slope prior to the transition to complete

deposition and surface saturation, noted by the plateau at $C/C_0 = 1$. As a result, the CFT-1S and CFT-2S models under-predict the cumulative retention amount of NP. Likewise, the RSA-1S model shows a significant disagreement in the amount of NP recovery, despite a good match in capturing the gentle portion of the breakthrough curves.

VII.3.3 Proposed filtration model and its agreement with the experimental data at different salinity levels and flow rates

So far, none of the above-mentioned models completely agrees with the experimental data. We present herein a new model that better predicts the transport of NP in salt in our experimental system. This new model also appears to fit results published by other groups for other salt conditions, and for other types of NPs. The new model is in fact a modification of the L-1S model with the single collector efficiency added to the blocking term, as follows:

$$\begin{cases} \dfrac{\partial C}{\partial t} = D_h \dfrac{\partial^2 C}{\partial x^2} - u\dfrac{\partial C}{\partial x} - \dfrac{\rho_b}{\phi}\dfrac{\partial S}{\partial t} \\ \dfrac{\partial S}{\partial t} = \eta\dfrac{\phi}{\rho_b}\left(1 - \dfrac{S}{S_{max}}\right)k_{a,1}C - k_d S \end{cases} \tag{VII.3}$$

The incorporated η in Equation (VII.3) is not an average value averaged across a porous medium, but it is instead a function of time and location $[\eta = \eta(x,\ t)]$. Consequently, the spatial dependence of the particle deposition rate is indirectly accounted in Equation (VII.3). It is, however, cumbersome to find the form of $\eta(x,\ t)$ in an analytical way, even though expressions of its average in the absence of an electrical double layer are available[199, 230]. To obtain a reasonable form of $\eta(x,\ t)$, we empirically correlated it to η_0 (the single collector efficiency in the absence of the repulsive

interaction[231]) and λ from the experimental data published by Ko and Elimelech[179]. In their work, they reported the nonlinear decline of η/η_0 as a function of λ at different pore velocities and particle sizes. We took their data, normalized them, and represented in Figure VII.4a, where λ was scaled by λ_{max}, defined as the maximum surface coverage.

(a)

(b)
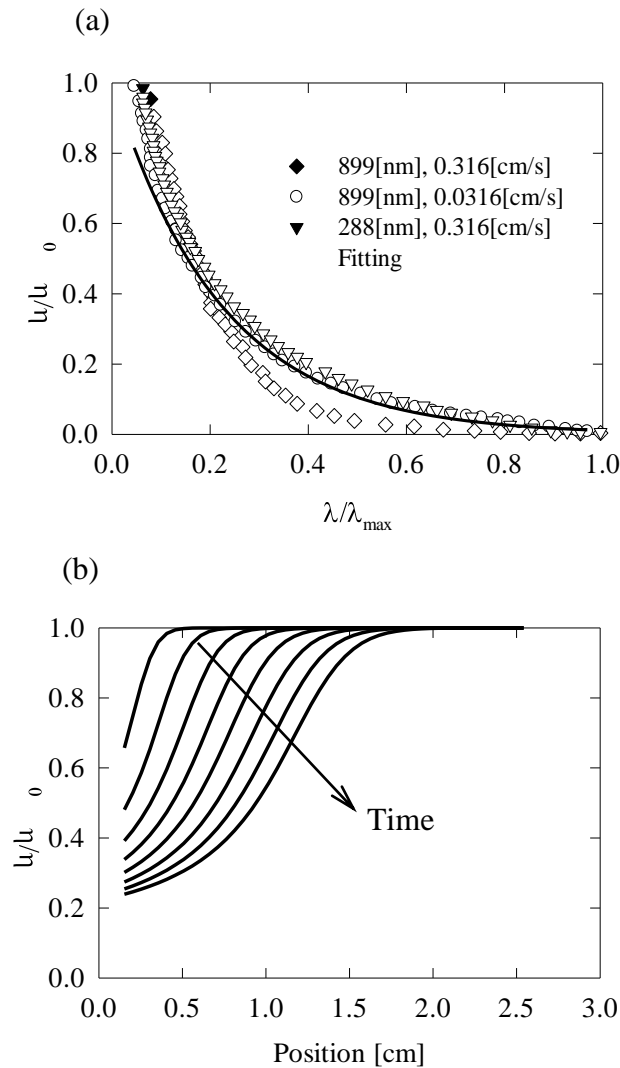
Figure VII.4. (a): Dimensionless single collector efficiency as a function of surface coverage at different particle sizes and pore velocities. Data were adopted from reference [179] and fitting equation was Equation (VII.4); (b): Dimensionless single collector efficiency along the column length at different time with D_h = 0.00009cm^2/s, u = 0.001273cm/s, ρ_b = 2.65g/cm^3, ϕ = 0.4, S_{max} = 8.3×10^{-4}mg/g, $k_{a,1}$ = 4.28×10^{-4}1/s, and ξ = 2.

119

It can be seen in Figure VII.4a that an exponential expression can describe the nonlinear decline of η/η_0 with λ/λ_{max} as follows:

$$\frac{\eta}{\eta_0} = \exp\left(-\xi \frac{\lambda}{\lambda_{max}}\right)$$

(VII.4)

where ξ is a fitting parameter, which is expected to depend on pore velocity, ionic strength of electrolyte solution, and on particle size. Since λ/λ_{max} and S/S_{max} are equivalent when the coverage is not thicker than a monolayer coverage, λ/λ_{max} can be replaced by S/S_{max} in Equation (VII.4) and substituted in Equation (VII.3) to yield

$$\begin{cases} \dfrac{\partial C}{\partial t} = D_h \dfrac{\partial^2 C}{\partial x^2} - u \dfrac{\partial C}{\partial x} - \dfrac{\rho_b}{\phi} \dfrac{\partial S}{\partial t} \\ \dfrac{\partial S}{\partial t} = \eta_0 \dfrac{\phi}{\rho_b}\left(1 - \dfrac{S}{S_{max}}\right)\exp\left(-\xi \dfrac{S}{S_{max}}\right)k_{a,1}C - k_d S \end{cases}$$

(VII.5)

To solve this system of equations, we assume a-priori that η_0 depends on neither time nor space, and can be known beforehand by theoretical calculation[199, 230]. In this work, η_0 was assumed to be 1, and S_{max} was calculated based on the amount of particle retention as obtained by the experiments. Knowing S_{max} restricts the number of fitting parameters, leaving ξ, $k_{a,1}$, and k_d undetermined. Note that $k_{a,1}$ and k_d are not interconnected, because the detachment process is intensive mainly at the "washing stage", in which the porous medium is usually flushed with a particle-free solution. This elution process washes away particles deposited in the secondary minimum in the DLVO energy profile[182, 228]. For this reason, in Equation (VII.5), the term $k_d S$ is not calculated during the particle injection stage. Instead, it is turned on at the beginning of the "washing stage". In other words, $k_{a,1}$ and k_d are obtained independently, from two

different parts of the breakthrough curve, $k_{a,1}$ from the increase of effluent concentration at the early stage of the experiment that is dominated by deposition, and k_d from the part of the curve corresponding to the washing stage that is dominated by particle detachment kinetics. To solve the system of equations in (VII.5), a method of lines[200], in which the porous medium was discretized into 50 slabs along its length was employed. The system of ordinary differential equations obtained after discretization was solved by Polymath (http://www.polymath-software.com), version 6.1. The conjunction, initial and boundary conditions are as follows:

$$C(x, t = 0) = 0$$
$$C(x = 0, 0 < t \leq T_{in}) = C_0 \qquad\qquad\qquad (VII.6)$$
$$\left.\frac{dC}{dx}\right|_{x=L,t} = 0$$

where T_{in} is the injecting time. Figure VII.4b is an illustration of the variation of η/η_0 along the medium length at different times for an extreme case of solving Equation (VII.5) with $\xi = 2$. It is apparent from the figure that η/η_0 nonlinearly increases along the flow path, and that η/η_0 at a specific medium location decreases against time. This behavior is expected, because the particles as they travel in the porous medium tend to collide with the surface and deposit first at locations closer to the medium inlet. As more and more pore surface at these locations is occupied, it leads to the reduction of η/η_0 associated with these locations, since available space for deposition becomes more limited for the following particles. This fact forces the particles that enter the porous medium later to deposit on other locations farther downstream, where η/η_0 is still large and there is available pore surface for deposition. The saturation process advances like that, until no particle is left for deposition, or $\eta/\eta_0 = 0$ at every location.

In an attempt to capture the experimental breakthrough curves that appear in Figure VII.2, Equation (VII.5) was solved and fit to the experimental data. The parameters ξ, $k_{a,1}$, and k_d were obtained from the equation fit, while D_h was assumed to be constant and was obtained independently from the tracer tests. Among four different salt concentrations, the 5% and 10% salt are chosen to be presented, as the particle breakthrough curves for 0% and 0.1% salt concentrations were identical to that of 5% salt. The result is shown in Figure VII.5, while the fitting parameters and the coefficient of determination (R^2) are reported in Table VII.1.
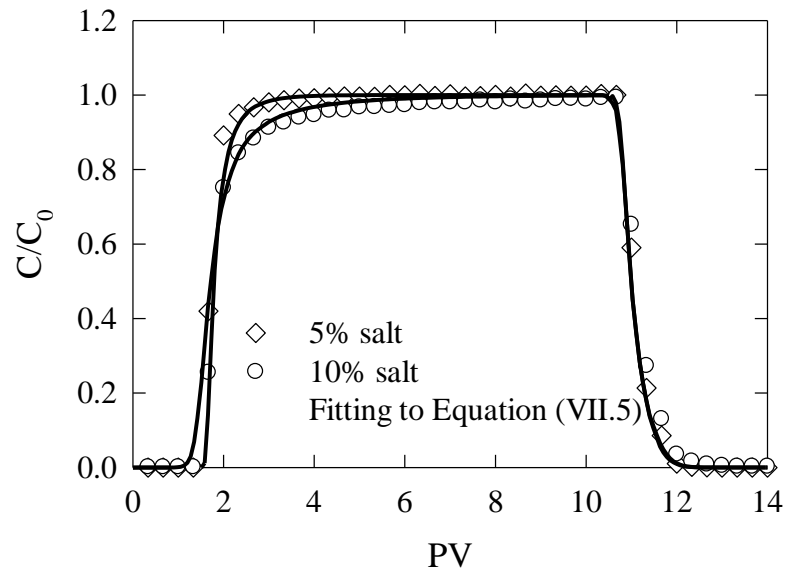
Figure VII.5. NP breakthroughs at two highest salinity levels and their agreement with the new model. The parameter ξ decreases when salt concentration increases.

Table VII.1. Fitting parameters used to solve Equation (VII.5) for two levels of salinity and two flow rates. The salt concentration in the cases of two flow rates was 10wt%. The porosity in the column was $\phi = 0.35$ in all cases.

Parameter	5% salt	10% salt	0.3 mL/min	3 mL/min
D_h [cm^2/s]	7.65×10^{-4}	7.65×10^{-4}	7.65×10^{-4}	7.65×10^{-3}
u [cm/s]	2.82×10^{-3}	2.82×10^{-3}	2.82×10^{-3}	2.82×10^{-2}
Recovered particle [%]	94	89	89	96
ρ_b [g/cm^3]	1.473	1.473	1.473	1.473
$k_{a,1}$ [1/s]	0.1	0.01	0.01	1
k_d [1/s]	2×10^{-4}	2×10^{-4}	2×10^{-4}	0.006
S_{max} [mg/g]	0.01542	0.022	0.022	0.0084
ξ [-]	13	6	6	11

In contrast to the models presented in Figure VII.3b, the gradual increase marked in the experimental breakthrough curves is well captured by Equation (VII.5) when ξ is 13 and 6 for 5% and 10% salt, respectively. The larger value of ξ corresponding to the smaller salt concentration is not by chance. Higher values of ξ mean a reduction in η and hindering of particle attachment to the pore surfaces. In terms of salinity level, decreasing salt concentration also leads to the same result, because η changes proportionally with salt concentration. One might also notice in Table VII.1 that the reported k_{a1} in the case of 10% salt is smaller than that for the case of 5% salt. The reason for this contradiction with findings in cases of small and moderate ionic strength (on the order of hundreds mM) is unclear. However, such behavior was reported in the work of Magal et al. when they investigated the transport of Fluorescent Carboxylate-Modified Latex microspheres in sand columns under salinity conditions of up to Dead Sea brine $(10^{0.9}M)$[232]. The average deposition rate increased with ionic strength of up to 250mM, approximately. Beyond this point, the deposition rate droped significantly when the ionic strength of saline solutions was on the order of 1 and 2M.

Another interesting observation is the relative importance of particle detachment versus particle deposition. It turns out that including the k_d term during the particle injection stage in the model fit is unnecessary, because the particle deposition process dominates during this stage. Particle detachment is in fact more active in the washing stage, in which the process is stimulated by either fluid shear or differences in the ionic strength of the washing solution versus the injection solution. It has been reported that washing the medium with a particle-free solution containing much lower salt concentration compared to the initial particle solution, or increasing velocity of washing solution, release attached particles from pore surfaces significantly[192, 215, 226, 233, 234]. In Equation (VII.1), one could neglect the $k_d S$ term, if the distal portion of breakthrough curves showed a sharp reduction, implying no particle detachment[186, 212]. The values of k_d reported in Table VII.1 were obtained by keeping $k_d = 0$ during the injection stage and then fitting for it between 10.6PV and 10.8PV. Following the work of Bergendahl and Grasso[234], the hydrodynamic shear due to the flow rates in our experiments is not expected to result in intensive particle detachment. The short duration of detachment (0.2PV) and the small values of k_d calculated herein have confirmed this expectation.

While ξ changes inversely with the ionic strength, its relation with the pore velocity is not yet elucidated. Increasing the pore velocity has been reported to be unfavorable for particle deposition, and thereby, particle recovery is increased[179, 186, 215, 235]. Likewise, increasing ξ potentially leads to the same consequence, since η decreases. To clarify this issue, the experiment with 10% salt was replicated with a higher flow rate of up to 3mL/min. The NP breakthrough from this replication is presented in Figure

VII.6 together with the case of the same salt concentration but with smaller pore velocity.
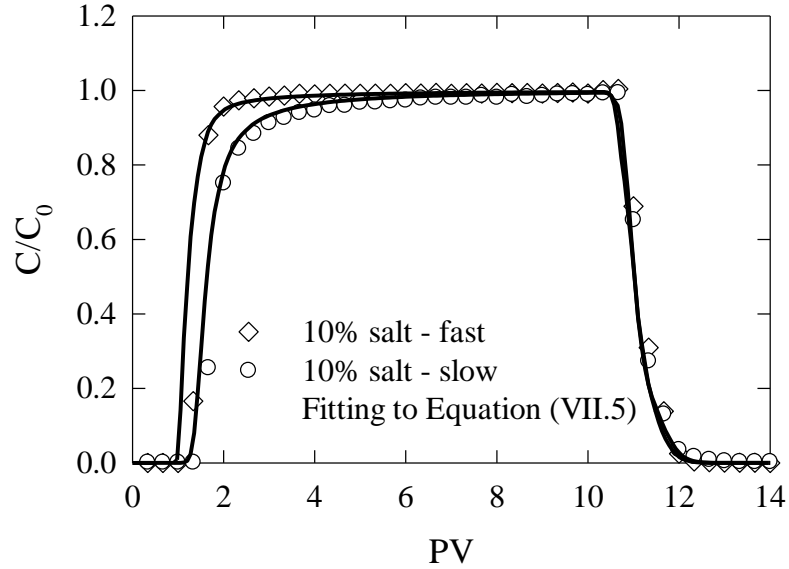
Figure VII.6. NP breakthroughs at the injection rate of 0.3mL/min (slow) and 3mL/min (fast) and their agreement with the new model. The parameter ξ increases when pore velocity increases.

In Figure VII.6, an earlier breakthrough and higher particle recovery in the case of higher pore velocity are observed. These features are all consistent with results reported in the literature[25,30,45,48]. Moreover, the relation between the pore velocity and ξ is consistent with the behavior described above (see Table VII.1).

VII.3.4 Agreement of the modified filtration model with prior data available in the literature

In Figure VII.7 we present the fitting of Equation (VII.5) with other published data and comparisons with other forms of the filtration equation used in those works. Breakthrough data of E. Coli and latex micro spheres through a silica sand packed column in Smith et al.'s work[188], fullerene (C60) through a fine Ottawa sand packed column in Li et al.'s work[186], and MWCNTs through a quartz sand packed column in

Liu et al.'s work[184] were used. Here we did not do a multi-parameter fitting. Instead, we used the parameters already calculated by the researchers in these papers. The parameters already reported by the authors were reused, such as k_a in the work of Smith et al. and k_a and S_{max} in the work of Li et al., to avoid simultaneously getting k_a, S_{max}, and ξ by fitting. In the case of Liu et al.'s work, S_{max} was calculated in advance via the amount of final retention by numerically integrating the breakthrough curve presented in the paper, since the value of this parameter was not provided in the reference.

In the above-mentioned works, although a fit between the data and the models is reported, there exist significant differences – mostly the experimental breakthrough lines are over-predicted. Specifically, those differences were due to the failure of matching the gradual augmentation in the breakthrough curves caused by competitive deposition because of surface saturation. The k_a at this stage declines against the level of surface coverage rather than remaining constant and equal to that at the clean bed stage. It is also inferred from the differences that the surface saturation rate is not as fast as that described by the L-1S model. The presence of no significant differences between the experimental data and data generated by Equation (VII.5) in Figure VII.7 affirms the efficiency of the new model compared to others.
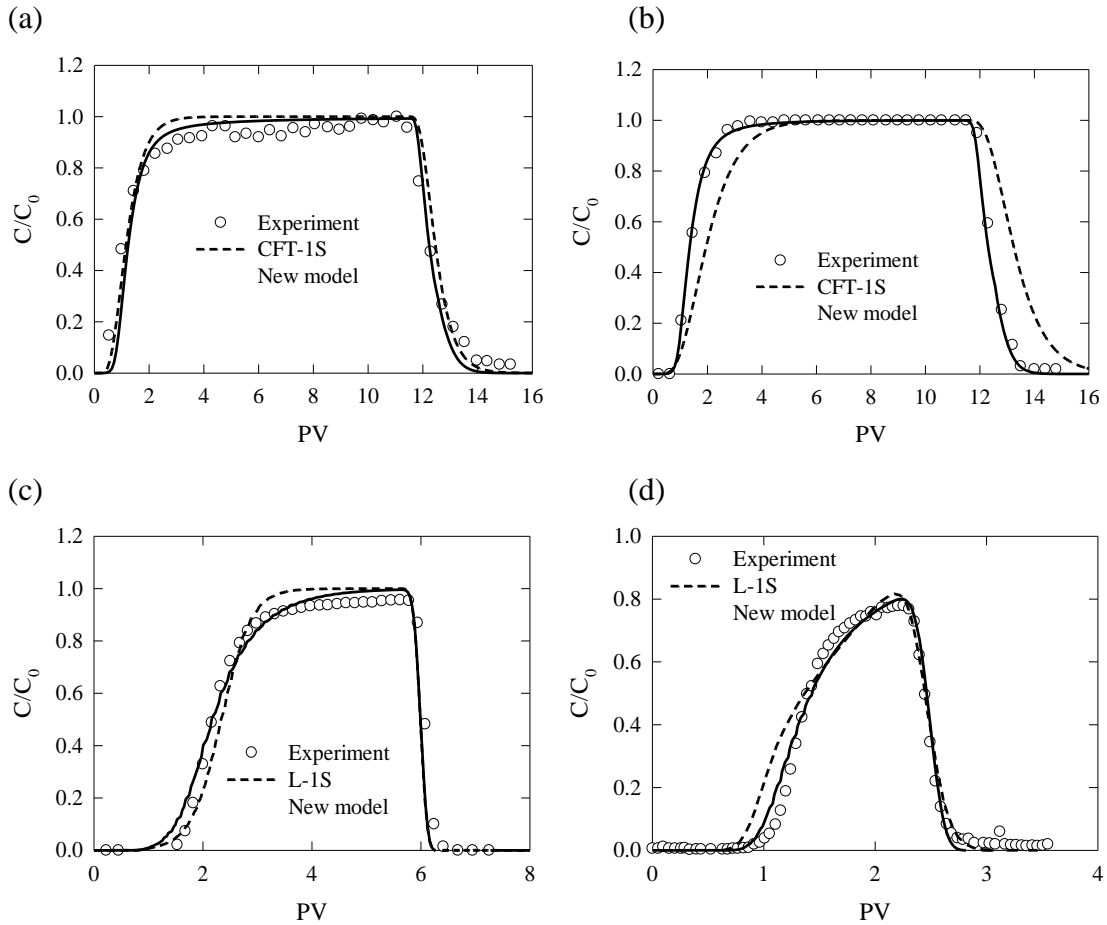
Figure VII.7. Agreement of the new model with literature data in comparison with used models in those works. (a) and (b) are the breakthrough of E. Coli and micro latex sphere adopted from reference [188], respectively. (c) is the breakthrough of fullerene (C60) adopted from reference [186], and (d) is the breakthrough of MWCNTs adopted from reference [184].

For the work of Smith et al., the proposed model successfully describes the declining rate of k_a near the surface coverage limit of the E. Coli breakthrough, and accounts for the late breakthrough of latex micro spheres although, in both cases, k_a was obtained by analyzing snapshots taken at some instants in time. For the work of Li et al., the new model predicts a slower deposition rate near the limit than that predicted by the L-1S model. While complete saturation is attained at around 3PV as interpolated from their fitting curve, complete saturation through the newly proposed model is 2PV later. The predicted slow saturation process is consistent with the experimental data,

127

which show an incomplete saturation. The normalized concentration of effluent remains less than unity during the measured time intervals. In the work of Liu et al., the improvement of the new model is noticeable at the first 1.5PV, where the L-1S model shows an earlier particle breakthrough compared to that from experimental data. The early breakthrough in this segment implies less intensive deposition in the clean bed stage than that observed in the experiment. In addition, given that the L-1S model predicts a steeper slope of the early breakthrough segment than the slope of the next segment, bounded within 1.5PV and 2.5PV, the deposition is predicted to be intensive after the clean bed stage. This intensive deposition is unlikely, since experimental evidence shows a decrease in deposition rate against time. With our proposed model, that improbable feature is not observed.

CHAPTER VIII.   CONCLUSIONS AND FUTURE PLANS

VIII.1 Conclusions

From the results of multiple topics presented herein, the following conclusions can be drawn:

For the flow over the nanopost array attached to the bottom wall of the micro square channels, it was found that the array deforms the fully developed flow field and turns it into a developing flow field. The flow tends to recover its original shape downstream from the array and the recovery length has been found to be a function of nanopost height, distance between two nanoposts in the line, and size of the microchannels. An empirical correlation for calculating this recovery length was also developed with errors bounded within 7%. This correlation was also proven to be valuable for microchannels with different sizes and different configurations of nanopost arrays. With the appropriate definition of the Reynolds number, drag coefficients of the nanopost arrays immersed into the fluid were found to be approximately in linear relation to $1/\Re e$. This finding can be useful for the design of nanopost configurations attached to microchannel walls that can be used to enhance heat transfer, when liquid coolants are utilized. It can also be useful in microfluidic applications other than heat transfer, such as bioflows where CNTs bond with DNA or CNTs are used to filter molecules or particles out of the flow.

For the prediction of stress distributions in the structured scaffolds, the fluid flow-induced stresses were calculated in different scaffold geometries consisting of regular shapes. It was found that the 3P gamma distribution reported by VVSP for

randomized, highly porous media can also describe the stress PDFs in porous media consisting of regular geometric shapes. However, the shape of the distribution changes when the angle of the flow direction relative to the internal scaffold surfaces takes only a few specific values. Therefore, a common distribution type, such as the suggested gamma-3P distribution, can be used to describe flow-induced stresses within porous media made of regular geometric shapes (beyond the already established random pore architectures), so long as there is a wide distribution of the direction of the flow relative to the internal scaffold architecture. Additionally it was found that the VVSP distribution applies for porous media that satisfy this criterion for a wider range of porosity than previously expected: agreement with the VVSP PDF was found for porosities as low as 50%.

The findings of this topic imply that it might be possible to control the stresses during the culture process by manufacturing scaffolds of specific geometry and by orienting them in the bioreactor in specific directions. If one wishes the stresses to follow a known distribution (the gamma-3P), then the internal architecture of the scaffold should be such that a uniform and continuous PDF of θ can be obtained. On the other hand, if one, for example, wishes to manufacture scaffolds that are such that most of the stresses will be on two peak values, then a scaffold like that of Case A should be manufactured (keeping in mind that when extracellular matrix is deposited the pore architecture will probably acquire a less ordered structure resulting in a transition to the gamma-3P distribution).

For the stress distributions in the open space of ideally and randomly packed beds, it was found that the distribution is unimodal when the beds were fcc and

randomly packed, whereas it is bimodal and trimodal in the case of bcc and sc spheres, respectively. For each particular sphere packing morphology, the distribution pattern remains unchanged for different pressure drops but under Darcy flow conditions. Additionally, the KS goodness of fit test results indicate that the 3P log-normal distribution can be used to describe the normalized stress distribution computed for randomly packed spheres and fcc-packed spheres. A common 3P log-normal distribution exhibits agreement with the stress data within statistical accuracy. Likewise, normalized stress distributions of other cases of highly porous structured scaffolds are also found to considerably agree with the predicted 3P log-normal distribution. In addition, a similarity between the pore size distribution and the associated normalized stress distribution is observed when simulating flow in the pore space of the Berea sandstone geometry. Therefore, one can infer that the pore size distribution of a porous medium profoundly affects the distribution of the fluid stresses in the void spaces. Such findings can be useful in predicting the PDF of stresses that nano and microparticles encounter as they travel through different types of porous media, and in predicting the stability of these particles.

For simulations of the transport and kinetics of NPs inside the pore space of packed porous media, by applying the probability of attachment and detachment concept, three different cases of particle-pore surface interaction, namely no deposition, irreversible deposition, and reversible deposition have successfully been simulated. The packing is represented by packing solid, impermeable spheres in a periodic computational box. Simulation results have been found to be in agreement with those predicted by the conventional filtration equation in all cases of the interaction. This fact

131

allows simulation results to be upscaled and to determine macroscopic parameters by fitting simulation data to equations. Additionally, particle breakthrough of PMWCNTs in inert glass bead packed column experiments agree with the breakthrough predicted by the simulation of a conservative tracer. Therefore, this approach can provide a rapid qualitative and quantitative investigation into microfluidics porous systems, and can be generalized to other more sophisticated porous media like sandstone.

For the last topic, we have presented the transport behavior of polymer-coated NPs in crushed Berea sand packed columns under high salinity levels. At or below 5wt% salt concentration, the effect of salt on NP retention is completely eliminated, and dispersion of NP remains the same as that in deionized water, because of the use of polymer coatings. At 10wt% salt, however, there is a 2.5% difference in NP recovery compared to the above mentioned cases at the same flow rate. A new filtration model, which successfully captures the effluent behavior of NP in such cases is also proposed. In the new model, a new parameter ξ is empirically determined, and is found to be proportional to the pore velocity and inversely proportional to the ionic strength.

VIII.2 Future plans
VIII.2.1 Unstructured layers of cell growth with time

To numerically investigate the effect of the dynamic change of the scaffold porosity due to cell growth during the culturing state on the stress distributions, it is ideal to assume a uniform layer of cells covering the scaffold structures, as being done herein and in the work of Lesman et al.[86]. However, experimental evidences have shown nonuniform layers of cells being formed on the surfaces of supporting scaffolds[95, 236, 237]. Raimondi et al.[95] have observed from their fibrous scaffolds that the

cells mainly attached at the intersections of the fibers with bridged and flattened morphology after two days of static culturing. With a combination of 1 week static culturing followed by 2 week dynamic culturing in bioreactor, the cells clumped on the fibrous branches. Jungreuthmayer et al.[238] have developed an algorithm to numerically and randomly seed cells on the surface of their virtually unstructured scaffolds with both flat and bridge attachment of the cells (see Figure VIII.1).

It is, thereby, important to take into account the cell growth and proliferation versus time, by which dynamically numerical creation of cell layers on the porous scaffolds should be adopted, especially at the intersections of the scaffold structures. In association with that, stress distributions over time also need to be explored. The growth of the cell layers over time is expected to reduce the pore spaces of the cell-seeded scaffolds, leading to the increase of pore velocity and the flow-induced stresses. As the velocity field should be dynamically changed, a dynamic LBM scheme might be needed.
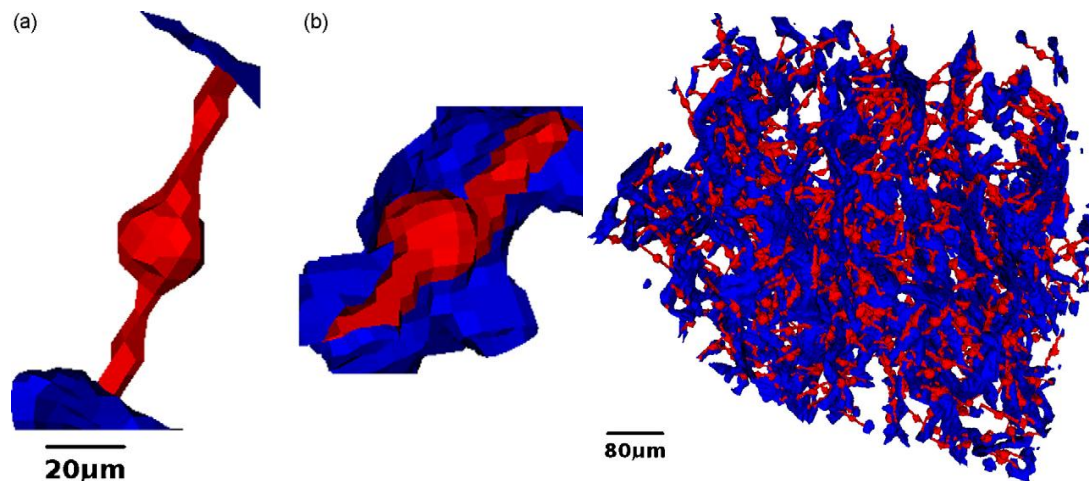
Figure VIII.1. Computationally cell seeded scaffold (right) with flat and bridge attachment of cells (left). Images taken from reference [238].

VIII.2.2 Slip boundary condition at the nanopost surfaces and heat transfer from the nanopost array to the flow

The nanopost array grown at the channel wall can be extended to the CNT arrays to take advantage of their high thermal conductivity. However, the deformation of flow as passing through a CNT array is expectedly different from what has been reported herein for any arrays with hydrophilic surfaces. CNTs, on the other hand, are highly hydrophobic, and tend to bundle up in water, because of hydrophobic interactions. With that in mind, lattice Boltzmann simulation of flow over a CNT array needs to account for the slip velocity on the CNT surfaces. The bounce back technique for no slip approximation, in which a particle will be returned to its original position at a previous time step after colliding with the channel wall, will fail to apply on the CNT surfaces, whereas a partial or full slip technique is needed for such surfaces.

For heat transfer from the CNT array to the liquid flow consideration, the LPT technique described in Section II.2 can be adopted. A number of heat markers can be released from the CNT surfaces, and advanced into the flow field by convection and diffusion. Either a uniform release or non-uniform release of heat markers over the CNT array surfaces can be employed to represent uniform or non-uniform heating from the CNT array. The temperature profile across the flow will be obtained by binning the flow and counting the number of markers in each bin.

VIII.2.3 Particle breakthrough under heterogeneous distribution of attachment probability, p_a, of the packed-sphere surfaces

The probability of attachment, p_a, associated with the sphere surfaces in Chapter VI is assumed to be uniformly distributed across the surfaces. Such assumption is reasonable in column experiments, which the packing materials undergo a severe

oxidation process with acid cleaning or combustion. After the pre-treating process, the surface charge of the packing materials is presumably uniform. A number of studies have shown that pre-cleaning collector surfaces with aggressively acidic oxidation or combustion is able to downplay effects of surface charge heterogeneity on particle attachment[239-241]. Inversely, untreated packing materials usually possess heterogeneous surface charges with which the surface charges are partially positive and negative. The presence of the positive charges among the majority of negative charges and vice versa has a pronounced effect on the particle breakthrough, which is unnoticeable by ζ potential measurement. Metallic oxides such as iron, aluminum, and manganese oxide coating on mineral surfaces are believed to be sources for the heterogeneous surface charge at macroscopic scale. Their presence, under certain conditions of the aqueous phase, results in particle attachment at favorable deposition sites regardless of the significant repulsive energy barrier revealed from DLVO theory. This source of discrepancy was early discussed by Elimelech and O'Melia more than two decades ago[242, 243]. In order to take into account the surface charge heterogeneity in the LBM/LPT simulations, the p_a can be patchily distributed over the sphere surfaces. In such cases, p_a associated with a particular patch will differ from p_a of other patches. Figure VIII.2 below illustrates possibilities of patchy distributions of p_a.
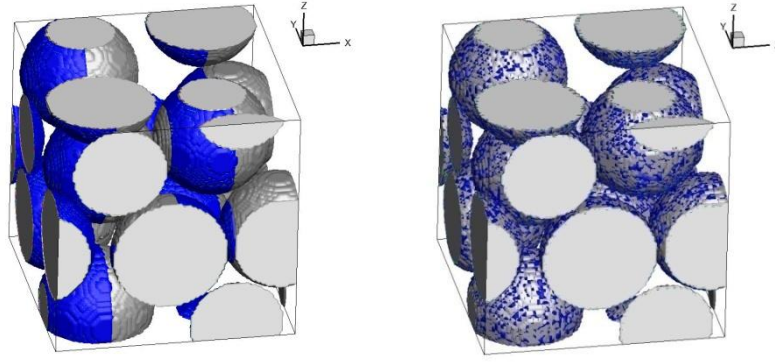
Figure VIII.2. Two possible patchy distributions of p_a: stripes (left) and random distribution (right). Blue color denotes surfaces with $p_a \neq 0$.

VIII.2.4 Saturation of packed-sphere surfaces with time by deposited particles

Together with the incorporation of surface charge heterogeneity, dynamic surface blocking can also be considered for NP transport in packed-sphere beds. It should be noticed in Chapter VI that deposited particles are considered not to hinder the attachment of following particles. In other words, the deposition of particles on the sphere surfaces, assumptively, does not change the capacity of capturing particles of the surfaces. Such consideration holds true for small pulse injection of particles or injection of dilute particle solution into the packed columns. If it is not the case, surface blocking effect of deposited particles cannot be ignored. It is admitted in the literature that a deposited particle will block a particular surface area of the collector, which is bigger than the projected area of the particle. When that area is blocked, it is unavailable to other free particles in the bulk. Excluded area, A_b, which is the ratio of the blocked area due to attachment of a particle over the projected area of that particle, is widely used to characterize the surface blocking effect in certain experimental conditions. A_b is correlated to the maximum fraction of surface coverage as follows:

136

$$A_b = \frac{1}{\lambda_{max}}$$
(VIII.1)

The pore velocity, the ionic strength of the particle solution, and the particle size has a pronounced effect on A_b. Thus, pre-estimating A_b corresponding to the designed experimental conditions is crucial for implementing the LBM/LPT simulations with surface blocking to predict the particle breakthrough.

REFERENCES

[1]   D. B. Tuckermann and R. F. Pease, 1982, Optimized convective cooling using micromachined structure, Journal of the Electrochemical Society, **129**(3), C98.

[2]   I. Mudawar and M. B. Bowers, 1999, Ultra-high critical heat flux (CHF) for subcooled water flow boiling—I: CHF data and parametric effects for small diameter tubes, International Journal of Heat and Mass Transfer, **42**(8), 1405-1428.

[3]   G. P. Celata, M. Cumo, V. Marconi, S. J. McPhail, and G. Zummo, 2006, Microtube liquid single-phase heat transfer in laminar flow, International Journal of Heat and Mass Transfer, **49**(19-20), 3538-3546.

[4]   P. S. Lee and S. V. Garimella, 2006, Thermally developing flow and heat transfer in rectangular microchannels of different aspect ratios, International Journal of Heat and Mass Transfer, **49**(17-18), 3060-3067.

[5]   L. Zhuo, T. Wen-Quan, and H. Ya-Ling, 2006, A numerical study of laminar convective heat transfer in microchannel with non-circular cross-section, International Journal of Thermal Sciences, **45**(12), 1140-1148.

[6]   J. P. McHale and S. V. Garimella, 2010, Heat transfer in trapezoidal microchannels of various aspect ratios, International Communications in Heat and Mass Transfer, **53**(1-3), 365-375.

[7]   D. Lelea, 2009, The heat transfer and fluid flow of a partially heated microchannel heat sink, International Communications in Heat and Mass Transfer, **36**(8), 794-798.

[8]   B. Badran, F. M. Gerner, P. Ramadas, T. Henderson, and K. W. Baker, 1997, Experimental results for low-temperature silicon micromachined micro heat pipe arrays using water and methanol as working fluids, Experimental Heat Transfer: A Journal of Thermal Energy Generation, Transport, Storage, and Conversion, **10**(4), 253-272.

[9]   J. Lee and I. Mudawar, 2008, Fluid flow and heat transfer characteristics of low temperature two-phase micro-channel heat sinks – Part 1: Experimental methods and flow visualization results, International Journal of Heat and Mass Transfer, **51**(17-18), 4315-4326.

[10]   A. I. Uddin and C. M. Feroz, 2009, Effect of working fluid on the performance of a miniature heat pipe system for cooling desktop processor, Heat and Mass Transfer, **46**(1), 113-118.

[11]   S. Lee, S. U.-S. Choi, S. Li, and J. A. Eastman, 1999, Measuring thermal conductivity of fluids containing oxide nanoparticles, Journal of Heat Transfer, **121**(2), 280-289.

[12]   Y. Xuan and Q. Li, 2000, Heat transfer enhancement of nanofluids, International Journal of Heat and Fluid Flow, **21**(1), 58-64.

[13] S. M. S. Murshed, K. C. Leong, and C. Yang, 2005, Enhanced thermal conductivity of TiO2—water based nanofluids, International Journal of Thermal Sciences, **44**(4), 367-373.

[14] S. M. S. Murshed, K. C. Leong, and C. Yang, 2008, Investigations of thermal conductivity and viscosity of nanofluids, International Journal of Thermal Sciences, **47**(5), 560-568.

[15] S. K. Das, S. U. S. Choi, and H. E. Patel, 2006, Heat transfer in nanofluids—A review, Heat Transfer Engineering, **27**(10), 3-19.

[16] X.-Q. Wang and A. S. Mujumdar, 2007, Heat transfer characteristics of nanofluids: a review, International Journal of Thermal Sciences, **46**(1), 1-19.

[17] W. Yu, D. M. France, J. L. Routbort, and S. U. S. Choi, 2008, Review and comparison of nanofluid thermal conductivity and heat transfer enhancements, Heat Transfer Engineering, **29**(5), 432-460.

[18] I. Papautsky, J. Brazzle, T. Ameel, and A. B. Frazier, 1999, Laminar fluid behavior in microchannels using micropolar fluid theory, Sensors and Actuators, A: Physical, **73**(1-2), 101-108.

[19] S.-S. Hsieh, C.-Y. Lin, C.-F. Huang, and H.-H. Tsai, 2004, Liquid flow in a micro-channel, Journal of Micromechanics and Microengineering, **14**(4), 436-445.

[20] S. V. Garimella and C. B. Sobhan, 2003, Transport in microchannels - a critical review, Annual Review of Heat Transfer, **13**, 1-50.

[21] S. Yang, K. Faileong, Z. Du, and C. K. Chua, 2001, The design of scaffolds for use in tissue engineering. Part I. Traditional factors, Tissue Engineering, **7**(6), 679-689.

[22] G. Chen, T. Ushida, and T. Tateishi, 2002, Scaffold design for tissue engineering, Macromolecular Bioscience, **2**(2), 67-77.

[23] S. J. Hollister, 2009, Scaffold design and manufacturing: from concept to clinic, Advanced Materials, **21**(32-33), 3330-3342.

[24] M. E. Gomes, V. I. Sikavitsas, E. Behravesh, R. L. Reis, and A. G. Mikos, 2003, Effect of flow perfusion on the osteogenic differentiation of bone marrow stromal cells cultured on starch-based three-dimensional scaffolds, Journal of Biomedical Materials Research, **67**(1), 87-95.

[25] M. E. Gomes, R. L. Reis, and A. G. Mikos, 2006, Bone tissue engineering constructs based on starch scaffolds and bone marrow cells cultured in a flow perfusion bioreactor, Materials Science Forum, **514-516**, 980-984.

[26] R. S. Voronov, 2010, Local fluid stress and nutrient transport effects via simulations of perfusion through bone tissue engineering scaffolds, PhD thesis, University of Oklahoma.

[27] C. A. Chung, C. W. Chen, C. P. Chen, and C. S. Tseng, 2007, Enhancement of cell growth in tissue-engineering constructs under direct perfusion: modeling and simulation, Biotechnology and Bioengineering, **97**(6), 1603-1616.

[28] V. L. Colvin, 2003, The potential environmental impact of engineered nanomaterials, Nature, **21**(10), 1166-1170.

[29] N. R. Panyala, E. M. Pena-Mendez, and J. Havel, 2008, Silver or silver nanoparticles: a hazardous threat to the environment and human health?, Journal of Applied Biomedicine, **6**(3), 117-129.

[30] Z. Li, E.S. Demessie, A.A. Hassan, G.A. Sorial, 2011, Transport and deposition of CeO2 nanoparticles in water-saturated porous media, Water Research, **45**(15), 4409-4418.

[31] A. M. Schrand, M. F. Rahman, S. M. Hussain, J. J. Schlager, D. A. Smith, and A. F. Syed, 2010, Metal-based nanoparticles and their toxicity assessment, WIREs Nanomedicine and Nanobiotechnology, **2**(5), 544-568.

[32] A. Magrez, S. Kasas, V. r. Salicio, N. Pasquier, J. W. Seo, M. Celio, S. Catsicas, B. Schwaller, and L. Forro, 2006, Cellular toxicity of carbon-based nanomaterials, Nano Letters, **6**(6), 1121-1125.

[33] C. J. Smith, B. J. Shaw, and R. D. Handy, 2007, Toxicity of single walled carbon nanotubes to rainbow trout, (Oncorhynchus mykiss): Respiratory toxicity, organ pathologies, and other physiological effects, Aquatic Toxicology, **82**(2), 94-109.

[34] Y. Morimoto, M. Horie, N. Kobayashi, N. Shinohara, and M. Shimada, 2013, Inhalation toxicity assessment of carbon-based nanoparticles, Accounts of Chemical Research, **46**(3), 770-781.

[35] B. A. Suleimanov, F. S. Ismailov, and E. F. Veliyev, 2011, Nanofluid for enhanced oil recovery, Journal of Petroleum Science & Engineering, **78**(2), 431-437.

[36] S. Drexler, J. Faria, M. P. Ruiz, J. H. Harwell, and D. E. Resasco, 2012, Amphiphilic nanohybrid catalysts for reactions at the water/oil interface in subsurface reservoirs, Energy & Fuels, **26**(4), 2231-2241.

[37] A. J. Worthen, S. L. Bryant, C. Huh, and K. P. Johnston, 2013, Carbon dioxide-in-water foams stabilized with nanoparticles and surfactant acting in synergy, AIChE Journal, **59**(9), 3490-3501.

[38] N. Yahya, M. Kashif, N. Nasir, M. N. Akhtar, and N. M. Yusof, 2012, Cobalt ferrite nanoparticles: an innovative approach for enhanced oil recovery application, Journal of Nano Research, **17**, 115-126.

[39] H. M. Zaid, N. R. A. Latiff, N. Yahya, H. Soleimani, and A. Shafie, 2014, Application of electromagnetic waves and dielectric nanoparticles in enhanced oil recovery, Journal of Nano Research, **26**, 135-142.

[40] H. Soleimani, N. Yahya, N. R. A. Latiff, H. M. Zaid, B. Demiral, and J. Amighian, 2014, Novel enhanced oil recovery method using Co2+xFe2+1-

xFe3+2O4 as magnetic nanoparticles activated by electromagnetic waves, Journal of Nano Research, **26**, 111-116.

[41]   C. Matteo, P. Candido, R. Vera, and V. Francesca, 2012, Current and future nanotech applications in the oil industry, American Journal of Applied Sciences, **9**(6), 784-793.

[42]   Y. Park, R. D. Whitaker, R. J. Nap, J. L. Paulsen, V. Mathiyazhagan, L. H. Doerrer, Y.-Q. Song, M. D. Hürlimann, I. Szleifer, and J. Y. Wong, 2012, Stability of superparamagnetic iron oxide nanoparticles at different pH values: experimental and theoretical analysis, Langmuir, **28**(15), 6246-6255.

[43]   R. S. Voronov, S. B. VanGordon, V. I. Sikavitsas, and D. V. Papavassiliou, 2010, Distribution of flow-induced stresses in highly porous media, Applied Physics Letters, **97**(2), 024101.

[44]   S. Chen and G. D. Doolen, 1998, Lattice Boltzmann Method for Fluid Flows, Annual Review of Fluid Mechanics, **30**, 329-364.

[45]   M. C. Sukop and D. T. Thorne, 2006, Lattice Boltzmann Modeling: An Introduction for Geoscientists and Engineers, Springer, NewYork.

[46]   C. K. Aidun and J. R. Clausen, 2010, Lattice Boltzmann Method for Complex Flows, Annual Review of Fluid Mechanics, **42**, 439-472.

[47]   R. S. Voronov, S. B. VanGordon, V. I. Sikavitsas, and D. V. Papavassiliou, 2010, Computational modeling of flow-induced shear stresses within 3D salt-leached porous scaffolds imaged via micro-CT, Journal of Biomechanics, **43**(7), 1279-1286.

[48]   R.S. Voronov, S.B. VanGordon, V.I. Sikavitsas, and D.V. Papavassiliou, 2010, Efficient Lagrangian scalar tracking method for reactive local mass transport simulation through porous media, International Journal for Numerical Methods in Fluids, **67**(4), 501-517.

[49]   S. M. Marco and L. S. Han, 1955, A note on limiting laminar Nusselt number in ducts with constant temperature gradient by analogy to thin-plate theory, Journal of Heat Transfer, **77**, 625-630.

[50]   G. V. Kolmakov, R. Revanur, R. Tangirala, T. Emrick, T. P. Russell, A. J. Crosby, and A. C. Balazs, 2010, Using nanoparticle-filled microcapsules for site-specific healing of damaged substrates: creating a "repair-and-go" system, ACS Nano, **4**(2), 1115-1123.

[51]   R. Verberg, A. Alexeev, and A. C. Balazs, 2006, Modeling the release of nanoparticles from mobile microcapsules, Journal of Chemical Physics, **125**(22), 224712.

[52]   D. V. Papavassiliou, 2002, Scalar dispersion from an instantaneous line source at the wall of a turbulent channel for medium and hight Prandtl number fluids, International Journal of Heat and Fluid Flow, **23**(2), 161-172.

[53]   R. S. Maier, D. M. Kroll, R. S. Bernard, S. E. Howington, J. F. Peters, and H. T. Davis, 2000, Pore-scale simulation of dispersion, Physics of Fluids, **12**(8), 2065-2079.

[54]   S. Iijima, 1991, Helical Microtubules of Graphitic Carbon, Nature, **354**(6438), 56-58.

[55]   M. F. Yu, O. Lourie, M. J. Dyer, K. Moloni, T. F. Kelly, and R. S. Ruoff, 2000, Strength and breaking mechanism of multiwalled carbon nanotubes under tensile load, Science, **287**(5453), 637-640.

[56]   S. Hong and S. Myung, 2007, Nanotube electronics: A flexible approach to mobility, Nature Nanotechnology, **2**(4), 207-208.

[57]   E. Pop, D. Mann, Q. Wang, K. Goodson, and H. Dai, 2006, Thermal conductance of an individual single-wall carbon nanotube above room temperature, Nano Letters, **6**(1), 96-100.

[58]   J. Xu and T. S. Fisher, 2006, Enhancement of thermal interface materials with carbon nanotube arrays, International Journal of Heat and Mass Transfer, **49**(9-10), 1658-1666.

[59]   M. A. Panzer, G. Zhang, D. Mann, X. Hu, E. Pop, H. Dai, and K. E. Goodson, 2008, Thermal properties of metal-coated vertically aligned single-wall nanotube arrays, Journal of Heat Transfer, **130**(5), 052401.

[60]   Y. Fan, X. Zhong, J. Liu, T. Wang, Y. Zhang, and Z. Cheng, 2009, Computational fluid dynamics for effects of coolants on on-chip cooling capability with carbon nanotube micro-fin architectures, Microsystem Technologies, **15**(3), 375-381.

[61]   X. Zhong, T. Wang, J. Liu, Y. Zhang, and Z. Cheng, 2006, Computational fluid dynamics simulation for on-chip cooling with carbon nanotube micro-fin architectures, Proceedings of the 8th International Conference on Electronic Materials and Packaging, Hong Kong.

[62]   X. Zhong, Y. Fan, J. Liu, Y. Zhang, T. Wang, and Z. Cheng, 2007, A study of CFD simulation for on-chip cooling with 2D CNT micro-fin array, Proceedings of the 2007 International Symposium on High Density Packaging and Microsystem Integration (HDP'07), Shanghai, China.

[63]   J. Liu, Y. Fu, and T. Wang, 2008, Recent progress of carbon nanotubes as cooling fins in electronic packaging, 2008 International Conference on Electronic Packaging Technology & High Density Packaging (ICEPT-HDP 2008), Shanghai, China.

[64]   Y. Xu, Y. Zhang, and E. Suhir, 2006, Thermal properties of carbon nanotube array used for integrated circuit cooling, Journal of Applied Physics, **100**(7), 074302.

[65]   M. O. Zhimin, J. Anderson, and J. Liu, 2004, Integrating nano carbontubes with microchannel cooler High Density Microsystem Design and Packaging and

Component Failure Analysis, 2004. HDP '04. Proceeding of the Sixth IEEE CPMT Conference on Shanghai, China.

[66]   K. Kordás, G. Tóth, P. Moilanen, M. Kumpumäki, J. Vähäkangas, and A. Uusimäki, 2007, Chip cooling with integrated carbon nanotube microfin architectures, Applied Physics Letters, **90**(12), 123105.

[67]   A. N. Ford and D. V. Papavassiliou, 2006, Flow arround surface attached carbon nanotubes, Industrial & Engineering Chemistry Research, **45**(5), 1797-1804.

[68]   I. Battiato, P. R. Bandaru, and D. M. Tartakovsky, 2010, Elastic response of carbon nanotube forests to aerodynamic stresses, Physical Review Letters, **105**(14), 144504.

[69]   K. Tamada and H. Fujikawa, 1957, The steady two-dimensional flow of viscous fluid at low Reynolds numbers passing through an Infinite row of equal parallel circular cylinders, The Quarterly Journal of Mechanics and Applied Mathematics, **10**(4), 425-432.

[70]   H. John, 1959, Viscous flow relative to arrays of cylinders, AiChE Journal, **5**(2), 174-177.

[71]   S. Kuwabara, 1959, The forces experienced by randomly distributed parallel circular cylinders or spheres in a viscous flow at small Reynolds numbers, Journal of the Physical Society of Japan, **14**(4), 527-532.

[72]   J. B. Keller, 1964, Viscous flow through a grating or lattice of cylinders, Journal of Fluid Mechanics, **18**(1), 94-96.

[73]   A. S. Sangani and A. Acrivos, 1982, Slow flow past periodic arrays of cylinders with application to heat transfer, International Journal of Multiphase Flow, **8**(3), 193-206.

[74]   J. E. Drummond and M. I. Tahir, 1984, Laminar viscous flow through regular arrays of parallel solid cylinders, International Journal of Multiphase Flow, **10**(5), 515-540.

[75]   J. H. Walther, T. Werder, R. L. Jaffe, and P. Koumoutsakos, 2004, Hydrodynamic properties of carbon nanotubes, Physical Review E, **69**(6), 062201.

[76]   W. Tang and S. G. Advani, 2006, Drag on a nanotube in uniform liquid argon flow, The Journal of Chemical Physics, **125**(17), 174706.

[77]   B. Huner and R. G. Hussey, 1977, Cylinder drag at low Reynolds number, Physics of Fluids, **20**(8), 1211-1218.

[78]   J. Yeom, D. D. Agonafer, J. H. Han, and M. A. Shannon, 2009, Low Reynolds number flow across an array of cylindrical microposts in a microchannel and figure-of-merit analysis of micropost-filled microreactors, Journal of Micromechanics and Microengineering, **19**(6), 065025.

[79]   W. S. Janna, 2009, Introduction to Fluid Mechanics, CRC Press, Boston.

[80]   B. Porter, R. Zauel, H. Stockman, R. Guldberg, and D. Fyhrie, 2005, 3-D computational modeling of media flow through scaffolds in a perfusion Bioreactor, Journal of Biomechanics, **38**(3), 543-549.

[81]   F. M. White, 1999, Fluid Mechanics, The McGraw-Hill, New York.

[82]   R. A. Gutierrez and E. T. Crumpler, 2008, Potential effect of geometry on wall shear stress distribution across scaffold surfaces, Annals of Biomedical Engineering, **36**(1), 77-85.

[83]   N. Jaiswal, S. E. Haynesworth, A. I. Caplan, and S. P. Bruder, 1997, Osteogenic differentiation of purified, culture-expanded human mesenchymal stem cells in vitro, Journal of Cellular Biochemistry, **64**(2), 295-312.

[84]   W. L. Grayson, S. Bhumiratana, C. Cannizzaro, P. H. G. Chao, D. P. Lennon, A. I. Caplan, and G. V. Novakovic, 2008, Effects of initial seeding density and fluid perfusion rate on formation of tissue-engineered bone, Tissue Engineering Part A, **14**(11), 1809-1820.

[85]   M. A. Hussein and T. Becker, 2010, Numerical modelling of shear and normal stress of micro-porous ceramics for stimulated in-vitro cultivation of bone cells, Microfluidics Nanofluidics, **8**(5), 665-675.

[86]   A. Lesman, Y. Blinder, and S. Levenberg, 2010, Modeling of flow-induced shear stress applied on 3D cellular scaffolds: implications for vascular tissue engineering, Biotechnology and Bioengineering, **105**(3), 645-654.

[87]   V. I. Sikavitsas, G. N. Bancroft, H. L. Holtorf, J. A. Jansen, and A. G. Mikos, 2003, Mineralized matrix deposition by marrow stromal osteoblasts in 3D perfusion culture increases with increasing fluid shear forces, PNAS, **100**(25), 14683-14688.

[88]   R. J. McCoy, D. Eng, and F. J. O'Brien, 2010, Influence of shear stress in perfusion bioreactor cultures for the development of three-dimensional bone tissue constructs: a review, Tissue Engineering Part B, **16**(6), 587-601.

[89]   S. H. Cartmell, B. D. Porter, A. J. Garcia, and R. E. Guldberg, 2003, Effects of medium perfusion rate on cell-seeded three-dimensional bone constructs in vitro, Tissue Engineering, **9**(6), 1197-1203.

[90]   F. Boschetti, M. T. Raimondi, F. Migliavacca, and G. Dubini, 2006, Prediction of the micro-fluid dynamic environment imposed to three-dimensional engineered cell systems in bioreactors, Journal of Biomechanics, **39**(3), 418-425.

[91]   Y. Jia, P. O. Bagnaninchi, Y. Yang, A. E. Haj, M. T. Hinds, S. J. Kirkpatric, and R. K. Wang, 2009, Doppler optical coherence tomography imaging of local fluid flow and shear stress within microporous scaffolds, Journal of Biomedical Optics, **14**(3), 034014.

[92]   C. Jungreuthmayer, S. W. Donahue, M. J. Jaasma, A. A. Al-Munajjed, J. Zanghellini, D. J. Kelly, and F. J. O'Brien, 2009, A comparative study of shear

stresses in collagen-glycosaminoglycan and calcium phosphate scaffolds in bone tissue-engineering bioreactors, Tissue Engineering Part A, **15**(5), 1141-1149.

[93]   J. L. Milan, J. A. Planell, and D. Lacroix, 2009, Computational modelling of the mechanical environment of osteogenesis within a polylactic acid–calcium phosphate glass scaffold, Biomaterials, **30**(25), 4219-4226.

[94]   J. A. Pedersen, F. Boschetti, and M. A. Swartz, 2007, Effects of extracellular fiber architecture on cell membrane shear stress in a 3D fibrous matrix, Journal of Biomechanics, **40**(7), 1484-1492.

[95]   M. T. Raimondi, F. Boschetti, L. Falcone, G. B. Fiore, A. Remuzzi, E. Marinoni, M. Marazzi, and R. Pietrabissa, 2002, Mechanobiology of engineered cartilage cultured under a quantified fluid-dynamic environment, Biomechanics and Modeling in Mechanobiology, **1**(1), 69-82.

[96]   Q. Hou, D. W. Grijpma, and J. Feijen, 2003, Porous polymeric structures for tissue engineering prepared by a coagulation, compression moulding and salt leaching technique, Biomaterials, **24**(11), 1937-1947

[97]   A. G. Mikos, A. J. Thorsen, L. A. Czerwonka, Y. Bao, and R. Langer, 1994, Preparation and characterization of poly (L-lactic acid) foams, Polymer, **35**(5), 1068-1077.

[98]   M. Cioffi, J. Ku¨ffer, S. Stro¨bel, G. Dubini, I. Martin, and D. Wendt, 2008, Computational evaluation of oxygen and shear stress distributions in 3D perfusion culture systems: macro-scale and micro-structured models, Journal of Biomechanics, **41**(14), 2918-2925.

[99]   J. W. Lee, P. X. Lan, B. Kim, G. Lim, and D. W. Cho, 2008, Fabrication and characteristic analysis of a poly (propylene fumarate) scaffold using micro-stereolithography technology, Journal of Biomedical Materials Research Part B, **87B**(1), 1-9.

[100]   I. Zein, D. W. Hutmacher, K. C. Tan, and S. H. Teoh, 2002, Fused deposition modeling of novel scaffold architectures for tissue engineering applications, Biomaterials, **23**(4), 1169-1185.

[101]   K. Youssef, J. J. Mack, M. L. Iruela-Arispe, and L.-S. Bouchard, 2012, Macro-scale topology optimization for controlling internal shear stress in a porous scaffold bioreactor, Biotechnology and Bioengineering, **109**(7), 1844-1854.

[102]   M. T. Raimondi, F. Boschetti, L. Falcone, F. Migliavacca, A. Remuzzi, and G. Dubini, 2004, The effect of media perfusion on three-dimensional cultures of human chondrocytes: Integration of experimental and computational approaches, Biorheology, **41**(3-4), 401-410.

[103]   M. Spiegel, T. Redel, Y. J. Zhang, T. Struffert, J. Hornegger, R. G. Grossman, A. Doerfler, and C. Karmonik, 2011, Tetrahedral vs. polyhedral mesh size evaluation on flow velocity and wall shear stress for cerebral hemodynamic simulation, Computer Methods in Biomechanics and Biomedical Engineering, **14**(1), 9-22.

[104] S. Yang, K. Faileong, Z. Du, and C. K. Chua, 2002, The design of scaffolds for use in tissue engineering. Part II. Rapid prototyping techniques, Tissue Engineering, **8**(1), 1-11.

[105] S. B. VanGordon, R. S. Voronov, T. B. Blue, R. L. Shambaugh, D. V. Papavassiliou, and V. I. Sikavitsas, 2011, Effects of scaffold architecture on preosteoblastic cultures under continuous fluid shear, Industrial & Engineering Chemistry Research, **50**(2), 620-629.

[106] D. M. Wang and J. M. Tarbell, 1995, Modeling interstitial flow in an artery wall allows estimation of wall shear stress on smooth muscle cells, Journal of Biomechanical Engineering **117**(3), 358-363.

[107] J. F. Alvarez-Barreto, S. M. Linehan, R. L. Shambaugh, and V. I. Sikavitsas, 2007, Flow perfusion improves seeding of tissue engineering scaffolds with different architectures, Annals of Biomedical Engineering, **35**(3), 429-442.

[108] J. F. Alvarez-Barreto and V. I. Sikavitsas, 2007, Improved mesenchymal stem cell seeding on RGD-modified poly(L-lactic acid) scaffolds using flow perfusion, Macromolecular Bioscience, **7**(5), 579-588.

[109] H. Inoguchi, T. Tanaka, Y. Maehara, and T. Matsuda, 2007, The effect of gradually graded shear stress on the morphological integrity of a huvec-seeded compliant small-diameter vascular graft, Biomaterials, **28**(3), 486-495.

[110] J. D. Fortner, D. Y. Lyon, C. M. Sayes, A. M. Boyd, J. C. Falkner, E. M. Hotze, L. B. Alemany, Y. J. Tao, W. Guo, K. D. Ausman, V. L. Colvin, and J. B. Hughes, 2005, C60 in water: nanocrystal formation and microbial response, Environmental Science & Technology, **39**(11), 4307-4316.

[111] E. Oberdörster, 2004, Manufactured nanomaterials (fullerenes, C60) induce oxidative stress in the brain of juvenile largemouth bass, Environmental Health Perspectives, **112**(10), 1058-1062.

[112] C. M. Sayes, A. M. Gobin, K. D. Ausman, J. Mendez, J. L. West, and V. L. Colvin, 2005, Nano-C60 cytotoxicity is due to lipidperoxidation, Biomaterials, **26**(36), 7587-7595.

[113] A. L. Alpatova, W. Shan, P. Babica, B. L. Upham, A. R. Rogensues, S. J. Masten, E. Drown, A. K. Mohanty, E. C. Alocilja, and V. V. Tarabara, 2010, Single-walled carbon nanotubes dispersed in aqueous media via non-covalent functionalization: Effect of dispersant on the stability, cytotoxicity, and epigenetic toxicity of nanotube suspensions, Water Research, **44**(2), 505-520.

[114] J. Gao, S. Youn, A. Hovsepyan, V. L. Llaneza, Y. Wang, G. Bitton, and J. J. Bonzongo, 2009, Dispersion and toxicity of selected manufactured nanomaterials in natural river water samples: effects of water chemical composition, Environmental Science & Technology, **43**(9), 3322-3328.

[115] M. Bottini, S. Bruckner, K. Nika, N. Bottini, S. Bellucci, A. Magrini, A. Bergamaschi, and T. Mustelin, 2006, Multi-walled carbon nanotubes induce T lymphocyte apoptosis, Toxicology Letters, **160**(2), 121-126.

[116] A. J. Kennedy, M. S. Hull, J. A. Steevens, K. M. Dontsova, M. A. Chappell, J. C. Gunter, and C. A. Weiss, 2008, Factors influencing the partitioning and toxicity of nanotubes in the aquatic environment, Environmental Toxicology and Chemistry, **27**(9), 1932-1941.

[117] M. M. Saggaf, 2008, A vision for future upstream technologies, Journal of Petroleum Technology, **60**(3), 54-55, 94-98.

[118] A. S. Stordal and D. S. Oliver, 2011, Characterization of permeability and porosity from nanosensor observations, Advances in Water Resources, **34**(8), 946-956.

[119] J. Ullo, 2008, Computational challenges in the search for and production of hydrocarbons, Scientific Modeling and Simulations, **15**(1-3), 313-337.

[120] M. S. Zaman, M. R. Islam, and S. Mokhatab, 2012, Nanotechnologoy prospects in the petroleum industry, Petroleum Science and Technology, **30**(10), 1053-1058.

[121] L. C. Villamizar, P. Lohateeraparp, J. H. Harwell, D. E. Resasco, and B. J. Shiau, 2013, Dispersion stability and transport of nanohybrids through porous media, Transport in Porous Media, **96**(1), 63-81.

[122] M. R. Rojas, A. J. Müller, and A. E. Sáezb, 2008, Shear rheology and porous media flow of wormlike micelle solutions formed by mixtures of surfactants of opposite charge, Journal of Colloid and Interface Science, **326**(1), 221-226.

[123] M. Vasudevan, E. Buse, D. Lu, H. Krishna, R. Kalyanaraman, A. Q. Shen, B. Khomami, and R. Sureshkumar, 2010, Irreversible nanogel formation in surfactant solutions by microporous flow, Nature, **9**, 436-441.

[124] W. R. Schowalter, 1982, The effect of bulk motion on coagulation rates of colloidal dispersions, Advances in Colloid and Interface Science, **17**(1), 129-147.

[125] H. S. Chung and R. Hogg, 1985, Stability criteria for fine-particle dispersions, Colloids and Surfaces, **15**, 119-135.

[126] G. R. Zeichner and W. R. Schowalter, 1979, Effects of hydrodynamic and colloidal forces on the coagulation of dispersions, Journal of Colloid and Interface Science, **71**(2), 237-253.

[127] W. R. Schowalter, 1984, Stability and coagulation of colloids in shear fields, Annual Review of Fluid Mechanics, **16**, 245-261.

[128] M. U. Bäbler, M. Morbidelli, and J. Baldyga, 2008, Modelling the breakup of solid aggregates in turbulent flows, Journal of Fluid Mechanics, **612**, 261-289.

[129] Y. Jia, L. An, and R. K. Wang, 2009, Doppler optical microangiography improves the quantification of local fluid flow and shear stress within 3-D porous constructs, Journal of Biomedical Optics, **14**(5), 1-3.

[130] G. Grossman, 1975, Stresses and friction forces in moving packed beds, AIChE Journal, **21**(4), 720-730.

[131] A. A. Zick and G. M. Homsy, 1982, Stokes flow through periodic arrays of spheres, Journal of Fluid Mechanics, **115**, 13-26.

[132] D. Mertens, C. Heinen, E. H. Hardy, and H. W. Buggisch, 2006, Newtonian and non-Newtonian low Re number flow through bead packings Chemical Engineering & Technology, **29**(7), 854-861.

[133] S. Sarkar and G. S. Gupta, 2007, Development of a two-dimensional mathematical model for stress and velocity distribution in a packed bed, Metallurgical and Materials Transactions B, **38B**(6), 965-975.

[134] A. K. Jaiswal, T. Sundararajan, and R. P. chhabra, 1991, Hydrodynamics of Newtonian fluid flow through assemblages of rigid spherical particles in intermediate Reynolds number regime, International Journal of Engineering Science, **29**(6), 693-708.

[135] M. Campolo, F. Curcio, and A. Soldati, 2013, Minimal perfusion flow for osteogenic growth of mesenchymal stem cells on lattice scaffolds, AIChE Journal, **59**(8), 3131-3144.

[136] M. Skoge, A. Donev, F. H. Stillinger, and S. Torquato, 2006, Packing hyperspheres in high-dimensional Euclidean spaces, Physical Review E, **74**(4), 041127.

[137] N. H. Pham, R. S. Voronov, S. B. VanGordon, V. I. Sikavitsas, and D. V. Papavassiliou, 2012, Predicting the stress distribution within scaffolds with ordered architecture, Biorheology, **49**(4), 235-247.

[138] S. Wang and J. M. Tarbell, 2000, Effect of fluid flow on smooth muscle cells in a 3-dimensional collagen gel model, Arteriosclerosis Thrombosis and Vascular Biology, **20**(10), 2220-2225.

[139] C. Steele, 2008, Use of the lognormal distribution for the coefficients of friction and wear, Reliability Engineering and System Safety, **93**(10), 1574-1576.

[140] Y. Yaw and R. S. Muller, 1989, A theoretical derivation of the log-normal distribution of time-dependent dielectric breakdown in thin oxides, Solid State Electronics, **32**(7), 541-546.

[141] E. Villermaux and B. Bossa, 2009, Single-drop fragmentation determines size distribution of raindrops, Nature Physics, **5**(9), 697-702.

[142] S. Harrison, D. D. Murphy, and P. R. Ehrlich, 1988, Distribution of the bay checkerspot butterfly, euphydryas editha bayensis: Evidence for a metapopulation model, The American Naturalist, **132**, 360-382.

[143] F. D. Meyer and C. Capel-Boute, 1987, Statistical analysis of Piccardi chemical tests, International Journal of Biometeorology, **31**, 301-322.

[144] H. Hasimoto, 1959, On the periodic fundamental solutions of the Stokes equations and their application to viscous flow past a cubic array of spheres, Journal of Fluid Mechanics, **5**(2), 317-328.

[145] R. M. Griffith, 1965, A technique for studying flow, fracture and structure in porous media, Chemical Engineering Science, **20**(12), 1015-1019.

[146] F. A. L. Dullien, 1992, Porous media fluid transport and pore structure, Acedemic Press, San Diego.

[147] E. F. Blick, 1966, Capillary-orifice model for high speed flow through porous media, Industrial & Engineering Chemistry Process Design and Development, **5**(1), 90-94.

[148] F. C. Blake, 1922, The resistance of packing to fluid flow, Transactions of the American Institute of Chemical Engineers, **14**, 415-421.

[149] G. M. Fair and L. P. Hatch, 1933, Fundamental factors governing the streamline flow of water through sand, Journal of the American Water Works Association, **25**(11), 1551-1565.

[150] R. B. Bird, W. E. Stewart, and E. N. Lightfoot, 2002, Transport Phenomena, John Wiley & Sons, New York.

[151] K. M. Ramachandran and C. P. Tsokos, 2009, Mathematical Statistics with Applications, Academic Press, San Diego.

[152] E. H. D'Hollander, 1979, Estimation of the pore size distribution from the moisture characteristic, Water Resources Research, **15**(1), 107-112.

[153] K. Kosugi, 1996, Lognormal distribution model for unsaturated soil hydraulic properties, Water Resources Research, **32**(9), 2697-2703.

[154] L. Zeman and G. Tkacik, in *Materials Science of Synthetic Membranes*, edited by Lloyd, D. R. (Millipore Corporation, Bedford, 1985), Vol. 269, pp. 339-350.

[155] W. R. Ott, 1995, Environmental Statistics and Data Analysis, Lewis, Florida.

[156] R. V. Hogg and E. A. Tanis, 1988, Probability and Statistical Inference, Macmillan Publishing Company, New York.

[157] R. J. Aitken, M. Q. Chaudhry, A. B. A. Boxall, and M. Hull, 2006, Manufacture and use of nanomaterials: current status in the UK and global trends, Occupational Medicine, **56**(5), 300-306.

[158] N. M. Franklin, N. J. Roqers, S. C. Apte, G. E. Batley, G. E. Gadd, and P. S. Casey, 2007, Comparative toxicity of nanoparticulate ZnO, bulk ZnO, and ZnCl2 to a freshwater microalga (Pseudokirchneriella subcapitata): the importance of particle solubility, Environmental Science & Technology, **41**(24), 8484-8490.

[159] A. Corma, P. Atienzar, H. García, and J. Y. Chane-Ching, 2004, Hierarchically mesostructured doped CeO2 with potential for solar-cell use, Nature Materials, **3**(6), 394-397.

[160] Q. Fu, A. Weber, and M. Flytzani-Stephanopoulos, 2001, Nanostructured Au–CeO2 catalysts for low-temperature water–gas shift, Catalysis Letters, **77**(1), 87-95.

[161] V. D. Kosynkin, A. A. Arzgatkina, E. N. Ivanov, M. G. Chtoutsa, A. I. Grabko, A. V. Kardapolov, and N. A. Sysina, 2000, The study of process production of polishing powder based on cerium dioxide, Journal of Alloys and Compounds, **303-304**, 421-425.

[162] F. E. Livingston and H. Helvajian, 2005, Variable UV laser exposure processing of photosensitive glass-ceramics: maskless micro- to meso-scale structure fabrication, Applied Physics A: Materials Science & Processing, **81**(8), 1569-1581.

[163] H.C. Huang, K. Rege, J.J. Heys, 2010, Spatiotemporal temperature distribution and cancer cell death in response to extracellular hyperthermia induced by gold nanorods, ACS Nano, **4**(5), 2892-2900.

[164] M. S. Mauter and M. Elimelech, 2008, Environmental applications of carbon-based nanomaterials, Environmental Science & Technology, **42**(16), 5843-5859.

[165] D. S. Sholl and J. K. Johnson, 2006, Making high-flux membranes with carbon nanotubes, Science, **312**(5576), 1003-1004.

[166] J. Theron, J. A. Walker, and T. E. Cloete, 2008, Nanotechnology and water treatment: applications and emerging opportunities, Critical Reviews in Microbiology, **34**(1), 43-69.

[167] W. M. Prickett, B. D. V. Rite, D. E. Resasco, and R. G. Harrison, 2011, Vascular targeted single-walled carbon nanotubes for near-infrared light therapy of cancer, Nanotechnology, **22**(45), 455101.

[168] N. Behabtu, C. C. Young, D. E. Tsentalovich, O. Kleinerman, X. Wang, A. W. K. Ma, E. A. Bengio, R. F. t. Waarbeek, J. J. d. Jong, R. E. Hoogerwerf, S. B. Fairchild, J. B. Ferguson, B. Maruyama, J. Kono, Y. Talmon, Y. Cohen, M. J. Otto, and M. Pasquali, 2013, Strong, light, multifunctional fibers of carbon nanotubes with ultrahigh conductivity, Science, **339**(182), 182-186.

[169] B. Nowack and T. D. Becheli, 2007, Occurrence, behavior and effects of nanoparticles in the environment, Environmental Pollution, **150**(1), 5-22.

[170] G. Bystrzejewska-Piotrowska, J. Golimowski, and P. L. Urban, 2009, Nanoparticles: Their potential toxicity, waste and environmental management, Waste Management, **29**(9), 2587-2595.

[171] R. Zhang, Y. Bai, B. Zhang, L. Chen, and B. Yan, 2012, The potential health risk of titania nanoparticles, Journal of Hazardous Materials, **211-212**, 404-413.

[172] A. Yethiraj and A. Striolo, 2013, Fracking: what can physical chemistry offer?, Journal of Physical Chemistry Letters, **4**(4), 687-690.

[173] X. Jiang, M. Tong, R. Lu, and H. Kim, 2012, Transport and deposition of ZnO nanoparticles in saturated porous media, Colloids and Surfaces A: Physicochemical and Engineering Aspects, **401**, 29-37.

[174] N. Solovitch, J. Labille, J. Rose, P. Chaurand, D. Borschneck, M. R. Wiesner, and J. Bottero, 2010, Concurrent aggregation and deposition of TiO2

nanoparticles in a sandy porous media, Environmental Science & Technology, **44**(13), 4897-4902.

[175] X. Jiang, M. Tong, and H. Kim, 2012, Influence of natural organic matter on the transport and deposition of zinc oxide nanoparticles in saturated porous media, Journal of Colloid and Interface Science, **386**(1), 34-43.

[176] S. Sirivithayapakorn and A. Keller, 2003, Transport of colloids in saturated porous media: A pore-scale observation of the size exclusion effect and colloid acceleration, Water Resources Research, **39**(4), 1109.

[177] M. Elimelech, 1994, Effect of particle size on the kinetics of particle deposition under attractive double layer interactions, Journal of Colloid and Interface Science, **164**(1), 190-199.

[178] S. R. Kanel and S. R. Al-Abed, 2011, Influence of pH on the transport of nanoscale zinc oxide in saturated porous media, Journal of Nanoparticle Research, **13**(9), 4035-4047.

[179] C. H. Ko and M. Elimelech, 2000, The "shadow effect" in colloid transport and deposition dynamics in granular porous media: measurements and mechanisms, Environmental Science & Technology, **34**(17), 3681-3689.

[180] N. Saleh, H. J. Kim, T. Phenrat, K. Matyjaszewski, R. D. Tilton, and G. V. Lowry, 2008, Ionic strength and composition affect the mobility of surface-modified Fe0 nanoparticles in water-saturated sand columns, Environmental Science & Technology, **42**(9), 3349-3355.

[181] D. Liu, P. R. Johnson, and M. Elimelech, 1995, Colloid deposition dynamics in flow through porous media: role of electrolyte concentration, Environmental Science & Technology, **29**(12), 2963-2973.

[182] C. Shen, B. Li, C. Wang, Y. Huang, and Y. Jin, 2011, Surface roughness effect on deposition of nano- and micro-sized colloids in saturated columns at different solution Ionic strengths, Vadose Zone Journal, **10**(3), 1071-1081.

[183] D. Grolimund, M. Elimelech, and M. Borkovec, 2001, Aggregation and deposition kinetics of mobile colloidal particles in natural porous media, Colloids and Surfaces, A: Physicochemical and Engineering Aspects, **191**(1-2), 179-188.

[184] X. Liu, D. M. O'Carroll, E. J. Petersen, Q. Huang, and C. L. Anderson, 2009, Mobility of multiwalled carbon nanotubes in porous media, Environmental Science & Technology, **43**(21), 8153-8158.

[185] D. P. Jaisi and M. Elimelech, 2009, Single-walled carbon nanotubes exhibit limited transport in soil columns, Environmental Science & Technology, **43**(24), 9161-9166.

[186] Y. Li, Y. Wang, K. D. Pennell, and L. M. Abriola, 2008, Investigation of the transport and deposition of fullerene (C60) nanoparticles in quartz sands under varying flow conditions, Environmental Science & Technology, **42**(19), 7174-7180.

[187] D. P. Jaisi, N. B. Saleh, R. E. Blake, and M. Elimelech, 2008, Transport of single-walled carbon nanotubes in porous media: filtration mechanisms and reversibility, Environmental Science & Technology, **42**(22), 8317-8323.

[188] J. Smith, B. Gao, H. Funabashi, T. N. Tran, D. Luo, B. A. Ahner, T. S. Steenhuis, A. G. Hay, and M. T. Walter, 2008, Pore-scale quantification of colloid transport in saturated porous media, Environmental Science & Technology, **42**(2), 517-523.

[189] Y. Tian, B. Gao, C. S. Batista, and K. J. Ziegler, 2010, Transport of engineered nanoparticles in saturated porous media, Journal of Nanoparticle Research, **12**(7), 2371-2380.

[190] P. R. Johnson and M. Elimelech, 1995, Dynamics of colloid deposition in porous media: blocking based on random sequential adsorption, Langmuir, **11**(3), 801-812.

[191] J. E. Saiers and G. M. Hornberger, 1994, First- and second-order kinetics approaches for modeling the transport of colloidal particles in porous media, Water Resources Research, **30**(9), 2499-2506.

[192] Z. Adamczyk, B. Siwek, M. Zembala, and P. Belouschek, 1994, Kinetics of localized adsorption of colloid particles, Advances in Colloid and Interface Science, **48**, 151-280.

[193] S. A. Bradford, J. Simunek, M. Bettahar, M. T. VanGenuchten, and S. R. Yates, 2003, Modeling colloid attachment, straining, and exclusion in saturated porous media, Environmental Science & Technology, **37**(10), 2242-2250.

[194] J. L. Baez, M. P. Ruiz, J. Faria, J. H. Harwell, B. Shiau, and D. E. Resasco, 2012, Stabilization of interfacially-active-nanohybrids/polymer suspensions and transport through porous media, 18th SPE Improved Oil Recovery Symposium, Tulsa, OK.

[195] M. Shapiro and H. Brenner, 1990, Dispersion/reaction model of aerosol filtration by porous filters, Journal of Aerosol Science, **21**(1), 97-125.

[196] D. Grolimund, M. Elimelech, M. Borkovec, K. Barmettler, R. Kretzschmar, and H. Sticher, 1998, Transport of in situ mobilized colloidal particles in packed soil columns, Environmental Science & Technology, **32**(22), 3562-3569.

[197] P. R. Johnson, N. Sun, and M. Elimelech, 1996, Colloid transport in geochemically heterogeneous porous media: modeling and measurements, Environmental Science & Technology, **30**(11), 3284-3293.

[198] R. Kretzschmar, M. Borkovec, D. Grolimund, and M. Elimelech, 1999, Mobile subsurface colloids and their role in contaminant transport, Advances in Agronomy, **66**, 121-193.

[199] N. Tufenkji and M. Elimelech, 2004, Correlation equation for predicting single-collector efficiency in physicochemical filtration in saturated porous media, Environmental Science & Technology, **38**(2), 529-536.

[200] M. B. Cutlip and M. Shacham, 1998, The numerical method of lines for partial differential equations, CACHE News, **47**, 18-21.

[201] D. A. Anderson, J. C. Tannehill, and R. H. Pletcher, 1984, Computational Fluid Mechanics and Heat Transfer, McGraw-Hill, New York.

[202] A. Midilli, M. Ay, I. Dincer, and M. A. Rosen, 2005, On hydrogen and hydrogen energy strategies: I: current status and needs, Renewable and Sustainable Energy Reviews, **9**(3), 255-271.

[203] S. Thomas, 2008, Enhanced oil recovery - an overview, Oil & Gas Science and Technology, **63**(1), 9-19.

[204] H. Bargozin and J. S. Moghaddas, 2013, Stability of nanoporous silica aerogel dispersion as wettability alteration agent, Journal of Dispersion Science and Technology, **34**(10), 1454-1464.

[205] H. M. Zaid, N. Yahya, and N. R. A. Latiff, 2013, The effect of nanoparticles crystallite size on the recovery efficiency in dielectric nanofluid flooding, Journal of Nano Research, **21**, 103-108.

[206] M. R. Islam, 1999, Emerging technologies in enhanced oil recovery, Energy Sources, **21**(1-2), 97-111.

[207] A. Karimi, Z. Fakhroueian, A. Bahramian, N. P. Khiabani, J. B. Darabad, R. Azin, and S. Arya, 2012, Wettability alteration in carbonates using zirconium oxide nanofluids: EOR implications, Energy & Fuels, **26**, 1028-1036.

[208] J. Y. Chen, C. H. Ko, S. Bhattacharjee, and M. Elimelech, 2001, Role of spatial distribution of porous medium surface charge heterogeneity in colloid transport, Colloids and Surfaces, A: Physicochemical and Engineering Aspects, **191**(1-2), 3-15.

[209] T. Harter, S. Wagner, and E. R. Atwill, 2000, Colloid transport and filtration of cryptosporidium parvum in sandy soils and aquifer sediments, Environmental Science & Technology, **34**(1), 62-70.

[210] Y. Tian, B. Gao, L. Wu, L. Munoz-Carpena, and Q. Huang, 2012, Effect of solution chemistry on multi-walled carbon nanotube deposition and mobilization in clean porous media, Journal of Hazardous Materials, **231-232**, 79-87.

[211] A. Cortis, T. Harter, L. Hou, E. R. Atwill, A. I. Packman, and P. G. Green, 2006, Transport of Cryptosporidium parvum in porous media: Long-term elution experiments and continuous time random walk filtration modeling, Water Resources Research, **42**(12), DOI: 10.1029/2006WR004897.

[212] J. G. Wang, Y. Li, J. D. Fortner, J. B. Hughes, L. M. Abriola, and K. D. Pennell, 2008, Transport and retention of nanoscale C60 aggregates in water-saturated porous media, Environmental Science & Technology, **42**(10), 3588-3594.

[213] P. Schaaf and J. Talbot, 1989, Surface exclusion effects in adsorption processes, Journal of Chemical Physics, **91**(7), 4401-4409.

[214] P. Schaaf and J. Talbot, 1989, Kinetics of random sequential adsorption, Physical Review Letters, **62**(2), 175-178.

[215] F. Compère, G. Porel, and F. Delay, 2001, Transport and retention of clay particles in saturated porous media: Influence of ionic strength and pore velocity, Journal of Contaminant Hydrology, **49**(1-2), 1-21.

[216] N. T. Mattison, D. M. O'Carroll, R. K. Rowe, and E. J. Petersen, 2011, Impact of porous media grain size on the transport of multi-walled carbon nanotubes, Environmental Science & Technology, **45**(22), 9765-9775.

[217] J. F. Schijven, S. M. Hassanizadeh, and R. H.A.M. de Bruin, 2002, Two-site kinetic modeling of bacteriophages transport through columns of saturated dune sand, Journal of Contaminant Hydrology, **57**(3-4), 259-279.

[218] N. Sun, M. Elimelech, N. Z. Sun, and J. N. Ryan, 2001, A novel two-dimensional model for colloid transport in physically and geochemically heterogeneous porous media, Journal of Contaminant Hydrology, **49**(3-4), 173-199.

[219] S. Bhattacharjee, J. N. Ryan, and M. Elimelech, 2002, Virus transport in physically and geochemically heterogeneous subsurface porous media, Journal of Contaminant Hydrology, **57**(3-4), 161-187.

[220] F. J. Leij and S. A. Bradford, 2009, Combined physical and chemical nonequilibrium transport model: Analytical solution, moments, and application to colloids, Journal of Contaminant Hydrology, **110**(3-4), 87-99.

[221] S. A. Bradford, S. Torkzaban, and J. Simunek, 2011, Modeling colloid transport and retention in saturated porous media under unfavorable attachment conditions, Water Resources Research, **47**(10), DOI: 10.1029/2011WR010812.

[222] H. Yuan and A. A. Shapiro, 2011, A mathematical model for non-monotonic deposition profiles in deep bed filtration systems, Chemical Engineering Journal, **166**(1), 105-115.

[223] D. G. Brown and P. R. Jaffé, 2001, Effects of nonionic surfactants on bacterial transport through porous media, Environmental Science & Technology, **35**(19), 3877-3883.

[224] M. J. Kadhum, D. P. Swatske, J. H. Harwell, B. Shiau, and D. E. Resasco, 2013, Propagation of interfacially active carbon nanohybrids in porous media, Energy & Fuels, **27**(11), 6518-6527.

[225] N. Tufenkji, G. F. Miller, J. N. Ryan, R. W. Harvey, and M. Elimelech, 2004, Transport of Cryptosporidium Oocysts in porous Media: role of straining and physicochemical filtration, Environmental Science & Technology, **38**(22), 5932-5938.

[226] J. A. Redman, S. L. Walker, and M. Elimelech, 2004, Bacterial adhesion and transport in porous media: role of the secondary energy minimum, Environmental Science & Technology, **38**(6), 1777-1785.

[227] Y. Liu, D. Janjaroen, M. S. Kuhlenschmidt, T. B. Kuhlenschmidt, and T. H. Nguyen, 2009, Deposition of Cryptosporidium parvum Oocysts on natural organic matter surfaces: Microscopic evidence for secondary minimum deposition in a radial stagnation point flow cell, Langmuir, **25**(3), 1594-1605.

[228] Z. A. Kuznar and M. Elimelech, 2007, Direct microscopic observation of particle deposition in porous media: Role of the secondary energy minimum, Colloids and Surfaces A: Physicochemical and Engineering Aspects, **294**(1-3), 156-162.

[229] K. Katari and L. Tauxe, 2000, Effects of pH and salinity on the intensity of magnetization in redeposited sediments, Earth and Planetary Science Letters, **181**, 489-496.

[230] J. Happel, 1958, Viscous flow in multiparticle systems: Slow motion of fluids relative to beds of spherical particles, AIChE Journal, **4**(2), 197-201.

[231] J. E. Song, T. Phenrat, S. Marinakos, Y. Xiao, J. Liu, M. R. Wiesner, R. D. Tilton, and G. V. Lowry, 2011, Hydrophobic interactions increase attachment of gum arabic- and PVP-coated Ag nanoparticles to hydrophobic surfaces, Environmental Science & Technology, **45**(14), 5988-5995.

[232] N. W. E. Magal, Y. Yechieli, S. L. Walker, and A. Yakirevich, 2011, Colloid transport in porous media: Impact of hyper-saline solutions, Water Research, **45**, 3521-3532.

[233] M. W. Hahn, D. Abadzic, and C. R. O'Melia, 2004, Aquasols: On the role of secondary minima, Environmental Science & Technology, **38**(22), 5915-5924.

[234] J. Bergendahl and D. Grasso, 2000, Prediction of colloid detachment in a model porous media: hydrodynamics, Chemical Engineering Science, **55**(9), 1523-1532.

[235] S. M. Hosseini and T. Tosco, 2013, Transport and retention of high concentrated nano-Fe/Cu particles through highly flow-rated packed sand column, Water Research, **47**(1), 326-338.

[236] P. Vossenberg, G. A. Higuera, G. v. Straten, C. A. v. Blitterswijk, and A. J. B. v. Boxtel, 2009, Darcian permeability constant as indicator for shear stresses in regular scaffold systems for tissue engineering, Biomechanics and Modeling in Mechanobiology, **8**(499 - 507),

[237] N. Naveena, J. Venugopal, R. Rajeswari, S. Sundarrajan, R. Sridhar, M. Shayanti, S. Narayanan, and S. Ramakrishna, 2012, Biomimetic composites and stem cells interaction for bone and cartilage tissue regeneration, Journal of Materials Chemistry, **22**(12), 5239-5253.

[238] C. Jungreuthmayer, M. J. Jaasma, A. A. Al-Munajjed, J. Zanghellini, D. J. Kelly, and F. J. O'Brien, 2009, Deformation simulation of cells seeded on a collagen-GAG scaffold in a flow perfusion bioreactor using a sequential 3D CFD-elastostatics model, Medical Engineering & Physics, **31**(4), 420-427.

[239] G. M. Litton and T. M. Olson, 1993, Colloid deposition rates on silica bed media and artifacts related to collector surface preparation methods, Environmental Science & Technology, **27**(1), 185-193.

[240] L. Song, P. R. Johnson, and M. Elimelech, 1994, Kinetics of colloid deposition onto heterogeneously charged surfaces in porous media, Environmental Science & Technology, **28**(6), 1164-1171.

[241] M. Elimelech, M. Nagai, C. H. Ko, and J. N. Ryan, 2000, Relative insignificance of mineral grain zeta potential to colloid transport in geochemically heterogeneous porous media, Environmental Science & Technology, **34**(11), 2143-2148.

[242] M. Elimelech and C. R. O'Melia, 1990, Effect of particle size on collision efficiency in the deposition of Brownian particles with electrostatic energy barriers, Langmuir, **6**(6), 1153-1163.

[243] M. Elimelech and C. R. O'Melia, 1990, Kinetics of deposition of colloidal particles in porous media, Environmental Science & Technology, **24**(10), 1528-1536.

APPENDICES

A.1. Connection between pore size and dimensional bulk stress distribution in a pore network assumed as a bundle of capillary tubes

Consider a porous medium with circular, straight tube-like pores. Let the diameter of the pores, D, take values from an arithmetic sequence between 1 and 50μm, (i.e., each diameter is larger than the one smaller than itself by $\Delta D = 1\mu m$) and let us assume that the diameters follow a log-normal distribution. Fluid is driven through these parallel tubes by a pressure difference of 1Pa/μm. Recall that the stress profile in each pore is linearly correlated to the pore diameter as described in Equation (V.3). In order to estimate the distribution of stresses in each pore, bins of stresses are created with each bin interval chosen to be 0.01Pa ($\Delta \tau = 0.01$Pa). Given the above, in each pore the number of stress bins depends on the pore diameter, so that there are 50 bins in a pore with D =1, and 100, 150…, 2500, stress bins in pores of diameter D = 2, 3…, 50μm, respectively. Because the pore diameter follows the log-normal distribution, the probability of finding a stress bin in a particular pore is proportional to the probability of finding that pore in the network. As a result, the *global* frequency of finding a stress bin in the pore network is a summation of the *local* frequency of finding a bin with similar stress values in each one of the pores that follow the log-normal distribution. This summation can be mathematically stated as

$$f(\tau) = \sum_{i=1}^{50} f_i(\tau) \times f_r(D_i) \qquad\qquad (A.1\text{-}1)$$

where $f(\tau)$ is the *global* frequency of finding a stress in the network, $f_i(\tau)$ is the *local* frequency finding a stress in a pore with diameter D_i and $f_r(D_i)$ is the frequency of finding pores in the network with diameter equal to D_i. By doing so, the PDF of the

global stress can be calculated, and the shape of the PDF curve can be seen in Figure A.1. It is evident from Figure A.1 that the PDF follows the log-normal pattern, presented by the black solid line. The fact that the null hypothesis cannot be rejected at $\alpha = 0.2$ after testing by the Kolgomorov – Smirnov test indicates that the stresses in this particular bundle of tubes follows the log-normal law.
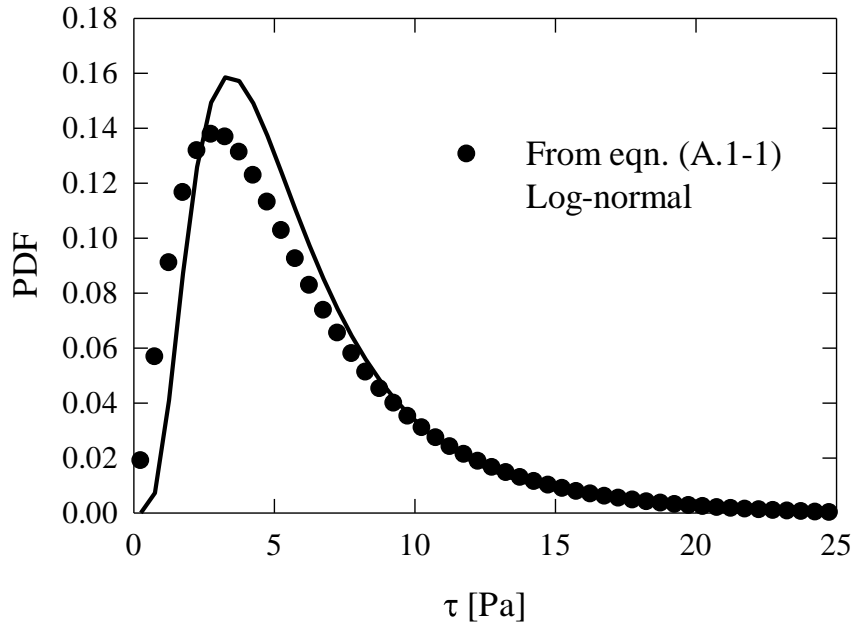
Figure A.1. Space stress distribution of a porous medium modeled by a bundle of circular capillary tubes with different diameters. The pressure different across the medium is 1Pa/μm. The log-normal(1.6, 0.61) is presented by the black solid line.

A.2. Log-normal(γ^*, ζ^*, χ) of τ^* as a consequence of log-normal(ζ, χ) of τ

If τ is lognormal(ζ, χ), what is $\tau^* = \dfrac{\tau - \bar{\tau}}{\sigma_\tau}$?

Cumulative PDF:

$$G(z) = P(\tau^* \le z) = P\left(\frac{\tau - \bar{\tau}}{\sigma_\tau} \le z \right) = P(\tau \le z\sigma_\tau + \bar{\tau})$$

158

So,

$$G(z) = \int_{0}^{z\sigma_\tau + \bar\tau} \frac{1}{\chi\tau\sqrt{2\pi}} \exp\left[-\frac{(\ln\tau - \zeta)^2}{2\chi^2} \right] d\tau \qquad (I)$$

But

$$\frac{d\tau}{d\tau *} = \sigma_\tau \quad \Rightarrow \quad d\tau = \sigma_\tau d\tau * \qquad (II)$$

We also have:

$$\ln\tau - \zeta = \ln(\tau * \sigma_\tau + \bar\tau) - \zeta = \ln\left[\sigma_\tau\left(\tau * + \frac{\bar\tau}{\sigma_\tau} \right) \right] - \zeta$$

$$= \ln\left(\tau * + \frac{\bar\tau}{\sigma_\tau} \right) - (\zeta - \ln\sigma_\tau) \qquad (III)$$

Substituting (II) and (III) into (I), we obtain

$$G(z) = \int_{0}^{z} \frac{1}{\sigma_\tau\left(\tau * + \dfrac{\bar\tau}{\sigma_\tau} \right)\chi\sqrt{2\pi}} \exp\left[-\frac{\left[\ln\left(\tau * + \dfrac{\bar\tau}{\sigma_\tau} \right) - (\zeta - \ln\sigma_\tau) \right]^2}{2\chi^2} \right] \sigma_\tau d\tau *$$

So $\tau *$ is lognormal($\gamma *$, $\zeta *$, χ), where $\gamma * = -\dfrac{\bar\tau}{\sigma_\tau}$ and $\zeta * = \zeta - \ln\sigma_\tau$.

A.3. Pore size distributions of fcc packing, bcc packing, sc packing, and random packing spheres
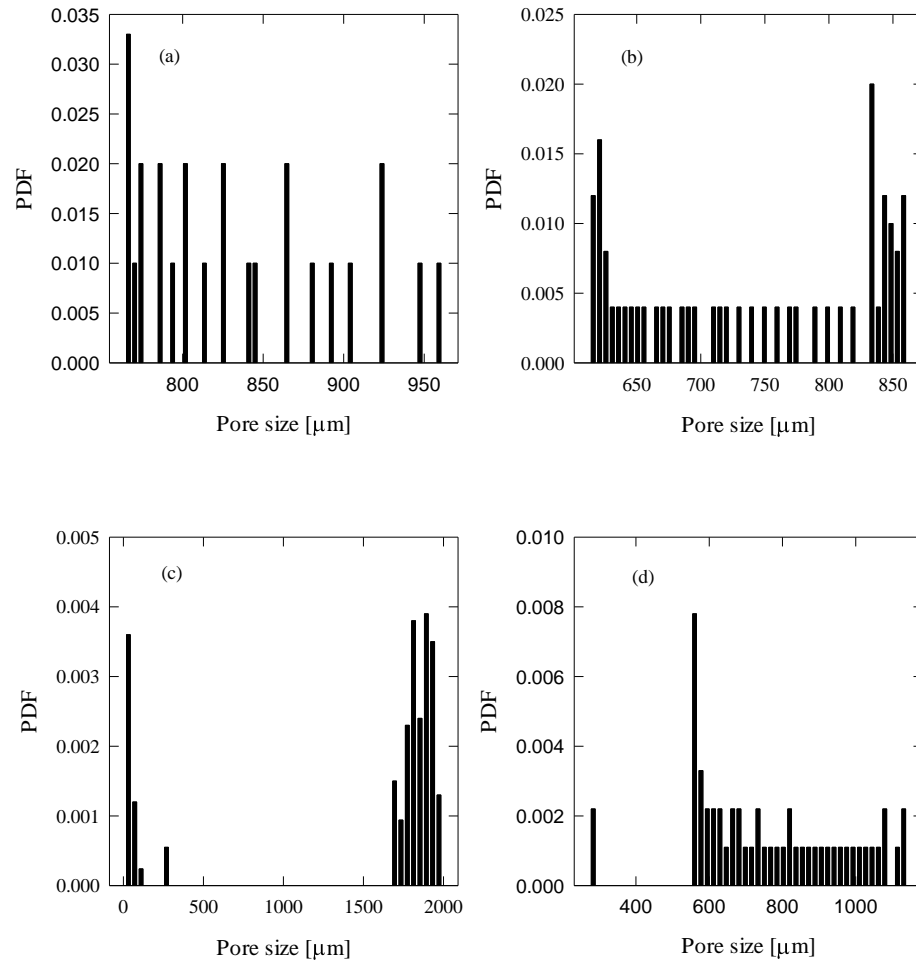
Figure A.3. Pore size distributions of the studied sphere packing patterns. (a) is fcc, (b) is bcc, (c) is random packing, and (d) is sc packing sphere.

A.4. Nomenclature

A projected area normal to flow

A_b excluded area

a size of the side of the square channels

a_e equivalent side

b center to center distance of two adjacent cylinders

B constant accounts for geometric characteristics of the medium

c lattice speed

C particle concentration in each pore volume interval

C_D drag coefficient

C_0 initial particle concentration

C_n Cunningham correction factor

d distance between each nanopost

d_c collector diameter

D nanopost diameter

D_h hydrodynamic dispersion coefficient

Da Damköhler number, defined in Equation VI.8

D_0 nominal molecular diffusivity

$D3$ number of dimensions in space

$\bar{e}$ microscopic lattice velocity

F drag force exerted on the object

f particle distribution function

f^{eq} particle equilibrium distribution function

f   probability density function

ff forcing factor

h nanopost height

k permeability of a porous medium

k_a attachment rate constant

k_B Boltzmann constant

k_d detachment rate constant

k_0 nominal attachment rate constant

K equilibrium coefficient

L   recovery length

L_{cal} recovery length calculated from Equation III.9

ℓ particle travel distance

m number of dimensions in space

n number of allowable directions

n_0 ratio of the total amount of particles injected to the volumetric flow rate

nx number of nodes in x direction

ny number of nodes in y direction

nz number of nodes in z direction

N   number of particles captured

N_0 number of particles injected

$N(0,\sigma)$ normal distribution with zero mean and standard deviation σ

p_a attachment probability

p_d	detachment probability
Q15	number of velocity lattice vector
Re	Reynolds number
$\mathfrak{Re}$	newly defined Re (Equation III.14)
R	cylinder radius
r	radial distance
r_p	particle radius
S	deposited particle concentration
S_{max}	maximum deposited particle concentration
Sc	Schmidt number
t	time
T	absolute temperature
u	pore velocity
U	macroscopic velocity in f^{eq}
$\underline{U}$	velocity vector
U_S	superficial velocity
$\vec{U}_t$	particle velocity at time t
U_{max}	maximum fluid velocity in the open space
U_∞	constant free stream velocity
V	characteristic velocity
V_r	radial velocity
V_θ	angular velocity
w	lattice specific weighing factor

$\vec{x}$ position

x   location in the flow direction

Greek symbols

α level of significance

$\bar{\alpha}$ shape parameter in gamma distribution

β scale parameter in gamma distribution

γ location parameter in gamma distribution

γ^* continuous location parameter in $f(\tau^*)$

Γ gamma distribution

δ_x unit length of microchannel simulations

Δt time interval of each time step

Δx lattice constant

$\Delta\vec{X}$ travel distance by diffusion

$\Delta P/L$ pressure drop

ε conversion factor from surface coverage to surface concentration

ζ' continuous parameter of $f(r)$

ζ continuous parameter of $f(\tau)$

ζ^* continuous location parameter of $f(\tau^*)$

η single collector efficiency

η_0 single collector efficiency in the absence of the repulsive interaction

Θ ratio of cylinder diameter to the center to center distance of two adjacent cylinders

θ azimuth

164

κ	relaxation time
λ	fractional surface coverage
λ_{max}	maximum fractional surface coverage
λ_∞	hard sphere jamming limit
μ	fluid dynamic viscosity
ν	fluid kinematic viscosity
ξ	fitting parameter in the new filtration model
Π	number of nanoposts in the line
ρ	fluid density
ρ_b	bulk density of the column
σ	standard deviation
σ_τ	standard deviation of the dimensional stress
$\underline{\underline{\tau}}$	stress tensor
τ	dimensional bulk stress
τ^*	normalized bulk stress
$\bar{\tau}$	mean bulk stress
$\bar{\tau}_w$	mean wall stress
τ_w	dimensional wall stress
τ_W^*	normalized wall stress
χ	continuous parameter of $f(\tau)$
χ'	continuous parameter of $f(r)$
ψ	surface blocking function
Φ	volume fraction occupied by nanopost

ϕ porosity

ω angle of the flow direction relative to the normal vector

Ω collision operator

Subscripts

1, 2   type of deposition sites

i lattice direction index

I   discrete node in x direction

J   discrete node in y direction

K   discrete node in z direction